

Pathlength-dependent jet quenching in the quark-gluon plasma at ALICE



Caitie Beattie

Abstract

Pathlength-dependent jet quenching in the quark–gluon plasma at ALICE

Caitie Beattie

2023

At extremely high temperatures, the quarks and gluons that compose the fundamental building blocks of our universe undergo a phase transition from stable hadronic matter to become a deconfined quark–gluon plasma (QGP). One way to study this medium is through collisions of heavy ions, where extraordinarily high energy densities produce just such a deconfined state. Of particular interest are jets, collimated showers of hadrons that originate early in the collision and undergo modification as they traverse the QGP, thus probing the medium’s properties and enabling the study of quantum chromodynamics at multiple scales. Notably, jets lose energy as they propagate through the medium, the pathlength dependence of which remains an open question. The answer is of significant interest, however, given that quantitative constraints on this dependence are closely related to the underlying mechanisms that drive jet quenching phenomena. This thesis will discuss the first measurement of jets using a technique known as event-shape engineering (ESE), a measurement made in an effort to constrain the pathlength dependence of jet energy loss.

For this thesis, charged jets were measured in Pb–Pb collisions using the ALICE detector at the CERN Large Hadron Collider. These jets were then classified according to their angle with respect to the event plane, as well as the shape of the event that they traversed. No sensitivity of the jet spectra to the event shape was observed; however, the yields were seen to be dependent on the event-plane angle. Moreover, this dependence was stronger for highly-elliptical events and weaker for highly-isotropic events. Such results are consistent with descriptions of pathlength distributions that were studied in Trajectum and the assumption that jets lose energy in a pathlength-dependent manner. Further theoretical models are required to extract quantitative constraints from this study.

Pathlength-dependent jet quenching in the quark–gluon plasma at ALICE

A Dissertation
Presented to the Faculty of the Graduate School
of
Yale University
in Candidacy for the Degree of
Doctor of Philosophy

by
Caitie Beattie

Dissertation Director: John Harris

May 2023

“We cross our bridges when we come to them and burn them behind us, with nothing to show for our progress except a memory of the smell of smoke, and a presumption that once our eyes watered.”

-Tom Stoppard

Copyright ©

Contents

1	Introduction	1
1.1	The Standard Model	2
1.2	Quantum Chromodynamics	3
1.3	Scales of QCD	6
1.4	Heavy-Ion Collisions	8
1.4.1	Stages of a Collision	8
1.4.2	Centrality	9
1.4.3	General Coordinates	10
1.4.4	Reaction Plane	11
1.5	Signatures of the QGP	12
1.5.1	Jet Quenching	12
1.5.2	Quarkonia Suppression	14
1.5.3	Strangeness Enhancement	15
1.5.4	Hydrodynamic Flow	16
1.6	QGP Properties	17
1.6.1	Temperature	19
1.6.2	Shear and Bulk Viscosity	20
1.7	Multiscale Studies	20
1.7.1	Pathlength Dependence of Jet Quenching	21
1.7.2	An Introduction to Event-Shape Engineering	22
2	The Experiment	25
2.1	The Large Hadron Collider	26

2.2	ALICE	27
2.2.1	Time Projection Chamber	28
2.2.2	Inner Tracking System	33
2.2.3	V0 Detectors	34
2.2.4	Triggering and Data Selection	34
3	Phenomenology	36
3.1	Jet Quenching	37
3.1.1	Mechanisms	37
3.1.2	Formalisms	40
3.1.3	Models	41
3.2	Modeling the Underlying Event	43
3.2.1	Initial State	44
3.2.2	Hydrodynamic Evolution	45
3.2.3	Event-Shape Engineering	46
3.3	Trajectum: A Case Study	47
4	The Measurement	56
4.1	Previous Results	57
4.1.1	Dijet Asymmetry	57
4.1.2	Azimuthal Anisotropy	58
4.1.3	Event-Shape Engineering	59
4.2	Methodology	60
4.2.1	Jets	60
4.2.2	Flow	77
4.2.3	Uncertainties	84
4.3	Results	86
4.4	Discussion	88
5	Outlook	93
5.1	Future Directions	94

5.1.1	Increased Statistics	94
5.1.2	Substructure and ESE	94
5.1.3	Dijet Asymmetry	96
5.1.4	New Experiments	98
5.2	Conclusions	99
A	Data Tables	101
B	Performance Studies	108
C	Systematic Uncertainties	128

by Caitie Beattie

All rights reserved.

“and this is the wonder that’s keeping the stars apart”

— e.e. cummings

Acknowledgments

As an undergraduate, I was told that this is the only section anyone ever reads. I hope that’s not true, as I worked pretty hard on the rest. If, however, you are unsure of whether to read on, I might like to say that the remainder of this text has many pictures and wide line-spacing - do with that information as you will. In the meantime, there are several people I’d like to thank for making this thesis a reality.

To my committee, and in particular to Helen and John. I feel so enormously privileged to have stumbled into the RHI Group, and I know this is due to the environment you have spent many years cultivating. Helen, you are one of the brightest physicists I know, and the way in which you encourage our growth as young scientists is a kindness that does not go unnoticed. I admire everything you have achieved in this field and will feel wildly successful in my life should I manage to accomplish half as much. John, thank you for taking me on as your student and having faith in me at each step of the way. I did not have the straightest path through grad school, but you have encouraged me at every point and made me feel that I belong here. I could not have asked for a better set of advisors.

To my less official advisors: Paula, Nikolai, Agnes, and Dick. Paula, I would especially like to thank you for making the logistical aspects of this job so painless. You are a force to be reckoned with, both in your prowess with administrative matters, and in how you stand up for what you believe in.

To the many post-docs who have come through RHIG: Audrey, Raghav, Mesut, Fernando, Isaac, and in particular to Laura and Mike. Laura, I owe almost everything I know about jets to you. In our many conversations ranging from physics chat to discussions of family life, you have been so generous with me in sharing the things you’ve learned. I really look up to you and know that the heavy-ion community is spectacularly lucky to be keeping you. Mike, while I didn’t like you at first, I am glad that I was not so stubborn as to maintain this opinion. Thank you for your consistent friendship and your predilection for wild road trips. Of the many reasons for which I am thankful, I am perhaps most grateful for how you believed in me when I didn’t believe in myself, and have had my back when I needed it most.

To the other RHIG students, current and former: Raymond, Dave, Michael, Dan, Tong, Youqi, Ananya, Andrew, and Sierra. Thank you for the many useful physics discussions, the even better lunch chats, and all the moral support in debugging through the years. In particular, Youqi, I will miss sharing an office with you next year. Your friendship and lively commentary brighten my afternoons.

To my collaborators on ALICE and in the heavy-ion community, and in particular to Florian, Govert, and Wilke. The work in this thesis truly would not have been possible without the effort of many hands. I have learned so much from everyone who has generously taken time to help me succeed, from analysis methodologies, to new perspectives on physics, to accelerated dish-washing techniques. Florian, thank you for sharing your office with me on my visits to CERN, and for always finding insightful topics to discuss (I am not just including you because you asked).

To my cohort, and in particular to Aniket, Giacomo, James, Nathan, Ridge, and Trevor. First year classes are notoriously unpleasant, but I think a major upside is the camaraderie that develops through shared suffering. Thank you for all the support through many difficult problem sets, and for all the fun memories we made in the first year office.

To the many other wonderful students at Yale with whom I was not sufficiently fortunate to share a cohort, and especially to Kelly and Sam. Kelly, you welcomed me to Yale and made me feel so much less alone at a time when I was vulnerable. I can't thank you enough for looking out for me the way you did. Sam, my time at Yale would have been immeasurably worse without our frequent breakfasts. I admire your kindness and your encouragement of emotional expression, be it your own or that of others. Please, never change this about yourself. The world needs more people like you.

To my friends who have been there since undergrad, and in particular to Brandon, Cassidy, Eamon, Liv, and Susanna. You all have supported me through my lowest lows, and I am eternally grateful for your presence in my life. The existence of this thesis is a credit to your friendship and the goodness you have shown me.

To my family, and in particular to Mom, Dad, Brian, Mimi (and Doritos and Augu). Thank you for always believing in me and supporting every one of my dreams. You somehow managed to raise the inquisitive little girl that I was into a semi-well-adjusted adult, and I am thankful for the curiosity you cultivated in me.

To Nick. You have never wavered in your support of my professional goals, be it through reading every abstract of mine or encouraging me when I was feeling overwhelmed. But more than this endless professional support, I have to thank you for all the ways in which you have enriched my life over the last ~ 4 (!) years. There is no one else who would have moved states with me on 3 days' notice, and no one else with whom I would have rather navigated falling ice dams, satellite internet, or the approach to 82 Crag. Thank you for all the fun, the companionship, and the million small memories I have been privileged enough to share with you.

To Hannah. Thank you for being with me every step of the way, from getting that couch into our third floor apartment on Day 1, to ridding our storage locker of mice, to giving our Quark Matter talks together in Krakow. I can't imagine having done any of this without you. Growing up, it always made me sad to not have a sister, but I couldn't have known that I would find one in adulthood. I know you are going to do amazing things in this field and that whoever gets to call you their post-doc is incredibly lucky. When you're out there changing the paradigms of jet physics, I'll be telling everyone that we were friends before you were a big deal. As evidence, I can show them this thesis, for it is as much yours as it is mine.

*“If I could remember the names of all these particles,
I’d be a botanist.”*

— Enrico Fermi

Chapter 1

Introduction

Quark-gluon plasma (QGP) is the deconfined state of quarks and gluons that exists at extremely high temperatures when hadronic matter undergoes a phase transition to become partonic matter. The QGP comprised the state of the universe in the microseconds following the Big Bang, and can be produced in the laboratory by colliding heavy ions at ultrarelativistic speeds to create “little bangs”. The partonic matter produced in these collisions possesses a host of interesting properties that span the scales of quantum chromodynamics (QCD), from asymptotically free scatterings to collective behavior and emergent phenomena. Study of these properties is proposed as a way to understand many aspects of the universe, giving us insight into questions as diverse as those regarding our origins to those concerning far-away neutron stars.

This chapter will first cover the theory of the Standard Model, with particular attention given to QCD. It will then address the physics of heavy-ion collisions and provide an overview of the fundamental experimental knowledge required to interpret studies of heavy ions. Next, this chapter will discuss the quark-gluon plasma, its properties, and the various ways we are able to study it. Finally, it will give an introduction to jet measurements using event-shape engineering, providing a brief overview of the unique contributions made in this thesis.

1.1 The Standard Model

The Standard Model of Particle Physics is an $SU(3) \times SU(2) \times U(1)$ theory characterizing the elementary particles that make up the observable universe. It includes descriptions of their interactions via the strong, weak, and electromagnetic forces. These particles can be grouped into fermions (leptons and quarks) and bosons (scalar and gauge), as depicted in Fig. 1.1, whose interactions are governed by the Lagrangian:

$$\mathcal{L}_{\text{SM}} = -\frac{1}{4}F_{\mu\nu}F^{\mu\nu} + i\bar{\psi}\not{D}\psi + \psi_i y_{ij} \psi_j \phi + h.c. + |D_\mu \phi|^2 - V(\phi) \quad (1.1)$$

where F is the field strength, ψ is the fermion multiplet, D is the covariant derivative, y is the Yukawa matrix, ϕ is the Higgs field (and h.c. here represents the hermitian conjugate of the previous term), and V is the potential of the Higgs field.¹

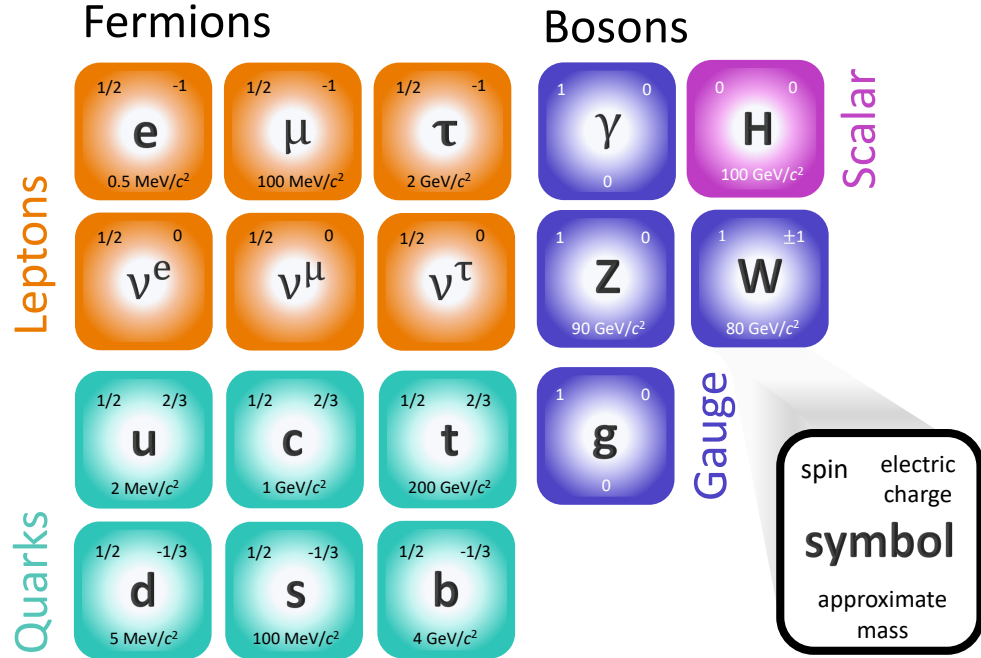


Figure 1.1: The Standard Model of Particle Physics. Note that all masses are approximate and only reported to one significant digit.

The Standard Model is one of the greatest achievements of modern physics, hav-

¹See [1] for a tidy explanation of the terms of the Standard Model Lagrangian.

ing predicted the existence and masses of several particle species before experimental evidence of their being was available, as well as accurately describing production cross-sections across 10 orders of magnitude [2]. Despite the great success of this theory, several open questions remain, such as the conspicuous absence of a description of gravity. In addition, there are aspects of the Standard Model that cannot be calculated analytically from first principles, such as the behavior of quantum chromodynamics (the theory of the strong force) in the high temperature regime. This particular deficiency has in large part motivated the development of the field of heavy-ion physics, and is responsible for the existence of this thesis.

1.2 Quantum Chromodynamics

Quantum Chromodynamics (QCD) is a Yang-Mills theory [3] symmetric under $SU(3)$ transformations.² The Yang-Mills Lagrangian, which provides a generic description for non-Abelian gauge theories belonging to $SU(N)$ groups, can be written as:

$$\mathcal{L} = -\frac{1}{4}(F_{\mu\nu}^a)^2 + \bar{\psi}(i\not{D} - m)\psi \quad (1.2)$$

where F is the field strength, D is the covariant derivative, and ψ represents the fermion multiplet in the theory. For the specific case of QCD, the Lagrangian becomes:

$$\begin{aligned} \mathcal{L}_{\text{QCD}} = & \bar{\psi}(i\not{D} - m)\psi - \frac{1}{4}(\partial_\mu A_\nu^a - \partial_\nu A_\mu^a)^2 + gA_\mu^a \bar{\psi}\gamma^\mu t^a \psi \\ & - gf^{abc}(\partial_\mu A_\nu^a)A^{\mu b}A^{\nu c} - \frac{1}{4}g^2(f^{eab}A_\mu^a A_\nu^b)(f^{ecd}A^{\mu c}A^{\nu d}) \end{aligned} \quad (1.3)$$

where the A represent the gluon fields, γ the Dirac γ -matrices, t the generator matrices of the symmetry, f^{ijk} the structure constants (derived from the commutators of the generators), and g the gauge coupling. From this Lagrangian, one can derive the interaction vertices shown in Fig. 1.2.

²A detailed derivation of the equations found in this section can be found in Peskin and Schroeder Chapters 16 and 17 [4].

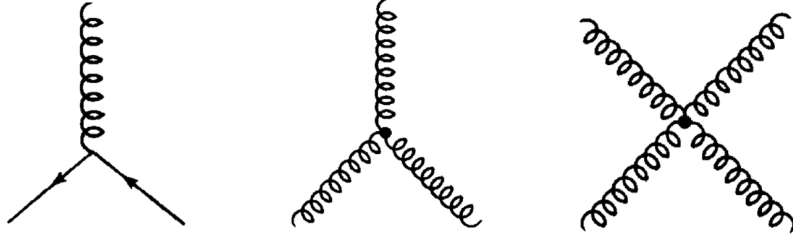


Figure 1.2: Interaction vertices arising from the QCD Lagrangian. Squiggly lines represent gluons and straight lines represent fermions.

This gauge coupling g is related to the strong coupling α_s according to the following relationship:

$$g^2 = 4\pi \cdot \alpha_s \quad (1.4)$$

It should here be noted that α_s is not a constant, but rather depends on the momentum scale of the interaction between the participating fields according to the following formula:

$$\alpha_s(Q) = \frac{2\pi}{(11 - \frac{2}{3}n_f) \log(Q/\Lambda)} \quad (1.5)$$

where n_f is the number of fermion species and $Q = \sqrt{s}$.³ Λ , an important quantity that is sometimes denoted as Λ_{QCD} , is the fundamental energy scale of QCD. It has an approximate value of 200 MeV, and marks a rough division between the perturbative and non-perturbative regimes of QCD.⁴

The inverse dependence of the strength of the coupling on the scale of the interaction Q^2 is often referred to as the “running” of the coupling constant. This dependence is shown in Fig. 1.3. Two physical consequences of the nature of the coupling are phenomena known as “confinement” and “asymptotic freedom”. Confinement describes the fact that, at normal temperatures and energy densities, partons remain bound within hadrons. This phenomenon is necessary for the stability of our universe. Conversely, asymptotic freedom refers to the effect that at very high energies and very close distance scales, partons become deconfined from these bound states and behave

³Here s is the Mandelstam variable, equal to the square of the sum of the incoming 4-momenta [5].

⁴Note that Λ_{QCD} is not a natural constant but rather takes on a value depending on the renormalization of the theory. Quotes for this value therefore often vary, see e.g. [6, 7].

independently of each other.

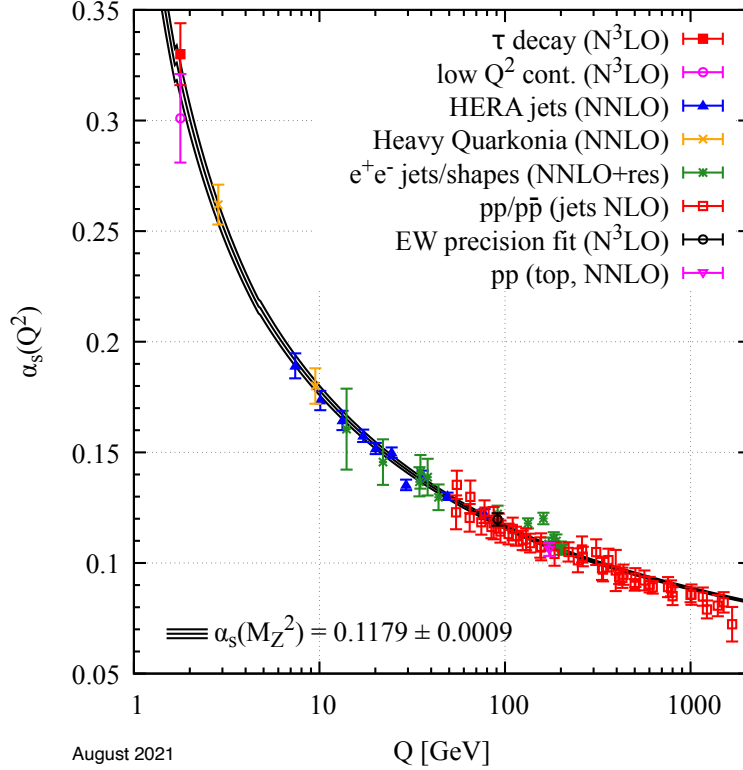


Figure 1.3: Calculations of the coupling constant α_s and its dependence on the strength of the interaction Q , along with various experimental measurements of these values. Here, M_Z refers to the mass of the Z boson [8].

The search for such a deconfined state of matter motivated early heavy-ion physicists in their quest for an asymptotically free quark-gluon plasma. It was believed that the energy densities produced in heavy-ion collisions would be sufficient to achieve such a state. Experimental studies have revealed, however, emergent properties of the QGP that are well described by hydrodynamics, indicating that the medium is in fact better understood as a strongly-coupled liquid. This observation is sometimes referred to as the “strong” coupling of the plasma (not to be confused with the strong force), and serves as the basis for a field of study that is much richer and more complicated than could have ever been predicted from knowledge of α_s alone.

1.3 Scales of QCD

In the limit of high energy interactions, α_s approaches 0. This behavior allows for the use of perturbative QCD (pQCD) to calculate a wide range of phenomena arising from large momentum transfers in a collision (sometimes termed “hard” interactions). One such phenomenon of interest is jet production.

Jets are high transverse momentum sprays of particles that originate from hard-scattered partons. When a parent parton undergoes a high- Q^2 interaction, it assumes a high virtuality.⁵ It then proceeds to radiate quarks and gluons to shed this virtuality. Eventually, as these particles return on-shell and α_s increases, the jet becomes governed by non-perturbative behavior. Its daughter partons will cluster together into bound hadrons in a process known as hadronization.⁶ The processes of jet evolution, ranging from hard scattering to hadronization, make it such that jet behavior is influenced by QCD dynamics at many scales.

Because jet production is a multi-scale process that spans the perturbative to non-perturbative regimes of QCD, it can be described using a factorization approach [9]. In this approach, the different scales are treated separately to produce the final cross-section. This is described in the following equation, which gives the cross-section for creating a high- p_T hadron, here taken as a proxy for a jet:

$$d\sigma_{AB \rightarrow h}^{\text{hard}} \approx A \cdot B \cdot f_{a/p}(x, Q^2) \otimes f_{b/p}(x, Q^2) \otimes d\sigma_{ab \rightarrow c}^{\text{hard}} \otimes \mathcal{D}_{c \rightarrow h}(z, Q^2) \quad (1.6)$$

where f are the parton distribution functions, $\sigma_{ab \rightarrow c}$ are the perturbatively calculable cross sections of the incoming partons, \mathcal{D} is the fragmentation function, and A and B are the scaling factors for the nuclear collision.

Parton distribution functions (PDFs) refer to the density of the various parton species as a function of their momentum fraction $x = p_{\text{parton}}/p_{\text{nucleon}}$. In the factorized approach, PDFs are how we quantify the pre-collision state of the incoming nuclei.

⁵Here, a virtual parton refers to one that is off-shell, such that $E^2 \neq p^2 + m^2$.

⁶While there are two main models that are often used to describe the process of hadronization in event generators (the string-breaking model and the clusterization model), in general the underlying mechanisms of hadronization are not well-understood.

Experimentally determined values of these functions can be seen in Fig. 1.4. The data used to constrain these curves historically comes from e^\pm -nucleon collisions. To this end, exploration of the low- x regime of the PDFs and the search for gluon saturation is a main motivation for the construction of the Electron Ion Collider [10].

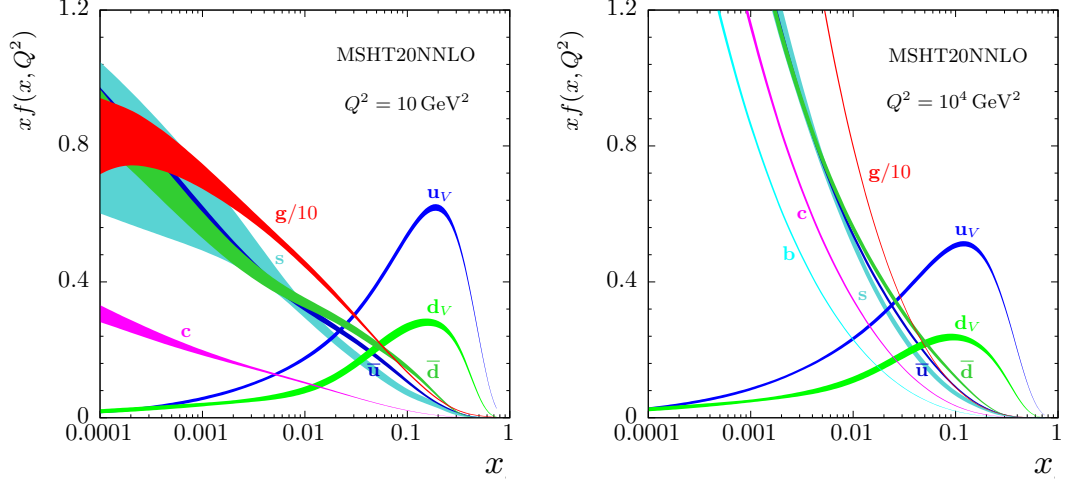


Figure 1.4: Parton distribution functions. Figure taken from [11].

Notably, when looking at the PDFs, it can be seen that they evolve with Q^2 . The necessary computational machinery to calculate this evolution can be found in the DGLAP equations [12, 13, 14], from which the parton splitting functions can be extracted. These splitting functions give the probabilities of gluon radiation from a parent parton, and are defined as:

$$P_{q \rightarrow qg}(z) = C_R \frac{1 + (1 - z)^2}{z} \quad (1.7)$$

$$P_{g \rightarrow gg}(z) = C_R \frac{1 + z^4 + (1 - z)^4}{z(1 - z)} \quad (1.8)$$

where C_R is the color factor (3 for gluons and 4/3 for quarks) and $z = \omega/E$ is the energy fraction carried by the radiated gluon.

The fragmentation functions (FFs) give the probability of a parton hadronizing in a particular way [15]. In contrast to the PDFs, which provide information about the initial state, the FFs can be used to quantify the late stage aspects of jet production.

The FFs are, however, comparable to the PDFs in that they are not perturbatively calculable. The DGLAP equations must therefore also be used to evolve them through Q .

The factorizable nature of jet production makes the study of jets an excellent test of the theory of QCD when studied in clean (i.e. e^+e^-) collision environments. Additionally, when studied in the heavy-ion environment, jets have the ability to reveal information to us about the interactions of QCD across scales in a way that is not easily calculable.

1.4 Heavy-Ion Collisions

Experimentally, we are able to study high-temperature QCD by colliding heavy-ions at ultrarelativistic energies. This is the only known way to produce the QGP phase in the laboratory. Various aspects of heavy-ion collisions will therefore be discussed here.

1.4.1 Stages of a Collision

A heavy-ion collision is a multi-stage process. First, the two incoming nuclei collide and enter a pre-equilibrium phase. This stage, referred to as the initial state, exhibits far-from-equilibrium behavior. Shortly after the initial collision the medium “hydrodynamizes”, meaning that its behavior can be described using hydrodynamics. At LHC energies, this occurs at approximately 0.2-0.6 fm/ c . After the onset of hydrodynamization, the medium expands and cools down according to the pressure gradients introduced by anisotropies in the initial state. The next stage is known as “thermalization” and is characterized by a locally isotropic medium, which occurs at about 6 fm/ c . Eventually, the medium hadronizes, achieving chemical freeze-out when the hadronic species are fixed at about 8 fm/ c . Finally, after a period of light elastic scattering, kinetic freeze-out is achieved when the particles’ kinematic properties become fixed. These particles are what are measured in our detector. These processes are summarized in Fig 1.5.

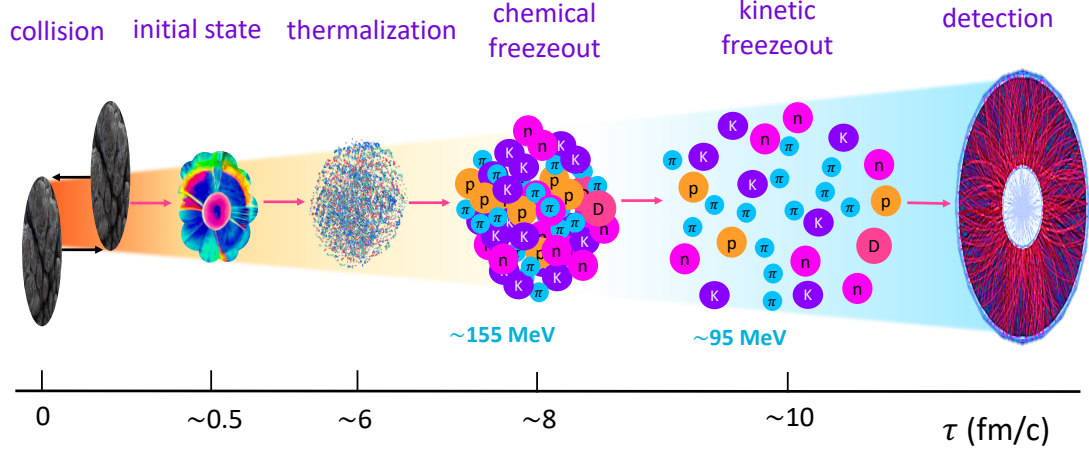


Figure 1.5: Stages of a heavy-ion collision.

1.4.2 Centrality

Centrality is a phenomenological observable that is often used as a proxy for a collision's impact parameter. Experimentally it is defined as [16]:

$$\mathcal{C} \approx \frac{1}{\sigma_{AA}} \int_{N_{ch}^{THR}}^{\infty} \frac{d\sigma}{dN_{ch}} dN_{ch} \quad (1.9)$$

where σ represents the hadronic cross-section and N_{ch} is the charged-particle multiplicity. It is typically reported as a percentile, with smaller values of centrality corresponding to smaller impact parameters. Centrality definitions make use of Glauber modeling, where events are simulated and the charged multiplicities are correlated with the average impact parameters that produce these multiplicities. In ALICE, the designation “central” corresponds to 0-10%, “semicentral” to 30-50%, and “peripheral” to 60-80%. A plot of the multiplicities measured in ALICE and their corresponding centralities is shown in Fig. 1.6.

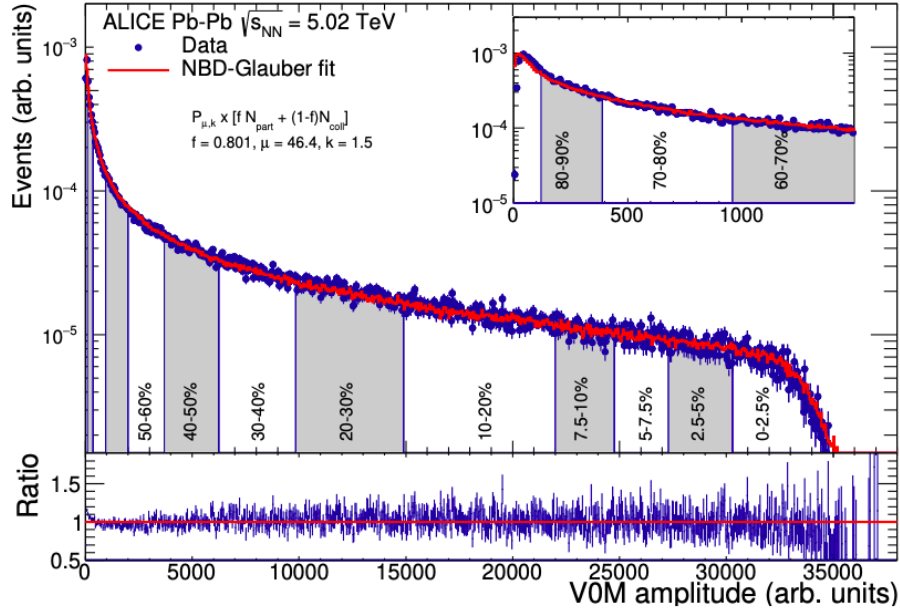


Figure 1.6: Centrality determination using the V0M summed amplitude. See Section 2.2.4 for more details on the V0 Detectors. Figure taken from [16].

1.4.3 General Coordinates

The set of coordinates frequently used when describing a particle's location in the lab-frame of a detector are the azimuthal angle φ and the rapidity y . Rapidity is a Lorentz-invariant quantity that can be defined as:

$$y = \frac{1}{2} \ln \left(\frac{E + cp_L}{E - cp_L} \right) \quad (1.10)$$

where E is a particle's energy, p_L is its longitudinal momentum, and c is the speed of light. Alternatively, one can consider a particle's pseudorapidity η . The pseudorapidity provides a convenient proxy for the rapidity, and is defined as:

$$\eta = -\ln \left[\tan \left(\frac{\theta}{2} \right) \right] \quad (1.11)$$

where θ is the polar angle from the beamline. While pseudorapidity is not a Lorentz-invariant quantity, it is often used due to the fact that one need not know (or make assumptions about) a particle's mass to calculate this variable, as compared to the

rapidity y . Pseudorapidities close to zero are described as “mid-rapidity”, while large pseudorapidity values are referred to as “forward”. Additional detector coordinates include the radius r from the beamline and the distance z along the beam axis. A schematic of these coordinates can be seen in Fig. 1.7.

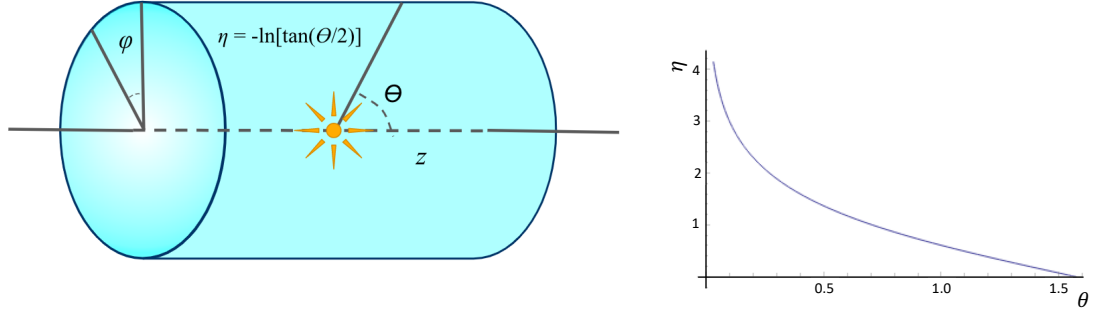


Figure 1.7: Left: A schematic of detector coordinates φ , θ , η , and z . Right: the relationship between η and θ .

1.4.4 Reaction Plane

The reaction plane is defined as the plane that contains the vector of a collision’s impact parameter and the z (beamline) vector, as seen in Fig. 1.8 (left). This is distinct from the participant plane, which arises from fluctuations in the positions of the participant nuclei and is shown in Fig. 1.8 (right). These are also both distinct from the event plane ψ_2 , which is the experimental approximation of the reaction plane. Differences between the reaction plane and the event plane arise due to fluctuations in the medium’s hydrodynamic expansion, and imprecisions in the detectors used to measure this quantity. These terms are sometimes used interchangeably, as experimentalists only have access to the event plane and, as such, there is generally no ambiguity in the concept to which one is referring. It is important, however, to keep these distinctions in mind so as to avoid making undue generalizations about the initial state from experimental data.

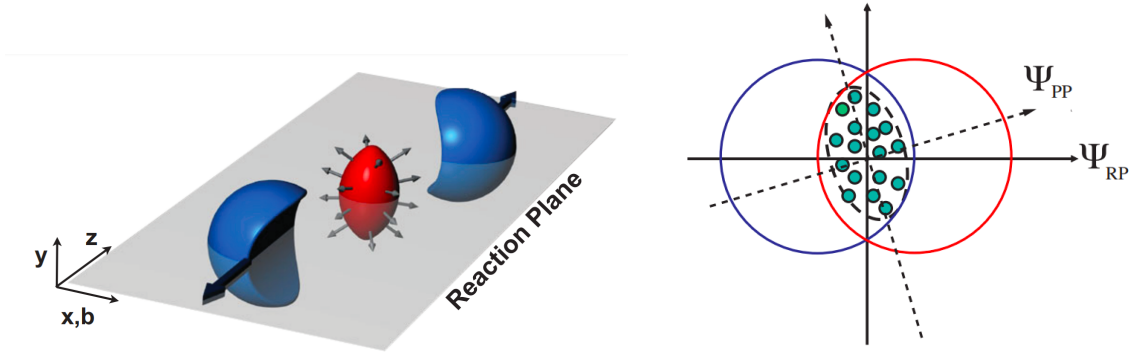


Figure 1.8: Left: Schematic of a heavy-ion collision's reaction plane. Right: Diagram showing the difference between the participant plane Ψ_{PP} and reaction plane Ψ_{RP} . Image taken from [17].

1.5 Signatures of the QGP

While the asymptotically free QGP imagined by early heavy-ion physicists does not describe our experimental measurements, there is ample evidence that the medium produced in heavy-ion collisions consists of deconfined quarks and gluons. This section will discuss some of the experimental signatures of deconfinement.

1.5.1 Jet Quenching

Jets in vacuum, as described above, provide excellent precision tests of QCD. When studied in heavy-ion collisions, however, the picture becomes more complicated. It is expected that jets will interact with the medium produced in such collisions as they traverse it, although the precise nature of these interactions is difficult to establish from first principles. The observation of jet quenching, a general term used to describe any modification that occurs to a jet due to its interactions with the medium, is thus considered a signature of QGP formation [18]. Jet quenching effects can be broadly grouped into the categories of (1) energy loss, (2) substructure modification, and (3) jet deflection. There are many observables that can probe these effects, but the first observation of quenching was made by STAR in 2003 when they studied the azimuthal production of high transverse-momentum hadrons. In this study, high p_T

triggers were used as proxies for jets. STAR observed a disappearing peak of said hadrons recoiling from a trigger, indicating suppression by the plasma [19].

Today, techniques for measuring jets have evolved significantly. Typically, such measurements involve using infrared and collinear (IRC) safe reclustering algorithms to capture the full radiation of the jet, in addition to a background subtraction procedure to ensure the signal is appropriately distinguished from the medium.⁷ Using such procedures, a host of observables can be measured, the most standard of which is the nuclear modification factor:

$$R_{AA} = \frac{1}{\langle T_{AA} \rangle} \frac{1}{N_{\text{event}}} \frac{\frac{d^2 N}{d\eta dp_T}|_{AA}}{\frac{d^2 \sigma}{d\eta dp_T}|_{pp}} \quad (1.12)$$

where $\langle T_{AA} \rangle$ is the average nuclear thickness [16].

The nuclear modification factor compares the jet spectrum in heavy-ion collisions to the expected spectrum from the same number of superimposed pp collisions. An R_{AA} below 1 indicates a modification to the jet spectrum owing to some additional interaction present in heavy-ion collisions, and so is interpreted as evidence for the presence of a QGP. The nuclear modification factors measured by the LHC experiments are shown in Fig. 1.9.⁸ From these measurements, it can be seen that jet yields are suppressed in heavy-ion collisions at LHC energies across the entire experimentally-accessible p_T range.

⁷See **Section 4.2.1: Jets** for more details about modern jet measurement techniques.

⁸Note that while the R_{AA} is discussed here in the context of jet measurements, it can be used to study any particle or collection of particles that can be measured by a detector. See e.g. Fig. 1.11.

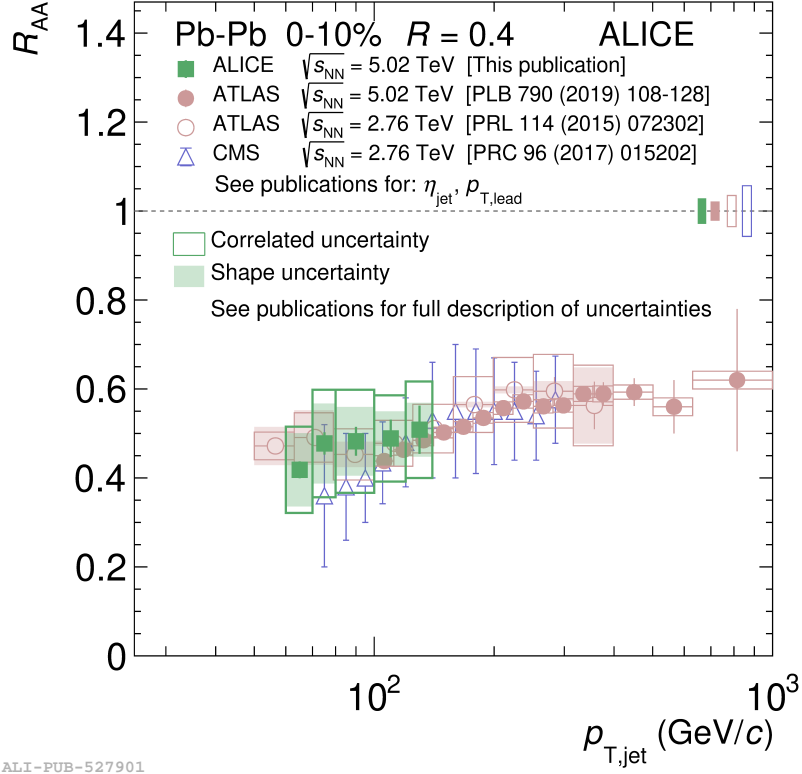


Figure 1.9: Shown are measurements of the full jet nuclear modification factor made by ALICE [20], ATLAS [21, 22], and CMS [23] in central Pb–Pb collisions.

1.5.2 Quarkonia Suppression

Another signature of deconfinement is the suppression of quarkonia yields, where quarkonia are a class of mesons consisting of a heavy-flavor quark and the corresponding anti-quark [24]. Due to the multitude of free color charges within the medium, heavy quarks experience a Debye screening effect, resulting in the “melting” of quarkonia states. Additionally, as heavy quarks are primarily produced early in the collision, these quarks undergo many of the same phenomena as jets and are thus expected to lose energy while traversing the medium. This combination of effects results in a suppression of yields in heavy-ion collisions that can be seen in Fig. 1.10 for two $c\bar{c}$ states, the J/ψ and the $\psi(2S)$. In addition to signaling the presence of a deconfined medium, the sequential suppression of excited quarkonia states can be used to illuminate various thermodynamic properties of the QGP, acting as a sort of thermometer

for the medium. Sequential suppression here refers to the fact that loosely-bound excited states (in this case, the $\psi(2S)$) are expected to melt more readily than their more tightly-bound counterparts. The transport models that describe the differences in melting rate are sensitive to various thermodynamic inputs, thus enabling better characterization of the QGP.

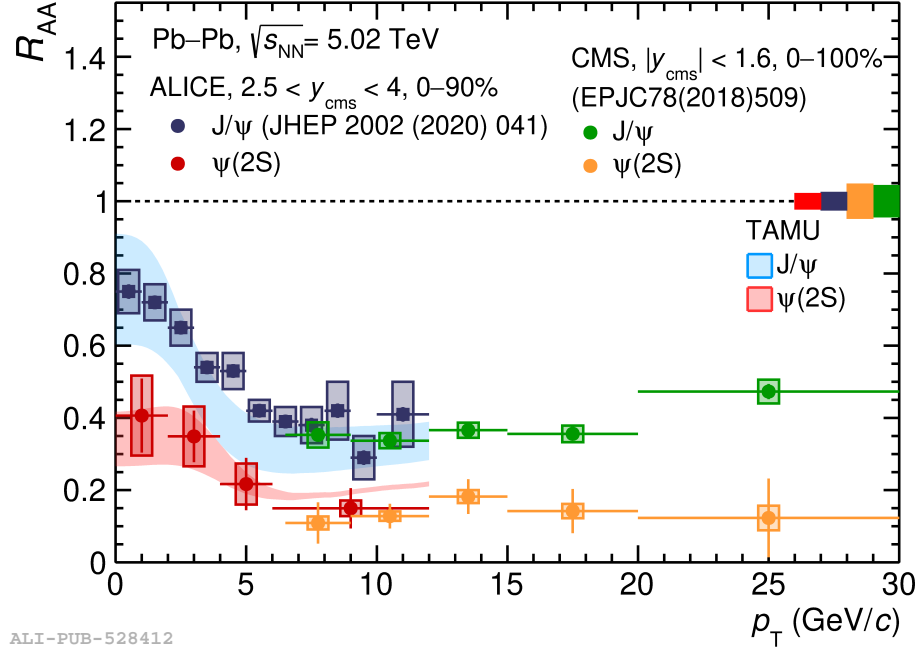


Figure 1.10: Nuclear modification factors for J/ψ and $\psi(2S)$ mesons as measured by ALICE [25] and CMS [26].

1.5.3 Strangeness Enhancement

Strangeness enhancement refers to the excess production of (multi-)strange hadrons observed in heavy-ion collisions relative to their non-strange counterparts [27], as seen in Fig. 1.11. This phenomenon can be understood by considering the processes that contribute to strangeness production. While there are no strange valence quarks in the colliding nuclei, they are light enough ($95 \text{ MeV}/c^2$) to be produced in abundance throughout the collision. These produced quarks eventually hadronize with the rest of the medium, leading to the above-described excess. Notably, similar signatures have been observed in small systems [28], raising the possibility that strangeness enhancement is a multiplicity-dependent phenomenon rather than a true signature

of QGP formation. Alternatively, these results can be interpreted as evidence of deconfinement in small systems.

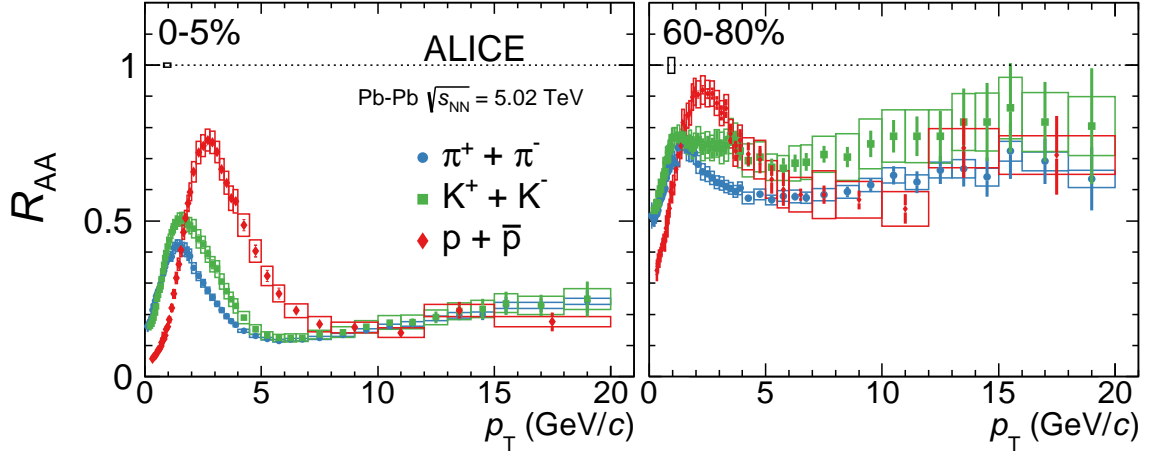


Figure 1.11: Nuclear modification factors of light hadrons for central (left) and peripheral (right) Pb–Pb collisions. Note that the kaon yields (green) are less suppressed than their non-strange pion counterparts (blue) [29].

1.5.4 Hydrodynamic Flow

A final signature of QGP formation is the presence of collective behavior, as measured by azimuthal anisotropies in the final-state particle spectra. This collectivity is often referred to as “flow” because it can be well-described by hydrodynamic theories. The relevance of hydrodynamics to heavy-ion collisions may not be immediately apparent, but can be understood by considering the overlap region of the collision. For all but the most central events, this region is anisotropic, having a rough almond shape.⁹ If a deconfined medium is achieved, this asymmetry will result in pressure gradients throughout that medium. The initial-state spatial anisotropies will thus be transformed into final-state momentum anisotropies. This evolution of the system from initial- to final-state follows a hydrodynamic expansion where energy and momentum conservation are imposed:

⁹Note that even in ultra-central collisions, fluctuations often produce significant anisotropies. However, the simplified picture of the almond overlap is helpful for understanding the origin of hydrodynamic behavior.

$$\partial_\mu T^{\mu\nu} = 0 \quad (1.13)$$

with $T^{\mu\nu}$ being the energy-momentum tensor. It can be written as:

$$T^{\mu\nu} = \varepsilon u^\mu u^\nu - (P + \Pi)(g^{\mu\nu} - u^\mu u^\nu) + \pi^{\mu\nu} \quad (1.14)$$

where ε is the energy density, u are the fluid velocity fields, P is the pressure, Π is the bulk dissipative term, $g^{\mu\nu}$ is the metric tensor, and $\pi^{\mu\nu}$ is the shear stress tensor.

Experimentally, this hydrodynamic evolution can be observed in the distribution of particles that appears in the detector. These final-state particles can be described using a Fourier decomposition in momentum-space:

$$E \frac{d^3N}{d^3p} = \frac{1}{2\pi} \frac{d^2N}{p_T dp_T dy} [1 + \sum 2v_n \cos(n(\varphi - \psi_n))] \quad (1.15)$$

where φ is the azimuthal angle and ψ_n is the n^{th} order reaction plane, defined as:

$$\psi_n = \frac{1}{n} \tan^{-1} \left[\frac{\langle \sin(n\varphi) \rangle}{\langle \cos(n\varphi) \rangle} \right] \quad (1.16)$$

The v_n are important observables often referred to as the flow harmonics. A geometric depiction of these harmonics can be seen in Fig. 1.12 (left), with a summary of values measured by ALICE shown in Fig. 1.12 (right).

1.6 QGP Properties

The top left corner of the QCD phase diagram (shown in Fig. 1.13), where temperatures are high and baryo-chemical potentials (μ_B) are low, is the region of phase space uniquely accessible to ion colliders. Most matter along this low μ_B axis is consigned to exist in a bound hadronic state; it is only at extremely high temperatures (above ~ 155 MeV, corresponding to $\sim 10^{12}$ K [33]¹⁰) that this bound state undergoes a

¹⁰These calculations were performed using lattice QCD. While a detailed discussion of lattice is beyond the scope of this thesis, see [34] for an introduction to the topic.

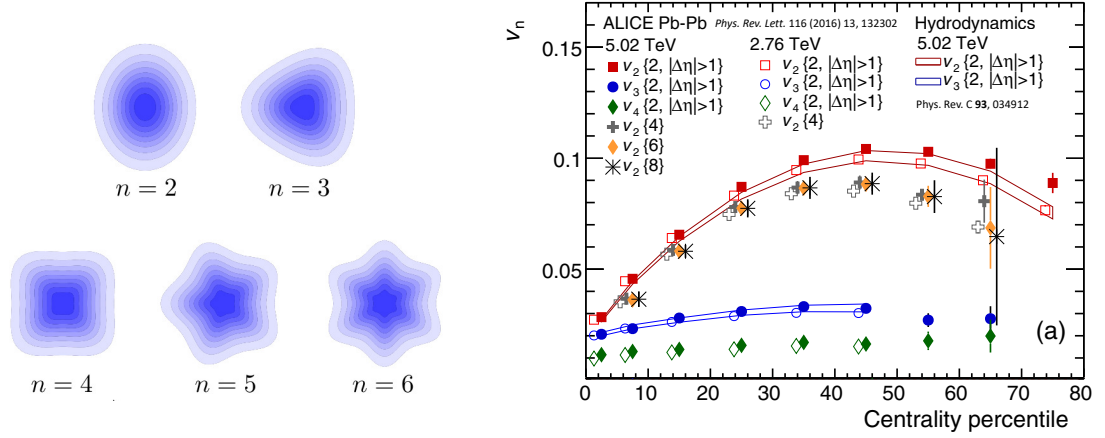


Figure 1.12: Left: Geometric depictions of harmonics 2-6. Image taken from [30]. Right: Measurements of v_2 - v_4 made by ALICE. Figure taken from [31], with hydrodynamics predictions from [32].

crossover transition to become deconfined partonic matter. Due to the extreme conditions required to escape the hadronic phase, many open questions remain regarding the QCD phase diagram. For example, is there a critical point, and if so, where is it? In the bottom right of the diagram, where baryo-chemical potentials are high and temperatures are low (a region occupied by e.g. neutron stars), is there deconfined matter mirroring the QGP? The extreme conditions required to explore these questions pose great challenges to experimentalists seeking to study the QCD phase diagram. With the use of heavy-ion colliders, however, the field has made substantial progress in characterizing the QGP of the top left corner. A brief summary of these characteristics will be discussed in this section.

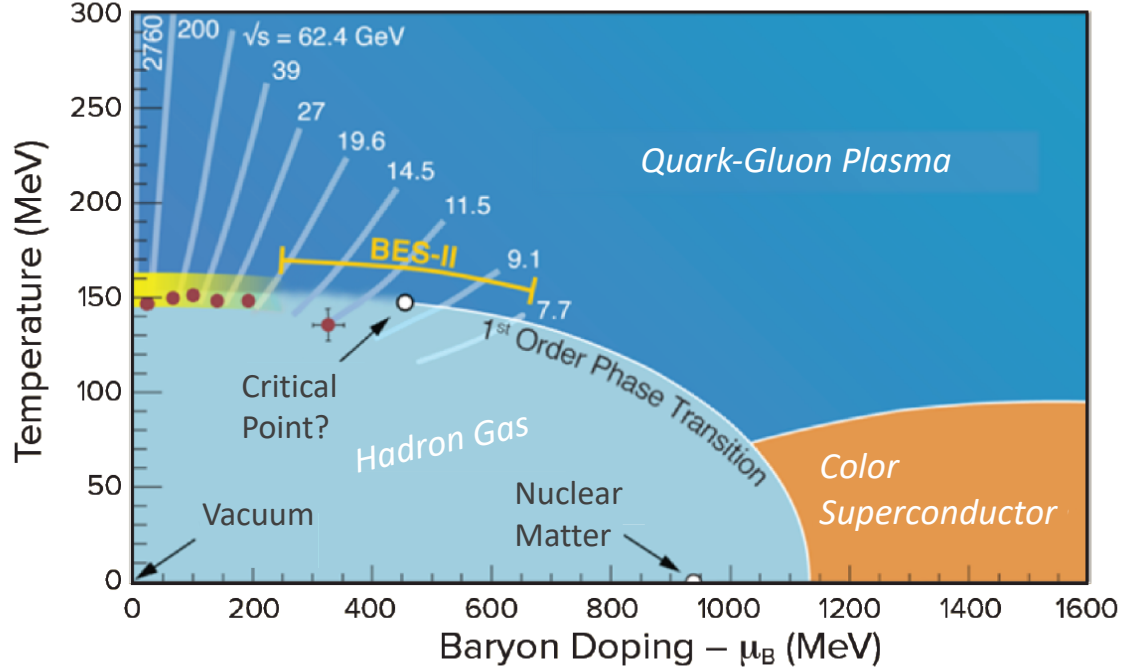


Figure 1.13: Phase diagram of QCD. QGPs produced at the LHC occupy the region around the upper y-axis. Figure taken from [35].

1.6.1 Temperature

The temperature of the QGP is a difficult concept to define, due to inhomogeneities in the initial state. It is also difficult to measure, given that any QGP produced at a collider undergoes an evolution as it cools down from its peak temperature and approaches freeze-out. There are, however, several key temperatures that can be associated with the various phases of a heavy-ion collision. The first is the critical temperature T_c , where hadronic matter undergoes a phase transition to deconfined partonic matter. This value is ~ 155 MeV. There is also the effective temperature, T_{eff} , which is a time-averaged quantity that can be measured using thermal photons. See Fig. 1.14 (left) for a summary of these temperatures and their constraints based on ALICE measurements.

1.6.2 Shear and Bulk Viscosity

A fluid’s viscosity is a measure of how well it resists flow. In the context of relativistic hydrodynamics, there are two types of viscosity: shear and bulk. Shear viscosity η can be thought of as a fluid’s resistance to deformation, and reduces the conversion efficiency from spatial anisotropies to final-state momentum anisotropies [36]. A fluid’s bulk velocity ζ can be thought of as its resistance to expansion. The QGP has the lowest shear viscosity to entropy ratio ever measured, earning it the moniker of the “perfect liquid”. Fig. 1.14 (right) shows these viscosity to entropy ratios as a function of temperature.

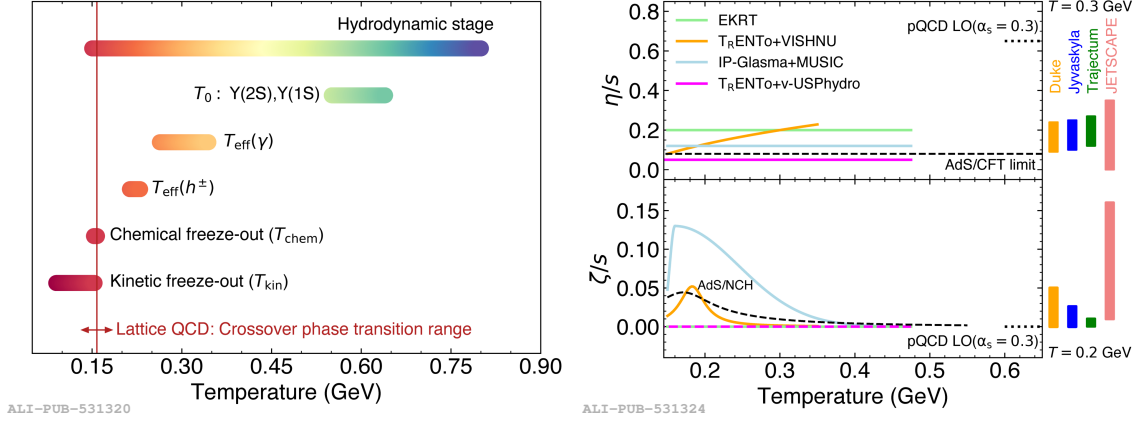


Figure 1.14: Left: Summary of relevant temperatures in a heavy-ion collision. Right: η/s and ζ/s as a function of temperature. Figures taken from [37].

1.7 Multiscale Studies

As described in this chapter, the field of heavy ions has provided many unique insights into the nature of high-temperature QCD. There remains much to be understood, however, about the interplay of QCD objects at varying scales. For example, the mechanisms that underlie jet interactions with the QGP are the subject of significant ongoing studies. While it is generally accepted that jets lose energy as they traverse the QGP, the details of how and why this happens remain unclear. This section will discuss the motivation for studying the pathlength dependence of jet quenching and how such knowledge would allow us to better understand QCD interactions at

multiple scales. It will then provide an overview of the work done in this thesis to contribute to our understanding of pathlength-dependent energy loss.

1.7.1 Pathlength Dependence of Jet Quenching

As jets traverse the QGP medium, they are expected to lose energy in a pathlength-dependent manner:

$$\frac{\Delta E}{E} \sim L^b \quad (1.17)$$

where $\Delta E/E$ is the fraction of energy lost, L is the pathlength traversed, and b is the dependence parameter. Constraining the dependence parameter b is of particular interest, given that it is related to the microscopic mechanisms by which this energy loss occurs. Assuming a static medium, collisional mechanisms are expected to correspond to $b = 1$, with radiative mechanisms corresponding to $b = 2$. Additionally, non-perturbative processes can be calculated using AdS/CFT, which corresponds to $b = 3$.¹¹ Pictorial representations of these processes are illustrated in Fig. 1.15.¹² In reality, multiple of these mechanisms are expected to contribute to the phenomenology of jet quenching, with their relative fractions being p_T -dependent. Providing experimental constraints to the pathlength dependence of jet quenching will thus allow us to better understand how jet energy loss occurs, and is therefore of general interest to the field.

Despite the strong theoretical motivation for pursuing these studies, there are significant experimental challenges that have thus far prevented an explicit characterization of b . These challenges primarily arise from the fact that we only have access to final-state particles, and are thus unable to identify the properties possessed by any given jet before it traversed the medium. For example, it is impossible to specify a jet's spatial origin, making it impossible to identify the path it followed through the QGP. Even if this could be done, inhomogeneities in the medium (i.e. hot spots of

¹¹Note that the L^3 dependence is commonly quoted, but likely only valid in a fairly restricted phase space. See **Section 3.1.3: Models** for more details.

¹²Note that these integer parameters are a simplification, but are useful for thinking about the relative contributions in a simplified system.

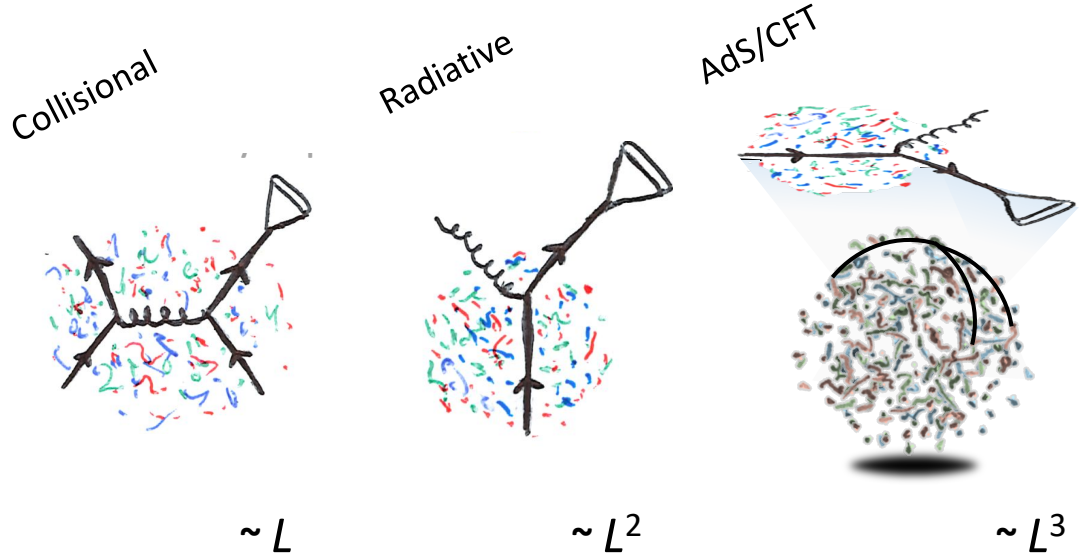


Figure 1.15: Feynman diagrams for collisional (left) and radiative (middle) jet energy loss for quark-initiated jets. A visual representation of energy loss from AdS/CFT processes (right). The cones represent the final-state hadrons. See **Section: 3.1.1: Mechanisms** for more details on these mechanisms.

high entropy density) make it difficult to unambiguously define the concept of path-length in geometric terms. Finally, interactions between the parton shower and the medium are probabilistic, thus smearing out the distribution of energy loss that any given parton could undergo. Creative methods must therefore be used to circumvent these problems and extract physics from our data.¹³ In this thesis, we use a technique known as Event-Shape Engineering (ESE) [38] to reduce medium fluctuations in our sample and provide further constraints to pathlength-dependent quenching.

1.7.2 An Introduction to Event-Shape Engineering

As discussed in the section above, medium fluctuations pose a difficulty to constraining the length of QGP that any given jet traverses. ESE, a technique that allows for one to select samples of events based on their shapes in addition to their central-

¹³It should be noted here that extracting such constraints requires input from both theory and experiment. One of the most promising ways to make this bridge can be found in software packages that describe heavy-ion behavior using Bayesian inference, where experimental measurements are used as inputs to extract relevant physics parameters.

ities, is one approach that can be used to reduce these fluctuations. This method relies on the fact that centrality and shape are related, but independent, concepts. As described in **Section 1.4.2: Centrality**, centrality is a proxy for the impact parameter. Due to the geometry of the overlap region, central events tend to be more circular while peripheral events tend to be more elliptical. Experimentally, however, centrality is determined using the multiplicity measured in the forward scintillating detectors. This value is insensitive to fluctuations in the spatial positions of incoming nucleons. Given this, event shape can be more directly measured by quantifying the harmonics described in **Section 1.5.4: Hydrodynamic Flow**. Experimentally, we find that when holding centrality constant, we are able to see significant variations in these harmonics. A sketch of this concept can be seen in Fig. 1.16.

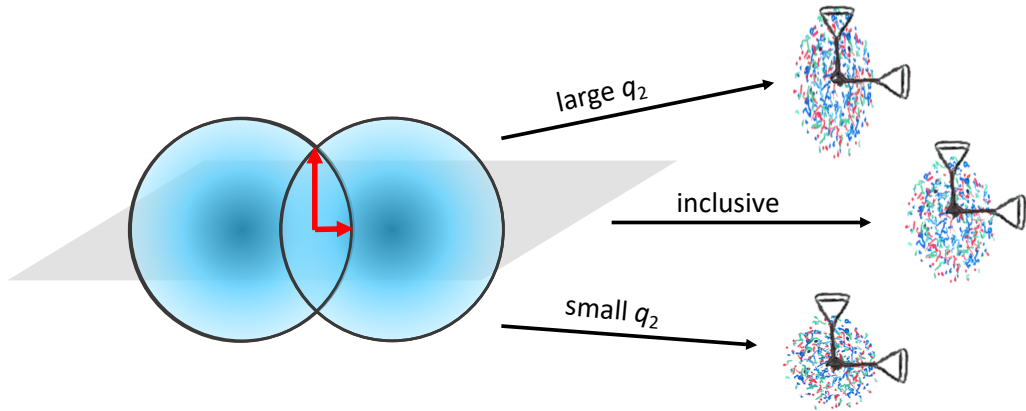


Figure 1.16: Sketch of a semicentral event. Such events, being defined by their forward multiplicity, can vary significantly in their spatial anisotropies. In this diagram, q_2 refers to the magnitude of the reduced second-harmonic flow vector. See **Section 4.2.2: Event Ellipticity** for more details.

While shape fluctuations may initially seem a nuisance, they provide experimenters an additional dial by which to study the behavior of the QGP. In the case of jet energy loss studies, they enable us to further constrain the pathlengths that jet populations traverse. Consider that, by applying an additional shape cut, one is able to select events that are more circular or more elliptical than the average of the inclusive sample. By applying further differential cuts, such as, e.g. in the jet angle

relative to ψ_2 , one is able to more precisely constrain the amount of medium that is available for a jet to pass through. This can be understood by remembering that in-plane pathlengths are, on average, shorter than out-of-plane pathlengths, a difference that is enhanced in elliptical events and suppressed in isotropic events. To the extent that jet energy loss depends significantly on the pathlength traversed, out-of-plane jets are therefore likely to be relatively more suppressed than in-plane jets in elliptical events than in isotropic events. Studying these differences thus has the possibility to provide more insight into the pathlength dependence of jet quenching than studying in-plane and out-of-plane spectra for inclusive events. The phenomenological justifications for these claims will be discussed in more detail in **Section 3.3: Trajectum - A Case Study**. In the meantime, this intuitive picture is useful for constructing observables that will inform us beyond those that have already been measured.

*“If we knew what it was we were doing, it would not
be called research, would it?”*

— Albert Einstein

Chapter 2

The Experiment

Quantum chromodynamics is responsible for phenomena as fundamental as the stability of the atoms that compose us, yet studying the high-temperature frontiers of QCD can only be done in the laboratory by way of heavy-ion collisions. This research requires a coordinated system of accelerators, detectors, and computing infrastructure, thus necessitating the collective effort of large groups of people. Experimental collaborations of this variety are typically composed of thousands of scientists, engineers, and technicians. Currently, the scale of these efforts is such that relativistic heavy-ion experiments only occur at two locations on the planet: the Large Hadron Collider (LHC) in Switzerland and the Relativistic Heavy Ion Collider (RHIC) on Long Island.

This chapter will discuss the Large Hadron Collider and the facilities used for generating heavy-ion beams. Next, it will introduce the ALICE detector, covering the specific sub-detector systems of interest to this thesis. Some upgrades for Run 3, and the specific contributions of the Yale group, will also be discussed. Finally, a brief discussion of triggering and data selection will be had.

2.1 The Large Hadron Collider

The Large Hadron Collider (LHC) is a 27-kilometer circumference ring that is buried approximately 100m underground along the border of Switzerland and France. At the LHC, charged nuclei are accelerated to near light-speed and collided at designated crossing points along the beam. There are four such collision points, each of which is home to a major experiment: ALICE (A Large Ion Collider Experiment) [39], LHCb (Large Hadron Collider-beauty) [40], CMS (Compact Muon Solenoid) [41], and ATLAS (A Toroidal LHC Apparatus) [42]. While the bulk of the LHC program is dedicated to colliding protons, the accelerator system is configured for approximately one month per year to add Pb ions into the rotation.¹ These so-called heavy-ion collisions are the subject of a rich and diverse field of physics, as well as the subject of this thesis.

Several facilities are required to prepare the ions for injection into the main ring of the LHC [43]. The heavy-ion beam begins at Linear Accelerator 3 (LINAC3), where ions are generated by an Electron Cyclotron Resonance (ECR) source, separated into long bunches, and accelerated to low energies of about 4 MeV. From here, they enter the Low Energy Ion Ring (LEIR), where the long pulses are compressed into shorter bunches and accelerated to an energy of 72 MeV [44]. Next, ions are fed to the Proton Synchrotron (PS) [45], which can accelerate particles up to 26 GeV [46]. After the PS, ions are passed to the 7 km circumference Super Proton Synchrotron (SPS), which can achieve beam energies of up to 450 GeV [47].² Upon exiting the SPS, the ions are finally ready to be injected into the LHC. A schematic of this complex can be seen in Fig. 2.1

Once inside the LHC, the ions enter two vacuum tubes in which they rotate in opposite directions, only crossing at designated points. The LHC ring itself consists of eight arcs separated by eight insertions. These arcs are composed of 154 dipole

¹Note that the LHC heavy-ion program is not limited to Pb. For example, a Xe–Xe run occurred in 2017, and there are plans for an O–O run in Run 3. However, Pb–Pb collisions form the most significant part of this program.

²The top energies quoted here for the PS and SPS were achieved with pp beams; typical heavy-ion energies are considerably lower.

The CERN accelerator complex *Complexe des accélérateurs du CERN*

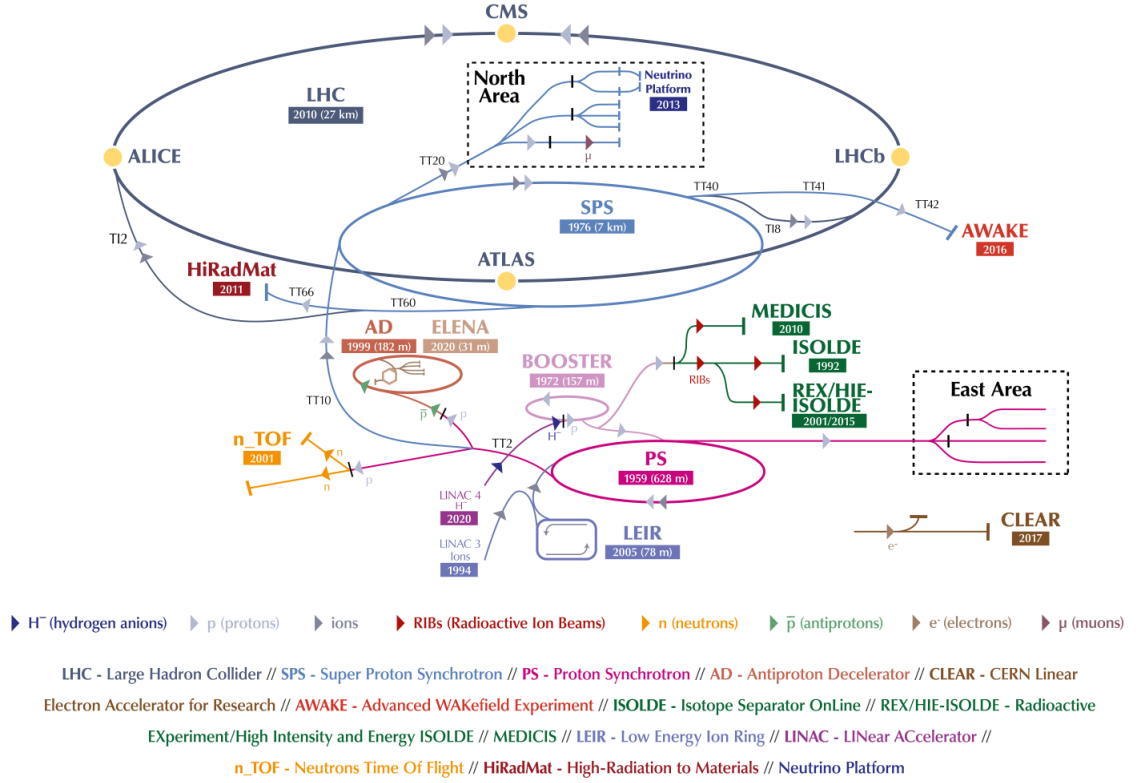


Figure 2.1: Schematic of the accelerator complex at CERN. See text for details. Figure taken from [48].

magnets each and generate a magnetic field of up to 8.3 T. This design allows the LHC to achieve top collision energies of $\sqrt{s} = 14$ TeV for proton beams³ and $\sqrt{s_{NN}} = 5.02$ TeV for Pb-ion beams, with a nominal luminosity of $\mathcal{L} = 10^{34} \text{ cm}^{-2}\text{s}^{-1}$.

2.2 ALICE

The ALICE detector is a multi-component particle detector designed to perform well in the chaotic heavy-ion environment, where thousands of particles are generated per collision [37]. A schematic of the various detector components can be seen in Fig. 2.2. Of particular note are the Time Projection Chamber (TPC) and Inner Tracking Sys-

³Note that this has not yet been achieved, with the highest energy pp collisions to date clocking in at $\sqrt{s} = 13.6$ TeV!

tem (ITS), which together form the Central Barrel used for charged particle tracking. Additionally, the V0 detectors allow for the measurement of charged particles at forward rapidities, thus enabling centrality and event-plane angle determinations. These sub-detectors, being necessary for the analysis presented in this thesis, will be discussed here in more detail.

THE ALICE DETECTOR

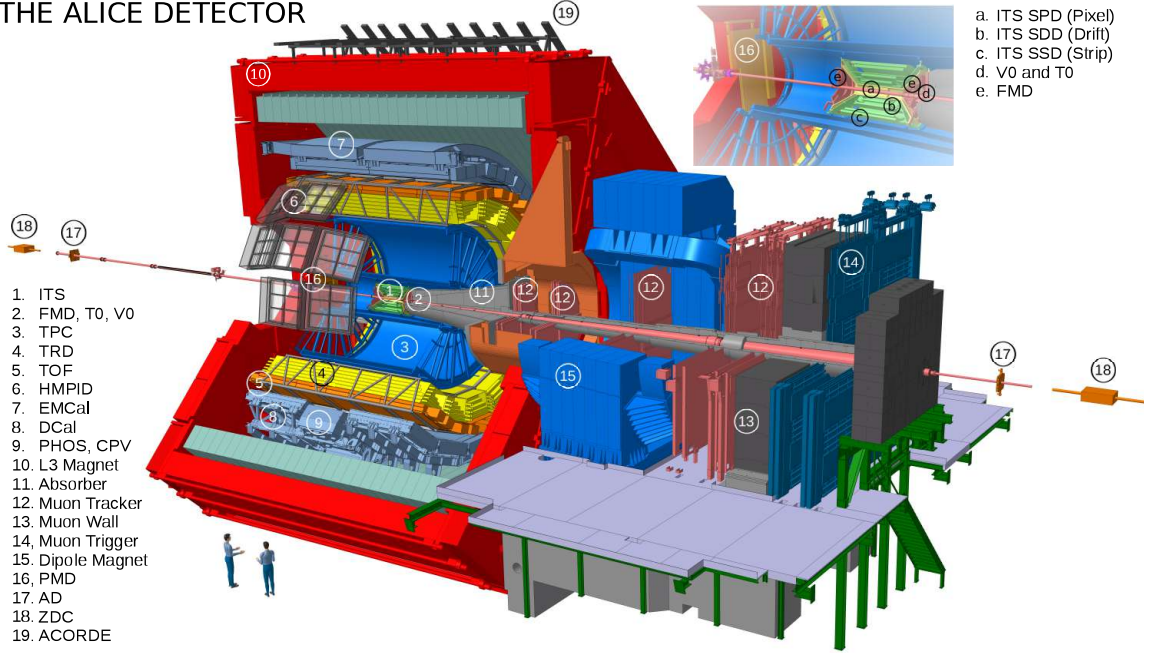


Figure 2.2: The ALICE apparatus as configured for Run 2. Numbers indicate locations of the various sub-detector systems. The central barrel (1 and 3) and forward scintillators (2) are particularly important for this thesis. Figure taken from [49].

2.2.1 Time Projection Chamber

General Information

The TPC, a gaseous detector that allows for the reconstruction of charged-particle tracks, is the prized detector of the ALICE experiment [50]. It provides high resolution tracking of charged particles in the low- to intermediate- p_T range. This enables the extensive and innovative correlation and flow-type studies that are performed using ALICE data, as well as state-of-the-art measurements of jet substructure [51, 52]. For the purposes of this thesis, the ability to combine soft information with the inclusive

jet spectrum is of highest importance.

The mechanism of a TPC is as follows. When a collision occurs in the beam-pipe, a multitude of particles propagates outward. A magnetic field generated by ALICE's solenoid magnet is applied throughout the detector, altering the trajectories of any charged particles produced by the collision such that they take a curved path through the TPC volume. These charged particles ionize the detector gas molecules along their trajectories, leaving tracks of liberated electrons in their wake. An electric field is applied throughout the TPC, directing these electrons from the center of the detector toward its end-caps. Here, the electrons undergo avalanche multiplication until they are of sufficient magnitude to form a detectable signal, which is then processed by the front-end electronics and converted to a digital signal. A schematic of this process can be seen in Fig. 2.3.

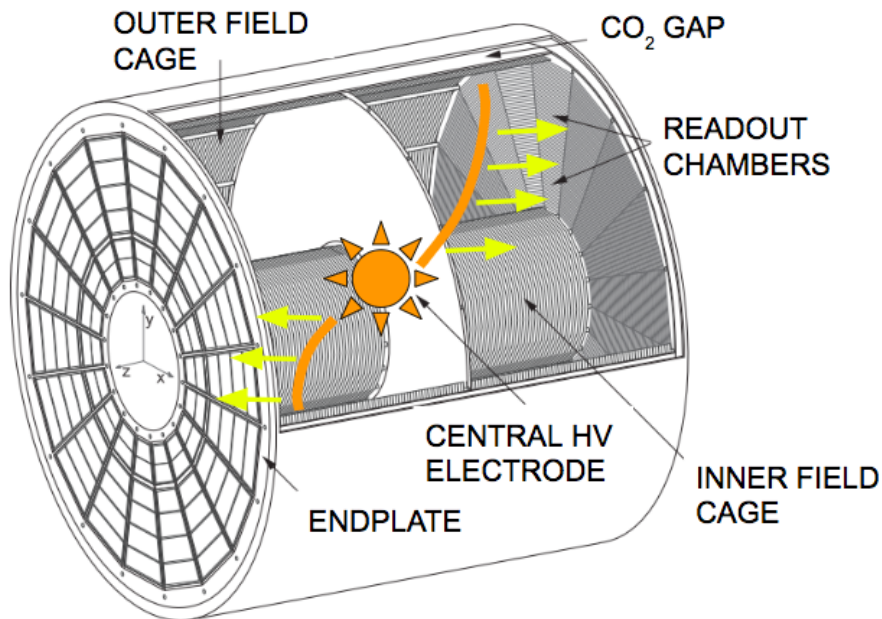


Figure 2.3: Schematic of the ALICE TPC. Note that for Run 2 and earlier, the endplates were composed of gating grids. For Run 3, they have been upgraded to quad-GEM structures. Sketch modified from the Upgrade TDR [50].

The ALICE TPC is 5.1 m in length and covers 2π in azimuth for a pseudorapidity range of $|\eta| < 0.9$. For Run 2, the gas mixture used in the drift volume consisted of Ar and CO₂ (88-12) [53], with charged tracks in the volume being subject to a magnetic field of 0.5 T. The readout plane used a gating grid to minimize ion backflow and

the resulting space-charge distortions. For Run 3, the gating grid has been replaced with a quad-GEM structure to allow for continuous readout in the high-luminosity environment [54].

Micro-Pattern Gaseous Detectors

Micro-Pattern Gaseous Detectors (MPGDs) are a class of detectors that can be used to collect signal at a TPC's readout plane. As the name implies, these detectors are small gaseous devices with intricate electronics, and include technologies such as the Gas Electron Multiplier (GEM) [54] and the MicroMegas [55]. They are typically designed to optimize for energy resolution and ion-backflow (IBF). Here, IBF refers to a phenomenon resulting from avalanche multiplication, where each new electron leaves behind a positive ion that can drift back into the detector volume and cause space-charge distortions (SCD). These distortions can alter the trajectories of tracks, thus degrading the data quality. The structural design of MPGDs allows them to excel at high-interaction rate data acquisition due to their ability to block ions in an untriggered manner.

As part of the upgrades made during the Long Shutdown preceding Run 3, ALICE has moved to using GEMs in place of a gating grid. GEMs are thin polymer foils with copper coatings. These sheets are perforated with channels for electrons to pass through. An electric field is applied across the channels to induce avalanche multiplication of the passing electrons. This field also induces escaping ions to collect on the surface of the GEM (as opposed to moving back into the drift chamber). A schematic of a GEM can be seen in Fig. 2.4 (left).

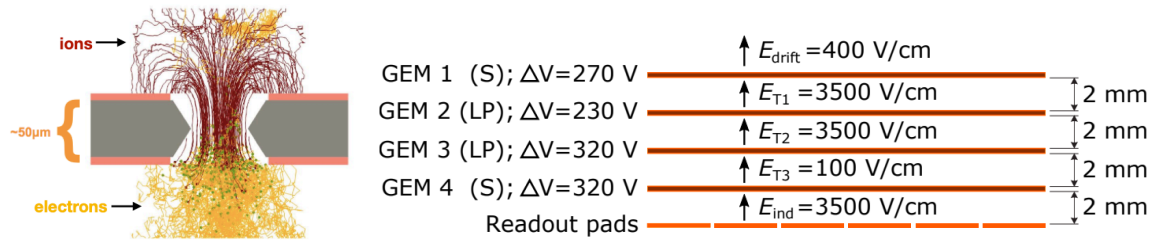


Figure 2.4: Left: A diagram of a GEM. Figure taken from [50]. Right: Schematic of the quad-GEM structure used for ALICE's Run 3. Figure taken from [56].

The specific devices employed by ALICE are quad-GEM structures consisting of four layers of GEM sheets with offset perforations. This design has been shown in R&D studies to achieve a gain of ~ 2000 while keeping IBF below 1%. A schematic of this structure with the operating conditions to be used in Run 3 can be seen in Fig. 2.4 (right). Note that the performance of such an MPGD system depends heavily on the operating conditions employed. For example, using different voltages, pitches, and foil widths can all impact the performance. Moreover, optimizing for IBF usually comes with a trade-off in energy resolution, and vice versa. A study of energy resolution vs. IBF as a function of various voltages can be seen in Fig. 2.5 (left). A separate study as a function of different gas mixtures can be seen in Fig. 2.5 (right) (note that this study was performed by Yale RHIG members [57]). Generally, curves that sit in the lower left corner are considered to have the best optimization, and guide the choices of operating conditions for the experiment.

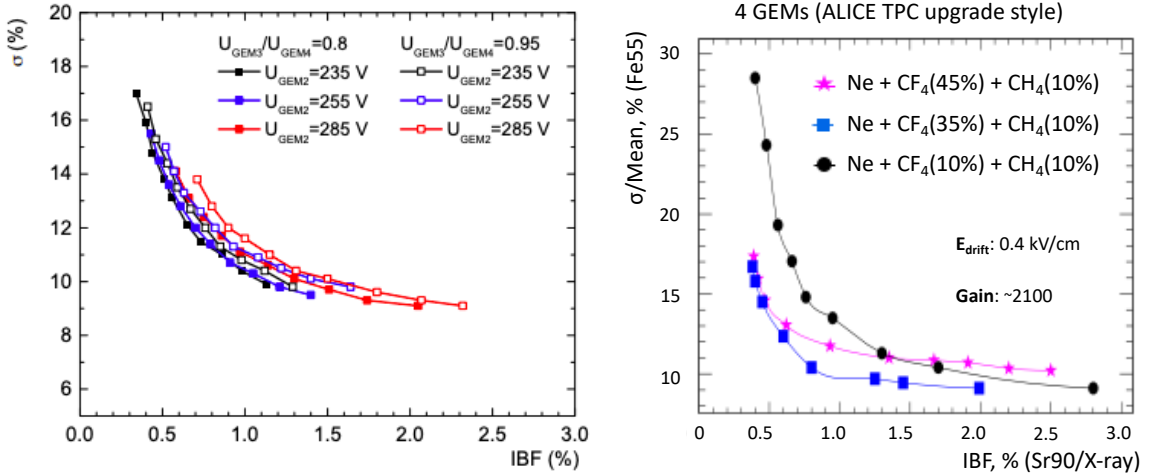


Figure 2.5: Left: Resolution vs. IBF for different voltage configurations, taken from [58]. Right: Resolution vs. ion back-flow for various gas configurations. Studies performed by Yale RHIG members in collaboration with colleagues from BNL [57].

Calibrations

While quad-GEM structures are capable of suppressing IBF in high-interaction rate environments, such environments still generate sufficient IBF to induce significant space-charge distortions (SCD). These distortions require that tracks be calibrated in

order to preserve the quality of the data. One method proposed to address the SCD in Run 3 and perform the necessary track calibrations involves the use of machine learning. The method works as follows. First, the TPC signal is converted into 1D Integrated Direct Currents (IDCs) by integrating over r and φ . This produces a z -dependent function, where one IDC value is available per time-step. These IDCs are then transformed into a series of coefficients using a Fourier decomposition. The use of Fourier decomposition allows for an initial reduction in the data size, as only the first several coefficients are required to reasonably reproduce the data.

After performing the Fourier decomposition, machine learning techniques can be applied to correct the 1D IDCs for distortions. In this case, a Random Forest [59] was chosen to study the effectiveness of using machine learning models to correct for the distortions. Tests performed on simulated TPC “maps” allowed the performance of the Random Forest to be evaluated by comparing this technique to the “true” correction. An example of this comparison is shown in Fig. 2.6 (left).

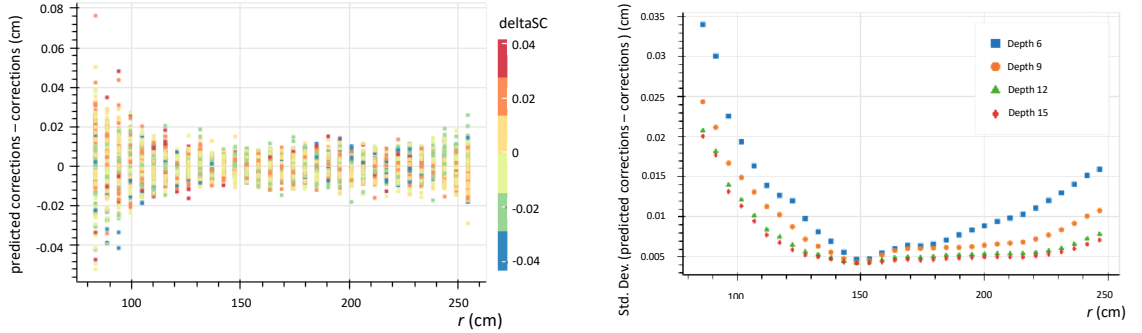


Figure 2.6: Left: Performance of machine learning corrections of TPC space-charge distortions using simulations. The difference between the correction predicted by the machine learning and the actual correction is shown as a function of the TPC r direction. The difference is on the order of 100s of microns. Right: Performance of the corrections for different reference depths. Larger reference depths improve the performance up to a value of about 12, at which point improvements begin to level off.

Studies to optimize the machine learning parameters for correcting SCD in the TPC were done as part of this thesis. These included varying the number of Fourier coefficients used in the training, the depth of the Random Forest, and the ion drift

time. Fig. 2.6 (right) shows an example of a depth study done to optimize the calibrations. Future studies in ALICE will examine these concepts further, and in particular will consider alternatives to the Random Forest approach. Ultimately, SCD corrections should achieve a precision on the order of $100\ \mu\text{m}$ [53].

2.2.2 Inner Tracking System

The Inner Tracking System (ITS), pictured in Fig. 2.7, is also critical for measuring charged tracks [60]. Tracks measured in the ITS can be matched with TPC tracks, thus allowing for better momentum parameterization and improving ALICE's overall tracking resolution. In addition, the ITS is used for locating primary vertices and reconstructing secondary vertices from heavy decays. It is a six-layered silicon detector coaxial with the beam pipe, covering pseudorapidity $|\eta| < 0.9$ (see Detector 1 in Fig. 2.2). The inner two layers are Silicon Pixel Detectors (SPD), the middle two are Silicon Drift Detectors (SDD), and the outer two are Silicon micro-Strip Detectors (SSD). In addition to the enhanced tracking capabilities enabled by the ITS, information from ITS clusters can be used for rejecting pileup events.

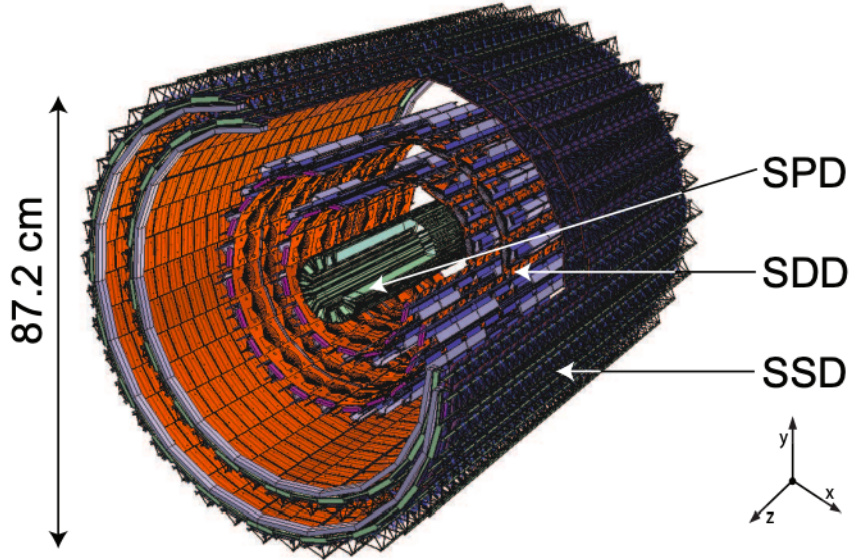


Figure 2.7: Schematic of the ITS. This detector is composed of six concentric layers of silicon material. Image taken from [60].

2.2.3 V0 Detectors

The V0 detectors are scintillating detectors in the forward region used primarily for charged multiplicity and event-plane angle determination [61]. The V0A (ATLAS-Side) is located at pseudorapidity $2.8 < \eta < 5.1$ and the V0C (CMS-Side) is located at $-3.7 < \eta < -1.7$. Together these detectors form the V0M. Each detector is divided into four concentric rings and eight azimuthal slices, as shown in Figure 2.8. The design of the V0 does not allow for the measurement of the kinematic details of the charged particles that strike the detector. However, it is adept at recording the overall multiplicity as well as the spatial distribution of these particles.

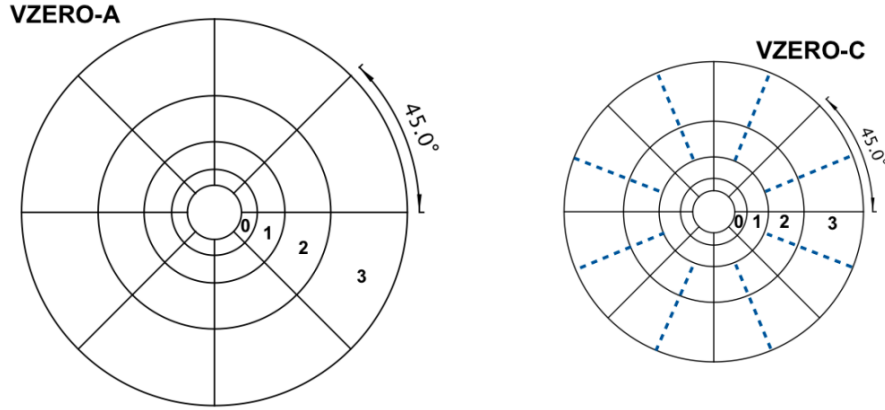


Figure 2.8: Schematic of the ALICE V0A and V0C detectors.

Centrality determination by the V0 is done by considering the summed amplitudes of the V0A and V0C, as seen in Fig. 1.6 [16]. Event-plane angle information can also be determined by considering the amplitudes of the azimuthal sections in the individual detectors. These values are then summed with an appropriate weighting determined by the resolution of the detector.

2.2.4 Triggering and Data Selection

Due to the high luminosities present at the LHC and data storage limitations, triggering systems are in place to select for data that is both “good” and “interesting” [62]. In ALICE, these triggering decisions are made by the Central Trigger Processor

(CTP) [63]. Good events are selected using a Minimum Bias trigger, which requires simultaneous signals in the V0A, V0C, and ITS detectors to reduce contamination from unwanted processes, e.g. beam-gas interactions. Rare processes are selected using the various interesting triggers. These include, for example, the High Multiplicity trigger (HM) and EMCal triggers (EJE, EGA, etc.) [64]. For the purposes of this thesis, the SemiCentral trigger was used to acquire a sample of events with increased statistics for 30-50% centrality taken during the 2018 Pb–Pb run.

After triggering, events need to pass appropriate selection criteria before being included in a measurement. First, events are typically required to have a primary vertex within $|z| < 10$ cm of the nominal interaction point. Additionally, a cut requiring a correlation between the hits in the ITS and TPC can be made to remove out-of-bunch pileup; this cut can be varied to remove pileup with various levels of efficiency. This cut removed approximately 30% of events from the analysis performed for this thesis. These cuts are intended to suppress out-of-bunch pileup, ensuring that the recorded event is associated with a true collision.

Chapter 3

Phenomenology

In the world of collider physics, relativistic heavy ions is a somewhat unique sub-field with respect to the status of and relationship between theory and experiment. Because many of high-temperature QCD’s open questions cannot be solved analytically, numerical methods are crucial for theoretical advancement. For example, lattice QCD, a technique that simulates partons on a large grid, has been used to study the thermodynamic properties of the QGP medium. More recently, Bayesian methods have been leveraged to constrain similar properties by extracting the likeliest values from existing experimental data. One common drawback of these approaches is that they require immense computing power, therefore limiting the questions they are able to address and the precision with which they are able to do so. It is consequently an exciting time to be working in heavy-ion research, where theoretical and experimental progress drive each other in tandem.

This chapter will provide a brief overview to the status of heavy-ion theory as it relates to the studies performed in this thesis. First, we will discuss the phenomenology of jet–medium interactions. Next, we will discuss simulations of the underlying event. Finally, we will give a detailed description of the Trajectum studies that have been done as a part of this thesis to investigate the use of event–shape engineering to study jet production.

3.1 Jet Quenching

As discussed in **Section 1.5.1: Jet Quenching**, jets are an important experimental signature of a deconfined medium. While medium-induced modification of the jet spectra is a generally accepted consequence of the deconfined state, the phenomenology of how and why this occurs is quite complex. In this section, we will discuss some of the common theoretical formalisms of jet quenching, the implementation of these formalisms into models, and the experimental consequences of these processes.

3.1.1 Mechanisms

There are several mechanisms by which jets can interact with the QGP medium. Perturbative QCD includes descriptions for both collisional and radiative mechanisms of energy loss. In addition to these processes, AdS/CFT (anti-de Sitter/conformal field theory) correspondence provides a description of quenching phenomena in the non-perturbative regime. The different mechanisms of jet-medium interactions and their predicted influences on the final-state jet will be described here in more detail.

Collisional energy loss refers to elastic in-medium scatterings. Most commonly, these scatterings are relatively soft, resulting in small momentum transfers. This results in an effect known as momentum broadening, where the hard fragmentation pattern of a jet softens and widens. In more rare instances, a jet parton may experience a hard “kick” from a medium particle, resulting in a significant wide-angle deflection of the incident parton. This is known as Molière scattering [65], and can be studied using observables such as the dijet acoplanarity¹ or the groomed k_T .² So far, no definitive evidence of Molière scattering has been found. Visual representations of momentum broadening and Molière scattering can be seen in Fig. 3.1.

Radiative energy loss refers to inelastic parton emissions that are induced by the medium. It is generally expected that collinear emissions of gluons will dominate

¹Acoplanarity studies consider the $\Delta\varphi$ distributions of dijets, with large deviations from $\Delta\varphi = 0$ or π being seen as evidence of in-medium scattering.

²The groomed k_T , also called the $k_{T,g}$ considers the hardness of splittings in a jet. Here, k_T is defined as $k_T = p_{T,2} \sin(\Delta R)$.

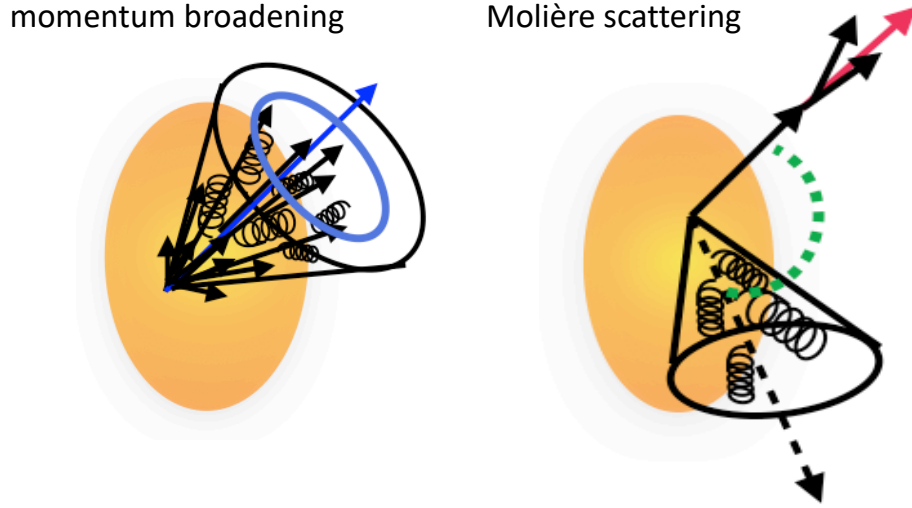


Figure 3.1: Examples of the effects of collisional energy loss. Momentum broadening (left) refers to a softening and broadening of the jet fragmentation pattern. Molière scattering refers to large, wide-angle kicks that a parton may undergo as it traverses the QGP. Diagrams taken from [66].

energy loss phenomena at high- p_T . In addition to this collinear radiation, the medium may induce wide-angle parton emissions. As in the case of collisional energy loss, these radiative processes can result in momentum broadening of the jet. Additionally, wide-angle radiations at sufficiently high momenta can generate separate jets that the medium is able to resolve independently from the original parton. The resolution length of the medium, i.e. the distance two partons must be apart from each other in order for the medium to “see” them as separate objects, is an open question in heavy-ion physics.

While collisional and radiative energy loss mechanisms are useful descriptions for understanding the ways in which energetic partons interact with the medium, they are incomplete. Notably, the mechanisms described above are perturbative in nature. In order for these descriptions to be valid, the relevant momentum exchanges must be sufficiently high and α_s correspondingly low. For this reason, we often say that collisional and radiative descriptions of jet–medium interactions are limited to the weakly-coupled limit. It is not unreasonable, however to expect that some energy loss processes are very soft, or occur after the parton has lost a significant amount of

virtuality. Because α_s is large, jet energy loss in this strongly-coupled limit is very difficult to calculate using traditional methods. In the absence of reliable traditional models, one alternative approach involves using AdS/CFT correspondence.³ The basic principle is that, in the appropriate limits, QCD can be considered equivalent to a dual gravity theory. Using this correspondence, one can perform calculations that are difficult in QCD by exploiting the simpler computational machinery of the dual gravity. This results in a calculational setup that effectively treats the medium as exerting a drag force on the passing parton. See Fig. 3.2 for a visual representation of this correspondence.

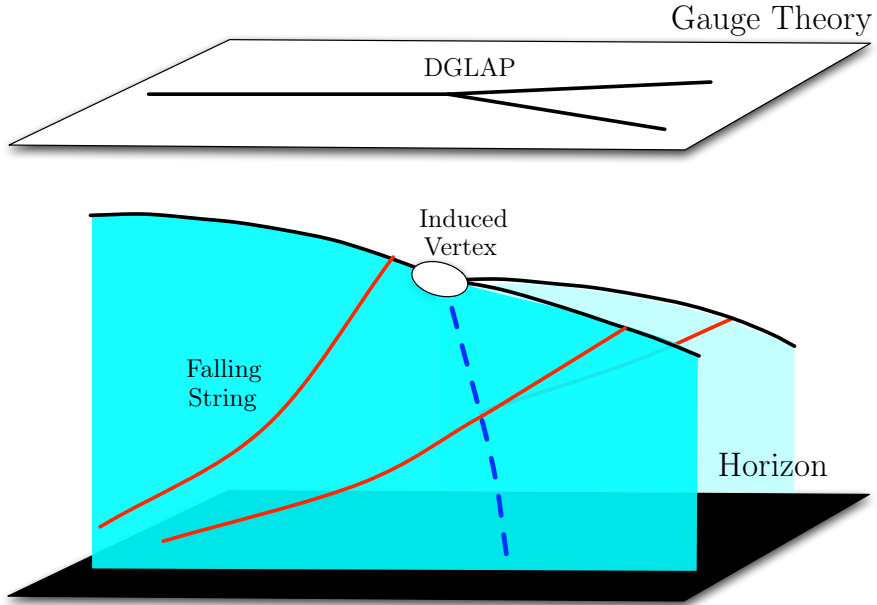


Figure 3.2: A visual representation of the AdS/CFT correspondence. The strongly coupled gauge theory is represented on the white plane above. Its correspondence to the dual gravity is shown in the higher dimensional portion below. Figure taken from [68].

In the case of simplified conditions, the mechanisms described above can be linked to explicit pathlength dependences of energy loss. These links provide a strong motivation for studying this dependence in experiment, as such can be directly mapped back to the theory of jet energy loss. Assuming a static medium, the collisional energy loss mechanism has a linear dependence on pathlength, whereas radiative energy loss

³See [67] for a description of AdS/CFT and its relevance to jet studies.

depends quadratically on pathlength. We know, however, that the medium is not static but instead undergoes a dynamical evolution. In these circumstances, it is theorized that radiative energy loss is more realistically described by a linear dependence [69]. Generally speaking, the evolution of the medium and the hard parton over a large interval of scales complicates the simple picture. Therefore, the mechanisms described in this subsection can be more realistically incorporated into rigorous theoretical formalisms, which will be discussed below.

3.1.2 Formalisms

Modeling jet-medium interactions from first principles is a difficult task. With the mechanisms described above, one must keep in mind several complicating factors, e.g. that the parton is continuously losing virtuality and that the medium is simultaneously evolving. For this reason, there are several theoretical formulations of jet quenching that provide a more complete picture. Four such formalisms of jet energy loss are BDMPS [70], GLV [71], AMY [72], and Higher Twist [73].

The Baier-Dokshitzer-Mueller-Peigne-Schiff (BDMPS) formalism provides a description of jet-energy loss due to medium-induced gluon radiations at high- p_T . It does this by treating the QGP as multiple scattering centers, and finds that such energy loss goes as:

$$\Delta E = (\alpha_s C_R / 8) (\mu^2 / \lambda_g) L^2 \ln(L / \lambda_g) \quad (3.1)$$

where α_s is the strong coupling, C_R is the color factor, λ_g is the gluon mean-free-path, μ is the Debye screening mass, and L is the length of plasma traversed.

The Gyulassy-Levai-Vitev (GLV) approach is similar to BDMPS in its treatment of the QGP. However, instead of considering soft gluon radiations, it begins from a single hard radiation of the jet. This approach finds that energy loss should go as:

$$\Delta E = \frac{C_R \alpha_s}{N(E)} \frac{L^2 \mu^2}{\lambda_g} \log(E / \mu) \quad (3.2)$$

where $N(E)$ is a numerically determined scaling factor that accounts for kinematic constraints.

The Higher Twist and Arnold-Moore-Yaffe (AMY) formalisms take an alternate approach to BDMPS and GLV. Instead of directly predicting the total energy lost by an initiating parton, they describe jet modification in terms of the modified fragmentation of said parton. Higher Twist, originally derived for e–A collisions systems, considers multiple scatterings of the hard parton by considering “higher twist” corrections to the leading twist diagram. AMY also considers multiple scatterings in its implementation of jet quenching. In this formalism, the temperature is assumed to be very high, resulting in small α_s and the applicability of pQCD. However, this assumption limits the general applicability of the AMY formalism.

3.1.3 Models

The above section details some of the commonly used formalisms for describing jet energy loss in the medium. To compare theoretical predictions with experimental data, these formalisms are often implemented in Monte Carlo simulation packages [74]. There are many advantages to these implementations, such as the ability to tune parameters to data, the capacity to extrapolate to new observables, and the increased accessibility to experimentalists. Some of the frequently used jet quenching Monte Carlos will be presented here.

PYTHIA [75, 76] is an event generator that is commonly used to simulate pp collisions. While it does not model jet energy loss, it is nearly ubiquitously used for the vacuum parton shower, and so merits discussion here. Concerning jets, it has a well-validated approach for simulating both initial- and final-state radiations in vacuum. PYTHIA evolves these showers according to the initiating parton’s virtuality by using the following expression:

$$d\mathcal{P}_a(Q^2) = \frac{dQ^2}{Q^2} \frac{\alpha_s(Q^2)}{2\pi} \sum_{b,c} \int_{z_{\min}(Q^2)}^{z_{\max}(Q^2)} P_{a \rightarrow bc}(z) dz \quad (3.3)$$

where $d\mathcal{P}_a(Q^2)$ is the infinitesimal branching probability. Here, $P_{a \rightarrow bc}(z)$ refer to the

DGLAP splitting functions, for which PYTHIA uses:

$$P_{q \rightarrow qg}(z) = \frac{4}{3} \frac{1+z^2}{1-z} \quad (3.4)$$

$$P_{g \rightarrow gg}(z) = 3 \frac{(1-z(1-z))^2}{z(1-z)} \quad (3.5)$$

$$P_{g \rightarrow q\bar{q}}(z) = \frac{1}{2}(z^2 + (1-z)^2) \quad (3.6)$$

where z is the momentum fraction of the outgoing parton.⁴ Notably, PYTHIA also includes a probability for a no-splitting event. This is known as the Sudakov factor [77]:

$$\Pi_a(Q_1^2, Q_2^2) = \exp \left(- \int_{Q_2^2}^{Q_1^2} d\mathcal{P}_a(Q^2) \right) \quad (3.7)$$

The Sudakov expression results from taking the infinitesimal no-splitting probabilities $(1-d\mathcal{P}_a(Q^2))$ and multiplying each contribution as the parton increments in virtuality. Once the parton shower has finished, hadronization is modeled using the Lund string model [78].

JEWEL (Jet Evolution With Energy Loss) [79] is a Monte Carlo framework that can model the parton shower in vacuum (as does PYTHIA) as well as in medium. The medium-modified spectrum is produced by first simulating PYTHIA-like jets, and subsequently calculating their energy loss via collisional and radiative mechanisms. Hadronization is then implemented using the Lund string model. One drawback of JEWEL (as concerns this thesis) is that its centrality definition is equivalent to a collision's impact parameter, and thus does not account for event-by-event fluctuations.

The Hybrid Model [80], as the name implies, combines multiple formalisms to model jet-medium interactions. First, the hard scattering and parton shower are modeled using pQCD. The interactions between the partons and the medium are then prescribed using AdS/CFT correspondence, where the medium is hydrodynamically

⁴Note that these are the same DGLAP splitting functions described in **Section 1.3: Scales of QCD**. Any apparent discrepancy between these equations arises from the final-state parton which is chosen for tracking, as $z \rightarrow z - 1$ in the cases where the selection is switched.

evolving. The energy loss of the hard parton is given by the following equation:

$$\frac{1}{E_{\text{in}}} \frac{dE}{dx} = -\frac{4}{\pi} \frac{x^2}{x_{\text{stop}}^2} \frac{1}{\sqrt{x_{\text{stop}}^2 - x^2}} \quad (3.8)$$

where E_{in} is the initial energy of the hard parton, x is the thickness of the “slab” of QGP, and x_{stop} is the parton’s stopping distance. Note that the pathlength dependence of energy loss described here depends on the size of x relative to x_{stop} , which is defined as:

$$x_{\text{stop}} = \frac{2}{\kappa_{\text{SC}}} \frac{E_{\text{in}}^{1/3}}{T^{4/3}} \quad (3.9)$$

where κ_{SC} is a dimensionless constant. The Hybrid Model shows reasonable (although imperfect) agreement with results such as the jet R_{AA} and dijet asymmetry.

JETSCAPE [81] is a modern event generation software package that is intended to construct a coherent picture from the disparate efforts to understand jet quenching. A modular framework with which a complete heavy-ion event can be simulated, JETSCAPE allows the user to designate which physics implementations are of interest for the observable at hand. The jet energy loss component of JETSCAPE considers the modification of PYTHIA-like jets, where the user can choose from a variety of energy loss mechanisms, such as MARTINI [82] (an implementation based on AMY), the Hybrid Model (based on AdS/CFT), and others. While JETSCAPE is a promising software package that may eventually allow for precision comparisons of theoretical models with data, computational limitations prevent it from being particularly useful for the work done in this thesis.

3.2 Modeling the Underlying Event

The progression of a heavy-ion collision can be broken into approximately three phases: the initial state, hydrodynamic evolution, and freeze-out. Models of the underlying event generally focus on one of these stages, and can be linked together to simulate a fully realistic collision. Because jet quenching behavior is intimately coupled to the evolution of the medium, we will here discuss various details of modeling

the initial state and hydrodynamic evolution.

3.2.1 Initial State

The initial state is the first step in the chain of a heavy-ion simulation, with initial state models addressing the pre-equilibrium phase of a collision. These models assign energy density distributions to the overlap region, forming the basis from which hydrodynamics can further evolve. This is generally done by considering some aspect of the colliding nuclei to be the degrees of freedom through which inhomogeneities can be introduced, as summarized in Fig. 3.3. One of the most traditional initial state models is the Glauber model [83], which considers incoming ions as collections of independent nucleons distributed according to some realistic density function. This is commonly done using a Woods-Saxon distribution [84], which can be written as:

$$\rho(r) = \rho_0 \frac{1}{1 + e^{(r-R/a)}} \quad (3.10)$$

where ρ is the nucleon density (with ρ_0 being a normalization factor), r is the distance from the center of the nucleus, R is the radius of the nucleus, and a is a thickness parameter. Notably, such models don't account for the effects of the nuclear binding energies. For this reason, Glauber simulations are often used as a baseline with which to compare heavy-ion collisions, where observed differences between the two are seen as indicative of QGP effects.

While Glauber models are frequently used due to their simplicity, there are many other models available, several of which simulate the deconfined state. IP-Glasma [86] is one such example. Instead of considering the incoming nucleons, this model treats the incoming gluons as the primary degrees of freedom. This is implemented by using an effective field theory known as the Color Glass Condensate (CGC) [87]. Another more recently developed example is TRENTO [88], which models the initial state by depositing entropy according to a “reduced thickness” function derived from the distribution of nucleons within the colliding nuclei. Here, the nucleons are the aforementioned degrees of freedom. Given that many different types of initial-state

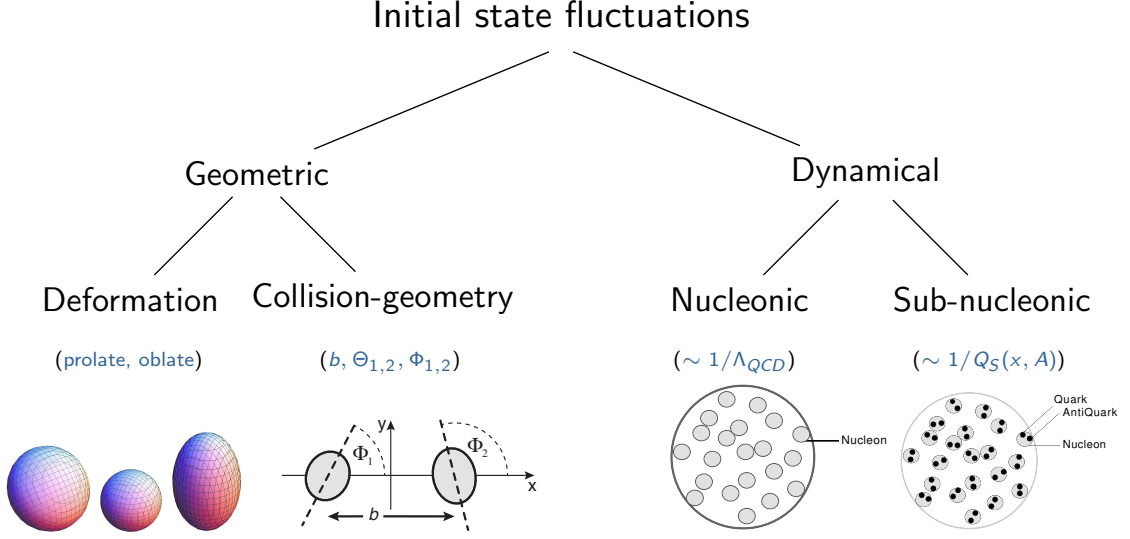


Figure 3.3: A summary of the degrees of freedom that can be considered when modeling the initial state of a heavy-ion collision. Figure taken from [85].

models with widely varying physical bases are able to reproduce experimental data, the true nature of the initial state remains an open question in the field.

3.2.2 Hydrodynamic Evolution

Successfully modeling the expansion of the medium is in some regards a more straightforward task, given that the widely-used relativistic fluid dynamics equations have had such success in describing final-state particle distributions for heavy-ion collisions. There are currently several available packages that model this stage of the collision, all of which solve Equation 1.14, rewritten here for convenience:

$$T^{\mu\nu} = \varepsilon u^\mu u^\nu - (P + \Pi)(g^{\mu\nu} - u^\mu u^\nu) + \pi^{\mu\nu} \quad (3.11)$$

Note that, while in the case of an isolated hydrodynamic system, $\partial_\mu T^{\mu\nu} = 0$, we must include a source term if we are to account for the jet-medium interaction. This constraint then becomes:

$$\partial_\mu T^{\mu\nu} = J^\nu \quad (3.12)$$

Some examples of models that can be used to reproduce the hydrodynamic behavior of heavy-ion collisions are MUSIC [89] and VISHNU [90].⁵ These models differ primarily in the approximations they use to solve the relevant differential equations and in the number of space-time dimensions they are adept at describing (i.e. 2+1D v. 3+1D).

3.2.3 Event-Shape Engineering

At this point, it may be apparent to the reader that event-by-event fluctuations are important considerations for describing the underlying event.⁶ While these fluctuations can take many forms, one particular variety of interest occurs in the form of the event shape. As shown in Fig. 3.4, events can embody a large range of ellipticities. Moreover, these differences can be observed even within very small centrality windows. This is all to say that centrality, which is experimentally determined by multiplicity (as explained in **Section 1.4.2: Centrality**), is only a very rough proxy for the event shape. Asserting precise knowledge of the event shape from centrality information alone is therefore an oversimplification.

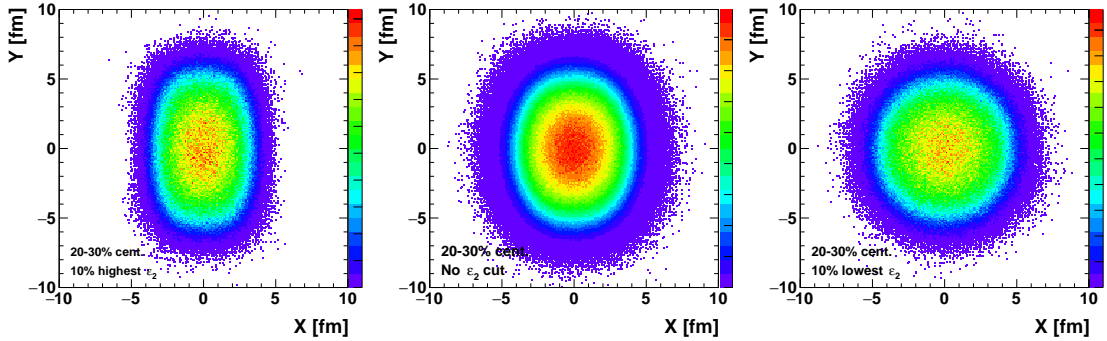


Figure 3.4: Spatial representation of the energy deposition from a heavy-ion collision using a Glauber model. Note that all plots are from the same centrality class. Figure taken from [91].

Here, the concept of Event-Shape Engineering (ESE) [38] becomes useful. ESE is a technique that allows one to select events based on their anisotropies using a

⁵Note that VISHNU is a hybrid model (not to be confused with The Hybrid Model) that simulates the hydrodynamic evolution in conjunction with a hadronic cascade.

⁶If this is not the case, I would encourage you to consider this now.

reduced harmonic flow vector.⁷ This selection is made within a centrality class so as to maximally constrain thermodynamic properties of the medium. ESE has been proposed as a way to study physics ranging from the Chiral Magnetic Effect [92] to femtoscopy [93], and offers a unique way to study jet energy loss.

To understand the application of ESE to jets, consider that one of the current limits to constraining the pathlength dependence of energy loss is the presence of medium fluctuations. These make it difficult to identify the pathlength that any given jet traverses. By using ESE, however, one can convert this weakness into a strength. Selecting events according to their shapes enables the geometry of the medium to be known with relative precision. By then considering the event-plane angles of the jets, the analyzer is able to put tighter constraints on the pathlengths traversed by those jets. The validity of this supposition will be discussed in the following section.

3.3 Trajectum: A Case Study

For the purposes of this thesis, the Trajectum framework [94] has proven to be a useful phenomenological tool. Trajectum is a heavy-ion simulation software that uses state of the art Bayesian inference to model collision properties. Even though it does not currently have a mechanism for modeling parton showers, its realistic description of the underlying event allows for it to be used to provide a better understanding of the pathlength distributions that jets can traverse. A study to contextualize the event-shape engineering measurement that is presented later in this thesis was done using Trajectum and will be discussed here in detail [95].⁸

This study was performed by simulating $2.2 \cdot 10^6$ Pb–Pb collisions at $\sqrt{s_{\text{NN}}} = 5.02$ TeV using a TRENTO initial state model with Cooper Frye freeze-out [96]. To measure the pathlength distributions of interest, non-interacting hard probes were simulated by generating back-to-back lines and propagating them outwards from each

⁷In the analysis performed for this thesis, we consider the second order harmonic flow vector. We are therefore selecting events based on the anisotropies between the semi-major and semi-minor axes of the elliptical overlap region. This sorts events by how elliptical or spherical they are.

⁸This study was performed in collaboration with Govert Nijs, Mike Sas, and Wilke van der Schee.

collision at the speed of light. Using these lines, various proxies for the pathlengths of the non-interacting probes were calculated. The consideration of multiple distinct proxies was motivated by the fact that “pathlength” is not an unambiguously defined quantity in a dynamic medium. For example, including weightings for the entropy density hotspots in the QGP results in different pathlength outputs than the use of purely geometric definitions.

The pathlength distributions for several of these definitions are shown in Fig. 3.5 (left). The first (red) is simply defined as the geometric length traversed by a non-interacting probe. The second (green) is a pathlength proxy, given by the probe’s inner product with the movement of the fluid cell. This accounts for whether the probe is traveling with or against the medium. The last definition (purple) is similar to the previous, but it also accounts for the Lorentz factor γ . Note that including the movement of the fluid cell in the computation shifts the pathlength distributions to the left, reflecting a reduction in the average amount of medium that is “seen” by the probe. This effect is also observed in Fig. 3.5 (right), where the average pathlengths (and proxies) are reported as a function of centrality. This figure shows that, across the full centrality range, the average pathlengths are reduced when they are defined to include the fluid cell movement. More importantly, the average pathlength traversed by a non-interacting probe decreases as centrality increases (i.e. as the event becomes more peripheral). This result is naively expected, given that the size of the medium is directly correlated with the centrality of the collision.

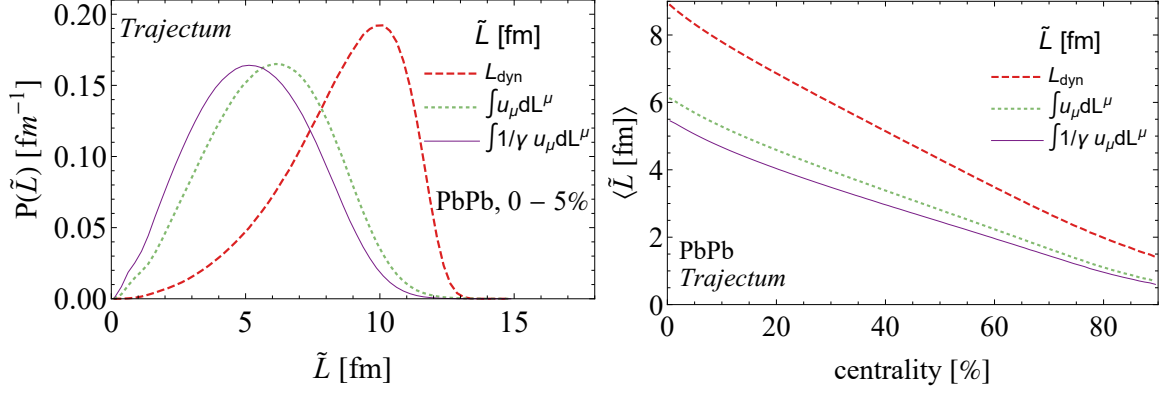


Figure 3.5: Left: Pathlength distributions calculated in Trajectum using various proxies for the length that a non-interacting hard probe would traverse. Accounting for the movement of the fluid cell shifts the pathlength distribution leftward. Right: Distribution of average pathlengths as a function of centrality. It can be seen that average pathlengths decrease as events become more peripheral. Figure taken from [95].

The results described above are for an inclusive sample of events. At this point, however, it becomes informative to incorporate ESE classes. Practically, this is done by considering the magnitudes of the harmonic flow vectors:

$$Q_n = \sum_{i=1}^M e^{in\varphi_i} \quad (3.13)$$

where n is the relevant order harmonic. To minimize any centrality bias, we can consider the reduced form of this vector:

$$q_n = \frac{|Q_n|}{\sqrt{M}} \quad (3.14)$$

Because the simulations discussed here do not include any hard-scale physics, the sum in Equation 3.13 is performed over charged particles at mid-rapidity.⁹ The average q_2 (and q_3) values are shown in Fig. 3.6 as a function of centrality. It can be seen that, even after normalizing for the number of particles, q_2 depends considerably on centrality. By contrast, q_3 remains relatively flat. This is intuitively reasonable, given that v_2 is strongly correlated with the geometry of the system, whereas v_3 arises

⁹In experiments, these sums are typically performed at forward rapidities to reduce potential auto-correlations between jets and the q_2 determination.

mainly from fluctuations in the initial state.

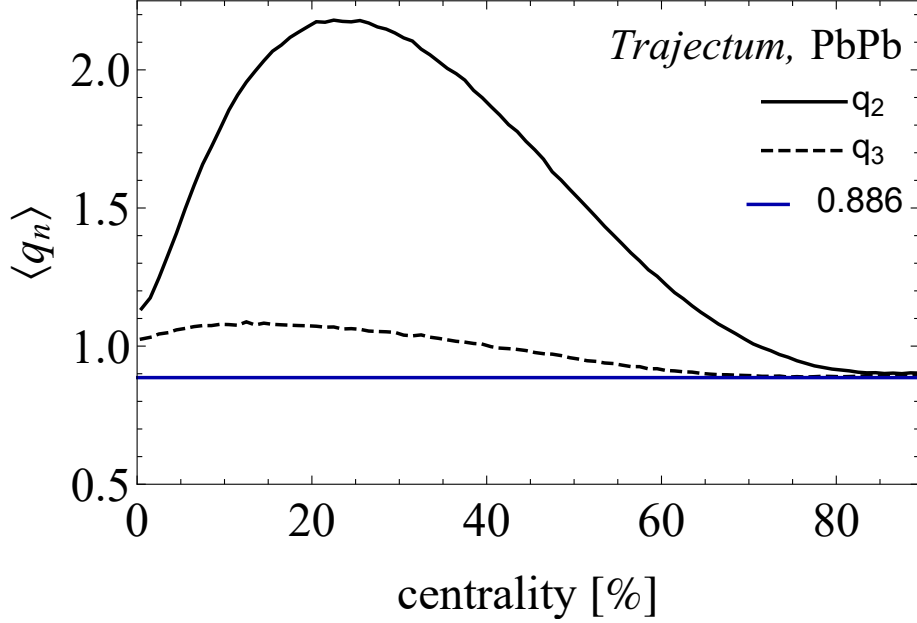


Figure 3.6: Average q_2 (q_3) as a function of centrality. Figure taken from [95].

If we look closer, however, we can see that collision geometry alone does not tell the full story. In Fig. 3.7, the probability distributions for q_2 (and q_3) are given, separated by different centrality classes. The curves are not narrowly peaked, but instead have significant widths. In particular, the 20–30% centrality class, which has the highest average q_2 of the classes shown here, also has the most significant width in q_2 . These results emphasize that a very wide distribution of anisotropies is experimentally accessible, even within a narrow centrality class. Said another way, an event’s anisotropy is not determined by collision geometry alone, but is also influenced significantly by fluctuations in the initial state.

Incorporating this information into our study of pathlength, we can consider how the average pathlength of a distribution changes for different ESE classes. Fig. 3.8 depicts the average pathlength as a function of centrality for multiple ESE classes. In this figure, the red curve represents inclusive events, the green curve represents q_2 —small events (isotropic), and the purple curve represents q_2 —large events (elliptical). It can be seen that, while the average pathlength depends strongly on centrality, it exhibits almost no dependence on the ESE class. This suggests that any differences

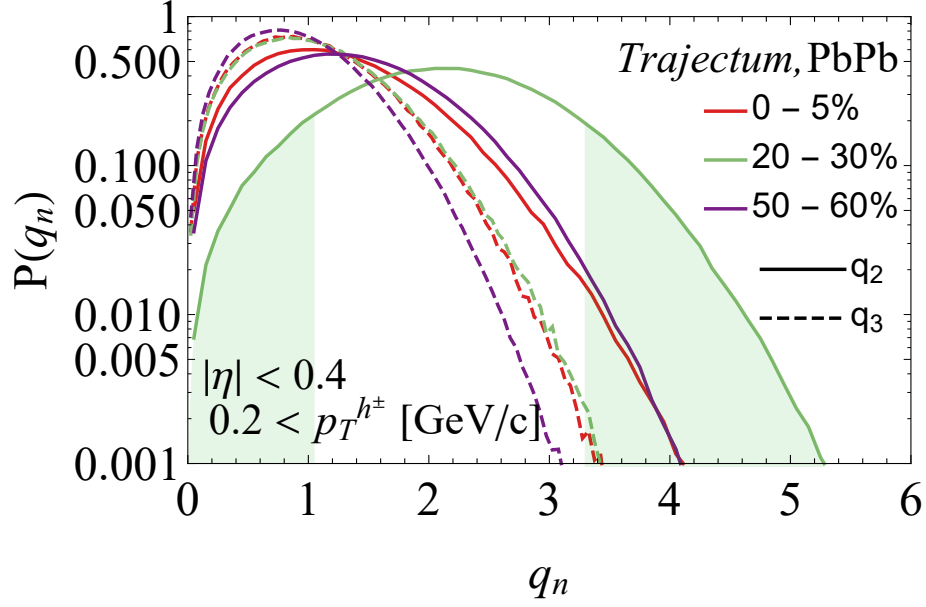


Figure 3.7: Probability of an event having a given q_2 (q_3) value for central (red), semicentral (green), and peripheral (purple) events. Figure taken from [95].

that may be observed in jet spectra between q_2 —small events and q_2 —large events are not due to differences in pathlength traversed by those jets. We must therefore consider more discriminative observables if we want to study the pathlength dependence of jet energy loss.

One such approach is to look more differentially at our ESE samples by considering the relative angle of the probe with respect to the event-plane. This is done in Fig. 3.9 for a combination of centralities. Intuitively, one expects that the in-plane axis will be shorter than the out-of-plane axis, given the almond-shaped overlap region of the collision. This assumption indeed forms the basis of many searches for azimuthally-dependent jet quenching. Experimentally, however, we only have access to final-state particles. We can therefore use Trajectum to study this phenomenon and verify our expectation that the initial state anisotropies indeed propagate to the measurement of the final state. Fig. 3.9 shows the results of this study, in which the pathlengths traversed by the non-interacting probes approximate the QGP axis lengths. It can be seen that the pathlength distributions for in-plane (solid line) probes are generally less than those for out-of-plane (dashed line) probes. Notably, this effect is more significant for more peripheral collisions, whereas for central collisions there is only

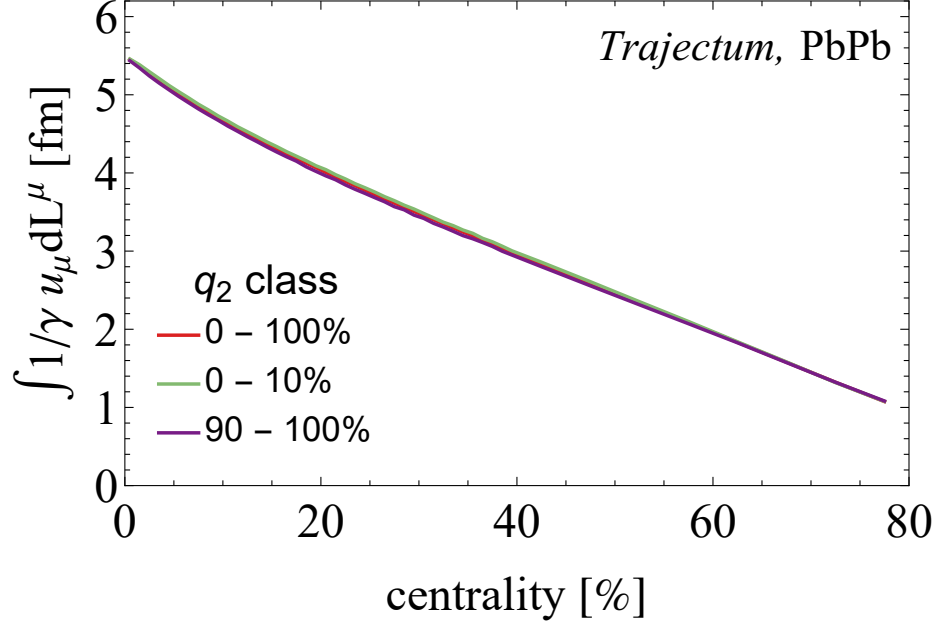


Figure 3.8: Right: Average pathlength as a function of centrality for central (green), peripheral (purple), and inclusive (red) events. Figure taken from [95].

a small shift in the distribution. Also note that this study only includes jets with $\Delta\varphi < 22^\circ$, where $\Delta\varphi = |\Psi_2 - \varphi_{\text{jet}}|$ for in-plane jets and $\Delta\varphi = |\vec{n} - \varphi_{\text{jet}}|$ for out-of-plane jets (here, \vec{n} is the vector perpendicular to Ψ_2). The observed difference supports the intuitive picture of an overlap region that was previously discussed.

Returning to the ESE classes, it is expected that more isotropic events will have smaller differences between in- and out-of-plane pathlengths than more elliptical events. This was also studied in Trajectum, the results of which are presented in Fig. 3.10. In Fig. 3.10 (left), the pathlength distributions for q_2 -small events are shown. These same distributions are shown for q_2 -large events in Fig. 3.10 (right). The same general effect can be observed as in the inclusive case, where pathlength distributions are more similar in central events than they are in peripheral. What is new here, however, is that for each centrality class, the in-plane and out-of-plane distributions are more similar in q_2 -small events than in the q_2 -large events.

To make these observations more quantitative, one can consider the ratios of the average in- and out-of-plane pathlengths for the different ESE samples, as can be seen in Fig. 3.11 and Fig. 3.12. For the purely geometric case (Fig. 3.11), the in-plane/out-

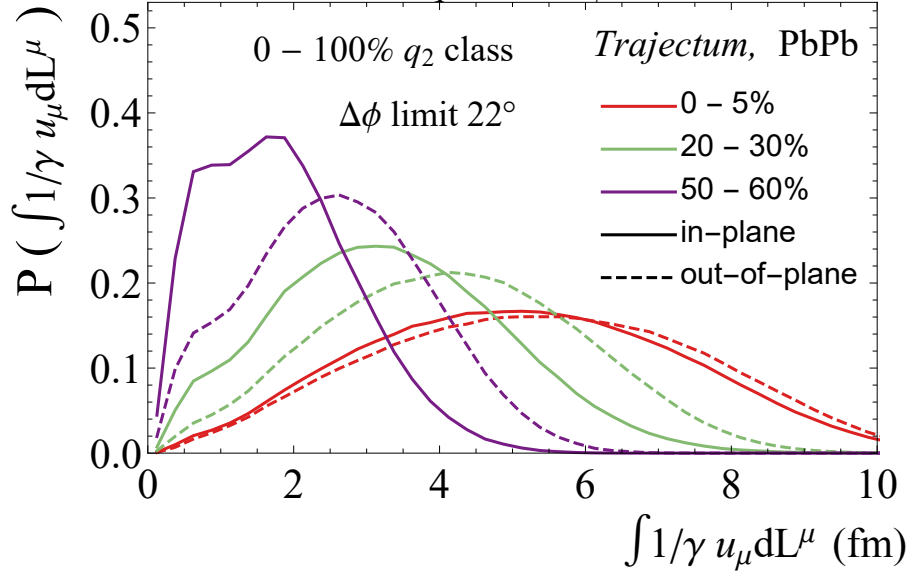


Figure 3.9: Pathlength distributions for in- and out-of-plane non-interacting probes. Distributions are presented for inclusive events. In this case, the pathlength definition includes the movement of the fluid cell. It can be seen that in-plane distributions are shorter than out-of-plane pathlengths, with a more pronounced difference in peripheral events. Figure taken from [95].

of-plane ratios are very similar for all centralities below about 50%. For peripheral collisions, a slight deviation begins to emerge, but the difference between the q_2 -small and q_2 -large curves is still not more than $\sim 5\%$ at 60% centrality (if $\Delta\varphi < \pm 22^\circ$). While this may or may not be significant enough of a difference to be experimentally measurable, the situation improves when one accounts for the movement of the fluid cell. In this case (Fig. 3.12 left), the difference between ratios for different ESE classes is significant at all centralities. Considering the semicentral region, the separation between the ratios for the q_2 -small and q_2 -large samples (again with $\Delta\varphi < \pm 22^\circ$) is about 14% at 30% centrality, and increases to 21% at 50% centrality.¹⁰ If one then includes a temperature weighting to account for hot spots in the plasma (Fig. 3.12 right), this separation is slightly reduced. However, it is still significant, ranging from $\sim 9\%$ to $\sim 14\%$ over the 30–50% centrality interval.

¹⁰Note that the 30–50% centrality region is of particular interest due to the ALICE experimental triggers that enable measurements on a higher statistics data-set in this region.

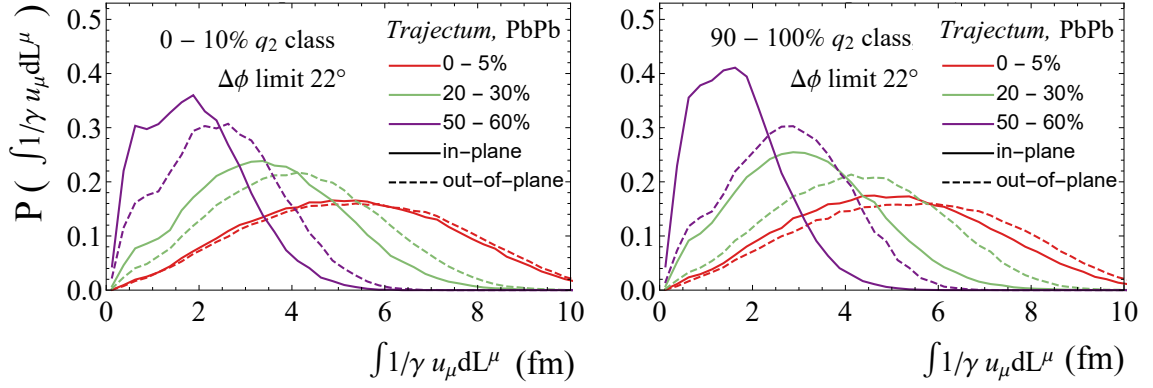


Figure 3.10: Pathlength distributions for in- and out-of-plane non-interacting probes in event-shape engineered samples. Distributions are presented for q_2 -small (left), and q_2 -large (right) event classes. Distributions are for the pathlength proxy in which the motion of the fluid cell is included. Figure taken from [95].

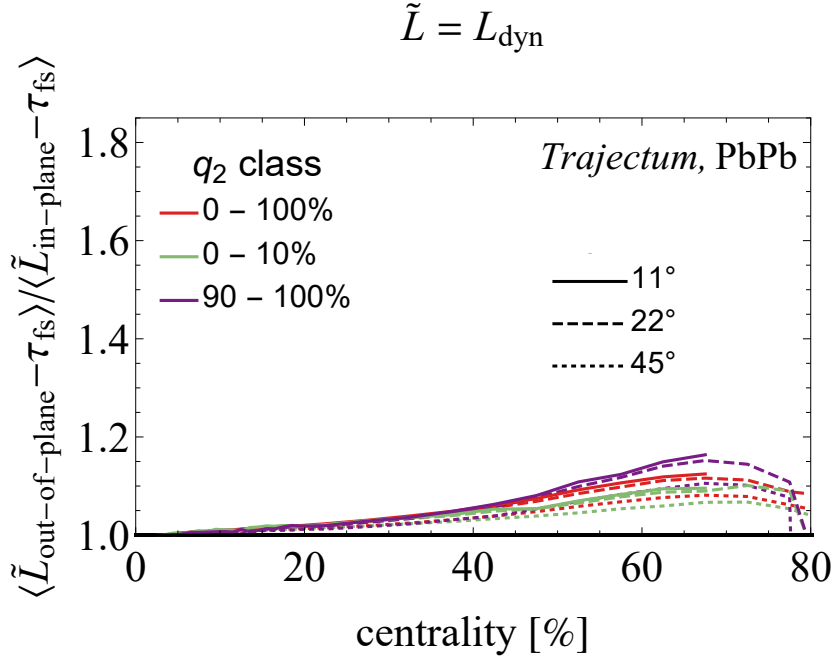


Figure 3.11: Ratios of average out-of-plane to in-plane pathlengths traversed by non-interacting probes for different q_2 classes. Here, pathlength is defined geometrically for an expanding medium. Figure taken from [95].

While the benefits of using ESE are clearly apparent from this study, there are a few details regarding how best to design the relevant observables that can be influenced by the calculations shown here. One such choice regards the selection of angles

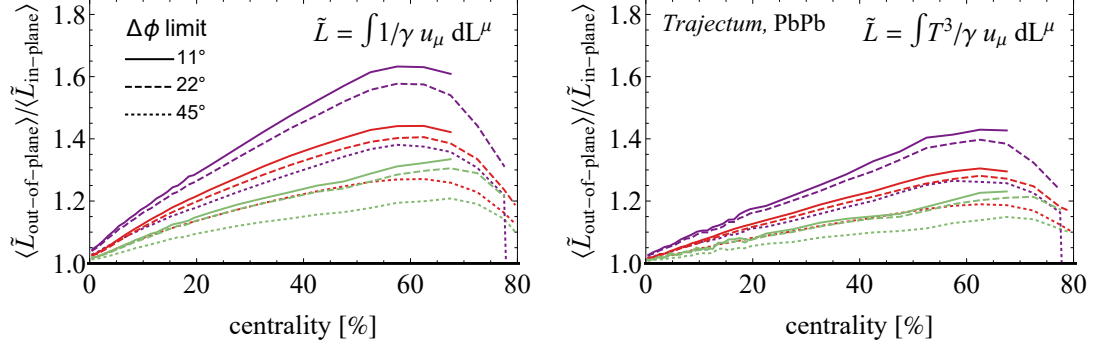


Figure 3.12: Ratios of average out-of-plane to in-plane pathlengths traversed by non-interacting probes for different q_2 classes. Left: The inner product of the probe and the fluid cell is considered when calculating the pathlength. Right: The inner product of the probe and the fluid cell, as well as a local temperature weighting, is considered when calculating the pathlength. Figure taken from [95].

to consider when assigning jets as in- or out-of-plane. Note that the dotted, dashed, and solid lines represent the restriction on $\Delta\varphi$. By this, we mean that any probes within the designated angle of Ψ_2 are considered in-plane, and probes within that angle of \vec{n} are considered out-of-plane. So for example, in the dotted case where the designation is 45° , all jets are classified as either in- or out-of-plane. This maximizes statistics, but minimizes potential signal, as can be seen in the figure. When $\Delta\varphi$ is then restricted to 22° , this improves the signal considerably. In Fig. 3.12 (left), for example, the q_2 –small and q_2 –large curves move from 12% apart to 17% apart at 40% centrality, simply by making this $\Delta\varphi$ cut. Note that, however, one receives diminishing returns when imposing further restrictions on $\Delta\varphi$. For example, after changing the designation to 11° , the resulting gain in signal is not considerable. The results of this study indicate that further angle restrictions past 22° , while significantly reducing the available statistics, do not optimize the potential signal.

“Let’s hope the heavy-ion guys didn’t mess up.”

— Unnamed Scientist, *Angels and Demons*

Chapter 4

The Measurement

There are several challenges to constraining the pathlength dependence of jet quenching that arise from the experimental reality of only having access to final-state particles. For example, it is impossible to identify the spatial origin of a jet within a heavy-ion collision, prohibiting the extraction of the pathlength that any given jet traverses. Further, even if one were able to measure this quantity directly, fluctuations in jet-medium interactions result in a probabilistic distribution of energy loss values that a parton could undergo. While these realities have thus far prevented an explicit determination of the pathlength dependence of jet energy loss, ongoing experimental work is continuously improving our knowledge of the subject.

This section will discuss previous experimental attempts to determine the pathlength dependence of energy loss, highlighting various techniques that have been developed to overcome the aforementioned difficulties. It will then cover the jet measurement that has been done for this thesis, discussing the consequences and implications of these results. Finally, ideas for additional measurements that may further clarify our collective understanding of pathlength-dependent energy loss will be considered.

4.1 Previous Results

As the pathlength dependence of jet-quenching is an important quantity that allows one to better understand the underlying jet-medium interactions, there have been many experimental efforts to constrain this value. A summary of those efforts is included here.

4.1.1 Dijet Asymmetry

One of the most traditional observables to study the pathlength dependence of jet quenching is the dijet asymmetry. This observable considers the momentum differences between back-to-back dijets, with the assumption that an imbalance will arise due to increased quenching of the jet that travels the longer distance through the plasma. The observable x_J , defined as:

$$x_J = \frac{p_T^{\text{subleading}}}{p_T^{\text{leading}}} \quad (4.1)$$

can be used for this purpose. Here, p_T^{leading} and $p_T^{\text{subleading}}$ refer to the transverse momenta of the highest- p_T and second highest- p_T jets in an event, respectively. Results measured by ATLAS show significant deviation between pp and Pb–Pb values, as shown in Fig. 4.1 (left) [97]. Alternatively, one can consider the observable A_J , defined as:

$$A_J = \frac{p_T^{\text{leading}} - p_T^{\text{subleading}}}{p_T^{\text{leading}} + p_T^{\text{subleading}}} \quad (4.2)$$

as was done by CMS [99], shown in Fig. 4.1 (right). While differences between pp and Pb–Pb results are suggestive of medium influence, they can be reproduced by considering only fluctuations in jet-medium interactions [98]. Therefore, this observable is not sufficient for constraining an explicit pathlength dependence.

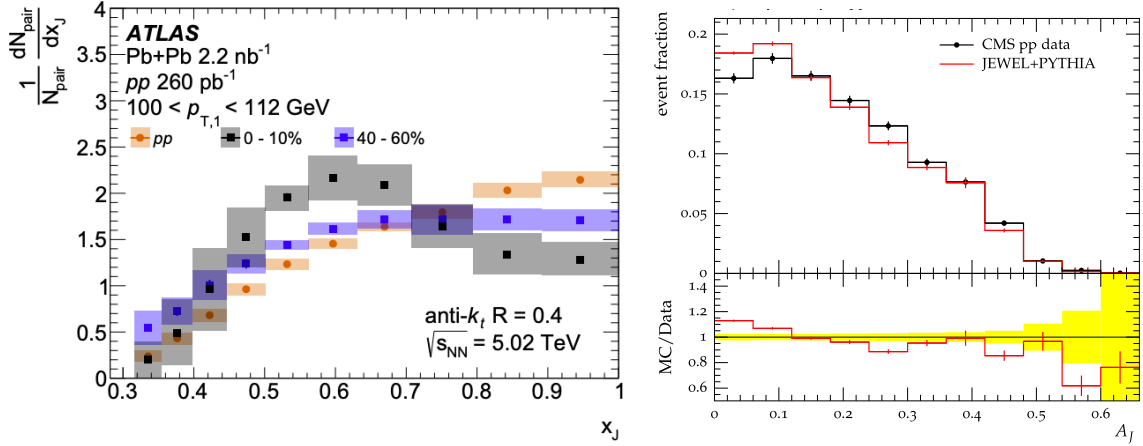


Figure 4.1: Left: The dijet asymmetry x_J , as measured by ATLAS. While significant differences in asymmetry are seen between pp and Pb–Pb collisions, these differences can be explained by fluctuations in jet-medium interactions. Figure taken from [97]. Right: The dijet asymmetry as measured by CMS, compared to JEWEL. Figure taken from [98].

4.1.2 Azimuthal Anisotropy

Another traditional approach to this question is to consider the azimuthal anisotropy of jet production using an observable known as the jet- v_2 . In ALICE, this measurement uses the event-plane technique to compare in- and out-of-plane jet yields, with:

$$v_2 = \frac{1}{R_2} \frac{\pi}{4} \frac{N_{\text{in}} - N_{\text{out}}}{N_{\text{in}} + N_{\text{out}}} \quad (4.3)$$

where N_{in} (N_{out}) are the yields of in-plane (out-of-plane) jets, and R_2 is the event-plane resolution.¹² Because the in-plane axis is shorter than the out-of-plane axis, it is expected that out-of-plane jets will undergo more energy loss and therefore be more suppressed if pathlength dependence is a significant contributor to their behavior. Such would result in a positive jet v_2 , as has been measured by ALICE [100] and ATLAS [101] at 2.76 TeV in central and semi-central collisions.

In addition to the traditional jet- v_2 study, one can consider the azimuthal anisotropy of jet constituents. This novel observable, termed the jet-particle v_2 , has recently

¹Note that this equation is only valid for in-plane and out-of-plane definitions at $\pm 45^\circ$ from the second order event-plane.

²The calculation of R_2 is discussed in more detail in **Section 4.2.2: Event-Plane Angles**.

been measured at ALICE using 5.02 TeV data [102]. This analysis shows that jet constituents have a v_2 of a similar magnitude to that of fully reconstructed jets. Interestingly, a finite jet-particle v_2 is also observed in p-Pb collisions, obscuring the interpretation of the results obtained in Pb-Pb. A summary of the various high- p_T v_2 measurements performed by ALICE is shown in Fig. 4.2.

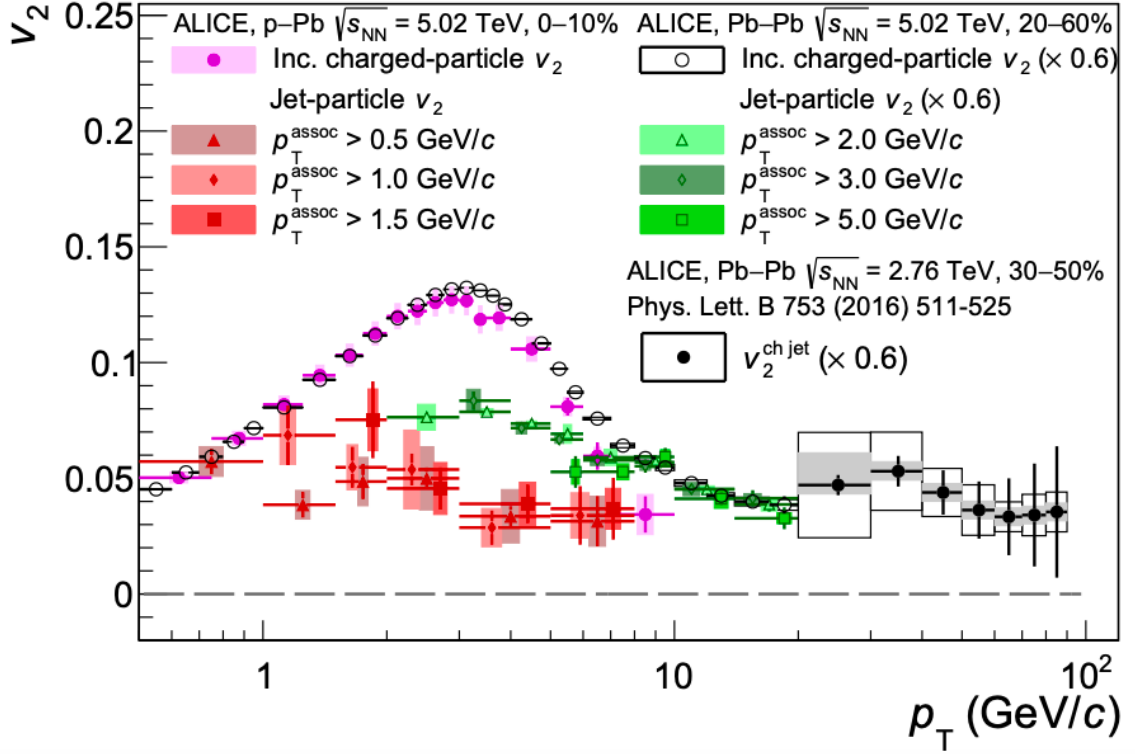


Figure 4.2: A summary of high- p_T v_2 measurements in p-Pb and Pb-Pb collisions using ALICE data. Figure taken from [102].

4.1.3 Event-Shape Engineering

While Event-Shape Engineering (ESE) has never been used before in data to study jet quenching, it has been used for various soft sector [103] and heavy-flavor [104, 105] measurements up to a p_T of 24 GeV/c. These heavy-flavor measurements are particularly interesting for contextualizing jet studies, as heavy-flavor partons are influenced by both the underlying flow of an event and quenching effects. In Fig. 4.3 (left) are shown the event-shape engineered yield ratios for prompt D-mesons. It can

be seen that these ratios are generally compatible with unity, with possible hints of a deviation for semicentral events. The D-meson v_2 can also be studied using ESE, as shown in Fig. 4.3 (right). These results demonstrate a correlation between the flow of the underlying event and that of the D-mesons, and provide interesting context for the jet measurement described later in this chapter.

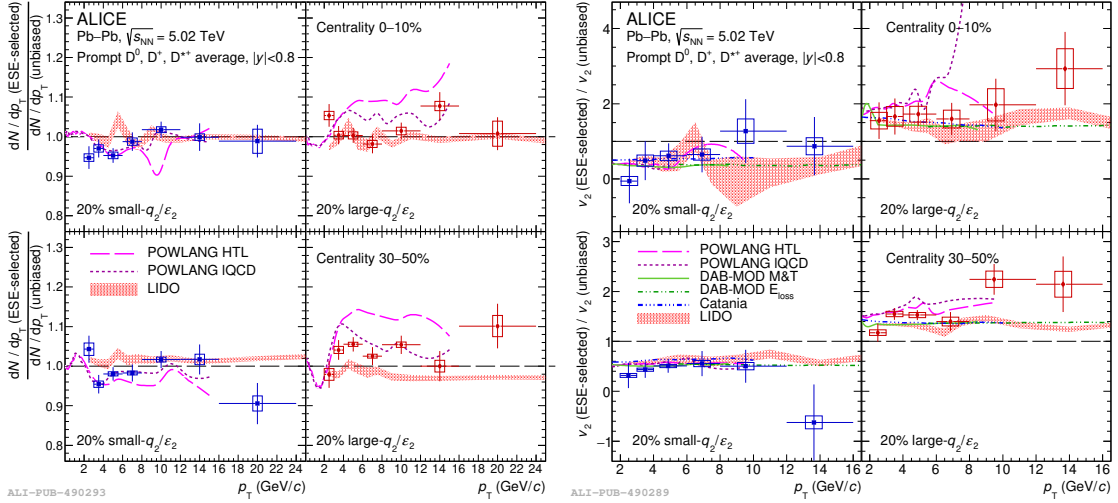


Figure 4.3: Left: Ratio of per-event D-meson yields for ESE-selected to unbiased event classes. Agreement with both LIDO [106] and POWLANG IQCD models within uncertainties makes difficult the extraction of the interplay between flow and quenching effects. Right: Ratio of D-meson v_2 values for large and small ESE classes as compared to the inclusive sample. Ratios agree well with most models. Figure originally appearing in [105].

4.2 Methodology

4.2.1 Jets

In rare instances, quarks and gluons will undergo large exchanges of transverse momentum early in a collision, resulting in high virtuality partons that scatter outward and fragment into sprays of hadrons known as jets. Due to the high Q^2 associated with this phenomenon, jet behavior is directly calculable, making jets excellent probes of pQCD. There are several difficulties, however, to performing precise experimental measurements that can be compared directly with theoretical predictions. These

challenges are further complicated in a heavy-ion environment, where the large and fluctuating background must be carefully considered. This section will address these difficulties, and their solutions, in the context of this analysis.

Reconstruction

While jets originate from high energy partons, hadrons (and leptons (and photons)) are what appear in a detector. To collect all the particles that originate from the chosen parton, a reconstruction algorithm must be applied. Several types of reconstruction algorithms are available, each possessing their own advantages. One necessary quality of a modern jet-finder is that it be infrared and collinear (IRC) safe. This means that soft and collinear radiations of the initiating parton should not impact the final jet definition. The field standard IRC-safe jet-finder is the anti- k_T algorithm [108], which clusters particles by first considering all tracks in the detector as “preclusters” (these are sometimes also referred to as “pseudo-jets”). The preclusters are then iteratively compared with each other. If these preclusters appear correlated according to criteria defined by the algorithm, they are merged. For anti- k_T jets, this merging condition is determined using a “distance” quantity d_{ij} , defined as:

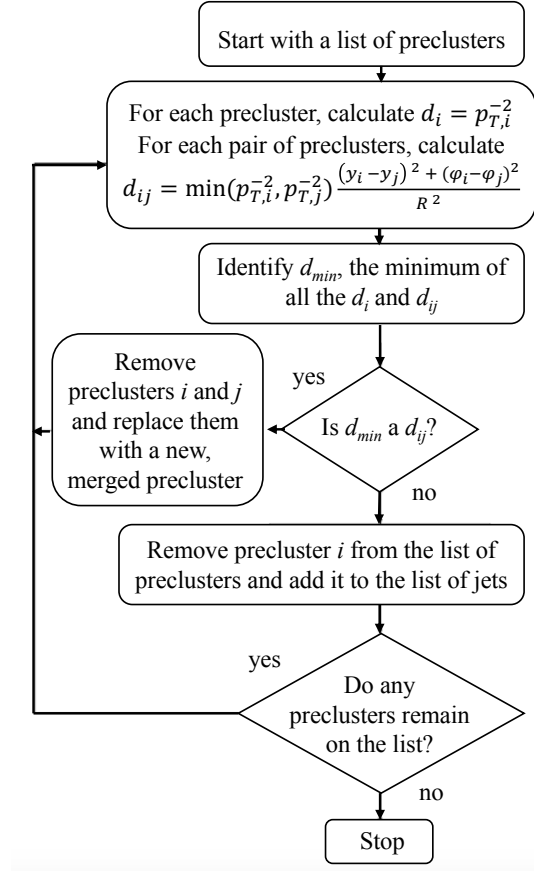


Figure 4.4: A flow diagram of the anti- k_T jet-finding algorithm. Figure taken from [107].

$$d_{ij} = \min(p_{T,i}^{-2}, p_{T,j}^{-2}) \frac{(y_i - y_j)^2 + (\varphi_i - \varphi_j)^2}{R^2} \quad (4.4)$$

where i and j are indices of the pseudo-jets. Additionally, every pseudo-jet is assigned a “self-distance” d_i , defined as:

$$d_i = p_{T,i}^{-2} \quad (4.5)$$

If d_{ij} is a minimum amongst all the distances and self-distances in the event, the preclusters i and j are deemed correlated and merged with each other. If, instead, d_i is a minimum, the precluster i is removed from the list. This process is repeated until all pseudo-jets are merged or rejected, as outlined in Fig 4.4. The anti- k_T algorithm is IRC safe, and typically defines jets in relatively conical shapes.

In addition to the different types of reconstruction algorithms available, jets are defined by several parameters. These include the recombination scheme, the resolution parameter (R), and the leading track bias. The recombination scheme refers to the prescription for merging pseudo-jets during the clustering process. Two popular recombination schemes are E -scheme and p_T -scheme. E -scheme refers to a procedure where the 4-vectors of the pseudo-jets are summed normally. For p_T -scheme, the p_T of the preclusters are summed after rescaling the energy if applicable. All else being equal, E -scheme is typically preferred given that one retains full kinematic information during merging. In ALICE, however, we lack a hadronic calorimeter, thus requiring one to make assumptions about the masses of the constituents in order to use E -scheme. For this analysis, we therefore use p_T -scheme recombination. A detailed description of the recombination schemes can be found in [109].

The next parameter to consider is the resolution parameter R . It is defined as:

$$R = \sqrt{(\Delta\varphi)^2 + (\Delta\eta)^2} \quad (4.6)$$

and is roughly equal to the radius of the jet. Note that R defines the region of phase space in which a jet-finder searches for correlated preclusters, and is not an intrinsic property of the jet. For this reason, it is theoretically advantageous to measure

large- R jets, given that these are more likely to capture the full radiation pattern of the parent parton. Experimentally, however, large- R jets collect more uncorrelated soft background during reconstruction than their small- R counterparts, making them more difficult to correct. The choice of R then often depends on various aspects and sensitivities of the observable one seeks to measure, and requires the analyzer to strike a balance between extracting maximum physics and being pragmatic. For this analysis, we measure both $R = 0.2$ and $R = 0.4$ jets.

The next input for the definition of a jet-finder is the leading track bias. A leading track bias refers to a p_T requirement imposed on the leading hadron, where jets without a sufficiently high- p_T track are discarded. Application of a leading track bias increases the probability that the jet is associated with a hard scattering, and is thus advantageous for reducing contamination from combinatorial jets (objects that are reconstructed by a jet finder, but do not originate from a hard scattering). This analysis considers jets with a leading track bias of $5 \text{ GeV}/c < p_T < 100 \text{ GeV}/c$.

Signal and Noise

In small collision systems (pp and p-Pb) with clean backgrounds, jet-finders are capable of providing reasonable jet definitions that serve as good proxies for the initiating parton. In heavy-ion collisions, this picture becomes more complicated due to the large and fluctuating nature of the underlying event. During the clustering process, jet-finders are susceptible to excluding signal particles while including background particles. Additionally, the jet and medium are not decoupled systems, and the presence of a jet provokes a medium response. This provides a further conceptual difficulty in defining which particles truly belong to the jet, and which are more appropriately classified as background.

In practice, these difficulties are managed with a straightforward background subtraction procedure. In ALICE, the standard method for performing this subtraction is to use what is known as the pedestal method [110], where the background-corrected jet p_T is defined as:

$$p_T^{\text{jet}} = p_T^{\text{jet,rec}} - \rho \cdot A^{\text{jet,rec}} \quad (4.7)$$

where ρ represents the average momentum density per unit area, and A is the jet area. In this analysis, we determine ρ using a k_T jet-finder³ with $R = 0.4$ to cluster all particles in the event into jets. The two highest p_T jets are then excluded, and an average momentum density is calculated from the remainder of the k_T jets. The jet area A is measured by applying a uniform density of massless “ghost” particles throughout the event and considering the proportion that are clustered into the jet. This quantity is required to be greater than $0.6\pi R^2$. The jet area cut serves the purpose of reducing contamination from combinatorial jets, which tend to have more irregular shapes than signal jets.

Embedding and the Response

While the background subtraction described above is an important first step for correcting the jet transverse momentum, it does not account for, say, whether or not a jet was in- or out-of-plane. Furthermore, it does not remove combinatorial jets with perfect efficiency or purity, or account for smearing due to inefficiencies in the detector. To address these issues, an unfolding procedure is applied.

Unfolding is the process by which we create a mapping from a reconstructed spectrum back to what that spectrum looked like before it passed through a detector. As we are only able to measure reconstruction-level quantities, however, we must approach this problem backwards. First consider:

$$p_T^{\text{rec}} = \mathbf{R} p_T^{\text{truth}} \quad (4.8)$$

where p_T^{rec} is the reconstructed spectrum, p_T^{truth} is the truth-level spectrum, and \mathbf{R} is the response matrix. We can generate p_T^{truth} with Monte Carlo simulations and we can measure p_T^{rec} experimentally. The question then becomes, how do we produce \mathbf{R} ?

³The k_T algorithm follows the same set of steps as the anti- k_T algorithm described in **Section 4.2.1: Reconstruction**. These algorithms differ only in the definition of d_{ij} (see Equation 4.4), where p_T^{-2} is replaced with p_T^2 for k_T jets. This produces jets with more irregular shapes.

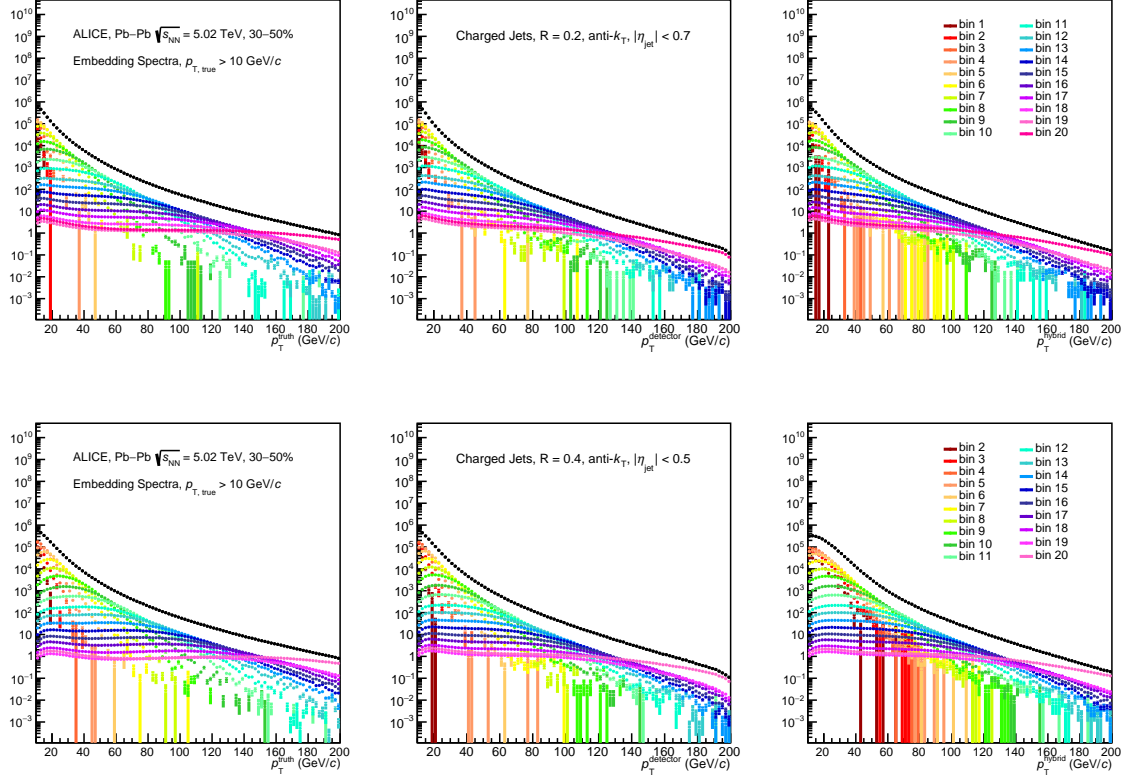


Figure 4.5: Truth-level (left), detector-level (middle), and hybrid-level (right) jet spectra for $R = 0.2$ (top) and $R = 0.4$ (bottom). Different colors correspond to different p_T^{hard} -bins.

Experimentally, \mathbf{R} can be generated using what’s known as an embedding procedure. This is done by first generating PYTHIA8 [76] jets and processing them using GEANT3 [111]. The GEANT jets are then inserted into a Pb–Pb background. We use the term “truth-level” to refer to the PYTHIA spectrum because it is the most foundational level of Monte Carlo and is directly comparable to theory. We use “detector-level” to refer to the spectrum after it has been processed by GEANT, because this stage reproduces how our detectors measure the PYTHIA jets. Finally, we use “hybrid-level” to refer to the spectra that have been embedded in Pb–Pb data, because this level accounts for effects from both the detector and the combinatorial background. The spectra processed at these three levels can be seen in Fig. 4.5 for $R = 0.2$ and $R = 0.4$ jets.

There are a few technical details of the embedding that one must keep in mind

to ensure the generation of a sufficiently high-quality sample. First, consider that PYTHIA jet yields are produced in a realistic manner, such that the jet cross-section is steeply falling with p_T . This poses the difficulty that high- p_T jets are not generated at significant rates, thus limiting the precision with which we can simulate the high- p_T regime. To circumvent this, we use “ p_T^{hard} bins” to artificially increase our statistics. These bins refer to constraints imposed on the highest Q^2 process in a PYTHIA event, such that the simulation is forced to include a parton scattering of the desired scale.⁴ For this analysis, we use 20 p_T^{hard} bins spanning the p_T range that can be measured in ALICE. After being generated, the jets from these p_T^{hard} bins must be down-scaled. This leaves us with a smooth and realistic spectrum with high statistics throughout the entire p_T range.

While the usage of p_T^{hard} -bins allows for sufficient statistics at high- p_T , it also introduces an excess of statistics at low- p_T . This in principle would not be an issue, except that our analysis is limited by the merging capabilities of the CERN grid and the computational space available on local computers to do the final processing. To handle this problem, we use what are known as extractor bins. Extractor bins down-sample jets at hybrid-level by randomly rejecting a predetermined fraction of jets based on their p_T . The spectrum is then scaled to account for the down-sampling introduced by these bins. The extractor bins used in this analysis are listed in Table 4.1.

In addition to the proper scaling for the p_T^{hard} and extractor bins, some additional cuts must be applied. One beneficial requirement is to apply a cutoff of $p_T^{\text{true}} > 10$ GeV/ c . This helps ensure the smoothness of the spectra by preventing low- p_T truth-level jets that sit on top of high- p_T data jets from being upweighted and introducing spikes at hybrid-level. Additionally, the $p_T^{\text{hard}} = 1$ bin has been removed from the $R = 0.4$ spectra. This improves the stability of the closure by removing outliers in the same way as the $p_T^{\text{true}} > 10$ GeV/ c cut described above. Here, it is worth remembering that these cuts are analysis specific. Ultimately, the analyzer should seek to balance the need for closure of the unfolding with the desire to use the least restrictive cuts on the Monte Carlo.

⁴These constraints are equivalent to the ptHat class that is sometimes used in PYTHIA.

$p_{T,\text{hybrid}}^{\min}$ (GeV/ c)	$p_{T,\text{hybrid}}^{\max}$ (GeV/ c)	Extraction Percentage
10	20	1%
20	30	4%
30	40	15%
40	60	25%
60	80	35%
80	100	35%
100	140	15%
140	200	5%

Table 4.1: Details of the extractor bins used in this analysis.

After the embedding has been performed and its quality has been verified, the hybrid-level jets are matched back to their truth-level counterparts, thus populating the entries of \mathbf{R} . To perform this matching, the hybrid- and truth-level jets are required to be within $R_{\text{matching}} = 0.75 \cdot R_{\text{jet}}$, where R is the resolution parameter. They are also required to have a shared p_T fraction of 0.5. These requirements help minimize the entry of combinatorial jets into the matching. Sample response matrices for this analysis are shown in Fig. 4.6. Note that we fill the response for both jet- p_T and $\Delta\varphi$, where $\Delta\varphi$ is the relative angle between the jet and the event-plane. This choice will be explained in more detail in **Section 4.2.1: Unfolding**.

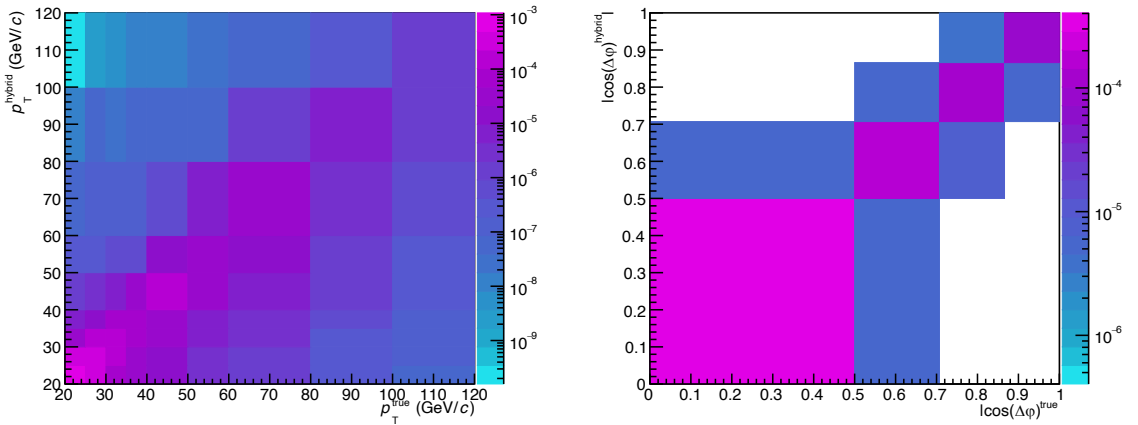


Figure 4.6: Projections of the response matrix for $R = 0.2$ jets. Left: Correlations between truth-level and hybrid-level jet p_T . Right: Correlations between truth-level and hybrid-level $\Delta\varphi$.

Performance

Now that we have constructed our response, we are almost ready to unfold. Before we can proceed, however, we must consider several metrics to assess the quality of the embedding and how difficult the unfolding problem will be. These metrics are collectively referred to as the jet performance. We can begin the process of evaluating the jet performance by first considering the 2-dimensional distributions known as the residuals. The residuals are defined as:

$$\mathcal{R}(x = p_{T,\text{true}}, y = \frac{p_{T,\text{rec}} - p_{T,\text{true}}}{p_{T,\text{true}}}) = \frac{d^2N}{dx dy} \quad (4.9)$$

Residuals for the spectra used in this analysis can be seen in Fig. 4.7. Note that we separate the contributions to \mathcal{R} by the three spectra levels described in **Section 4.2.1: Embedding and the Response**. This is done so that the source of any abnormalities can be more easily identified.

To make practical use of the residuals, we can consider various projections of \mathcal{R} and the corresponding statistical information associated with these plots. The first such metric is the Jet Energy Scale (JES), which is defined as:

$$\text{JES} = \left\langle \frac{p_{T,\text{rec}} - p_{T,\text{true}}}{p_{T,\text{true}}} \right\rangle \quad (4.10)$$

This is equivalent to the mean of \mathcal{R} as a function of $p_{T,\text{true}}$. The JES can be used to determine if there is any systematic over- or under-subtraction of the background, with a JES of 0 indicating that the background subtraction is, on average, correct. Plots of the JES can be seen for various ESE classes in Fig 4.8, separated by the different spectra levels. Here, “Detector” refers to the contribution from detector effects (PYTHIA \leftrightarrow GEANT), “Fluctuations” the contribution from background (GEANT \leftrightarrow hybrid), and “Overall” the combined effect (PYTHIA \leftrightarrow hybrid). Note that for $R = 0.4$ jets, the contribution due to fluctuations is worse than it is for $R = 0.2$. This is because $R = 0.4$ jets are more susceptible to the inclusion of soft background particles. This observation will prove important for determining the lower limits of

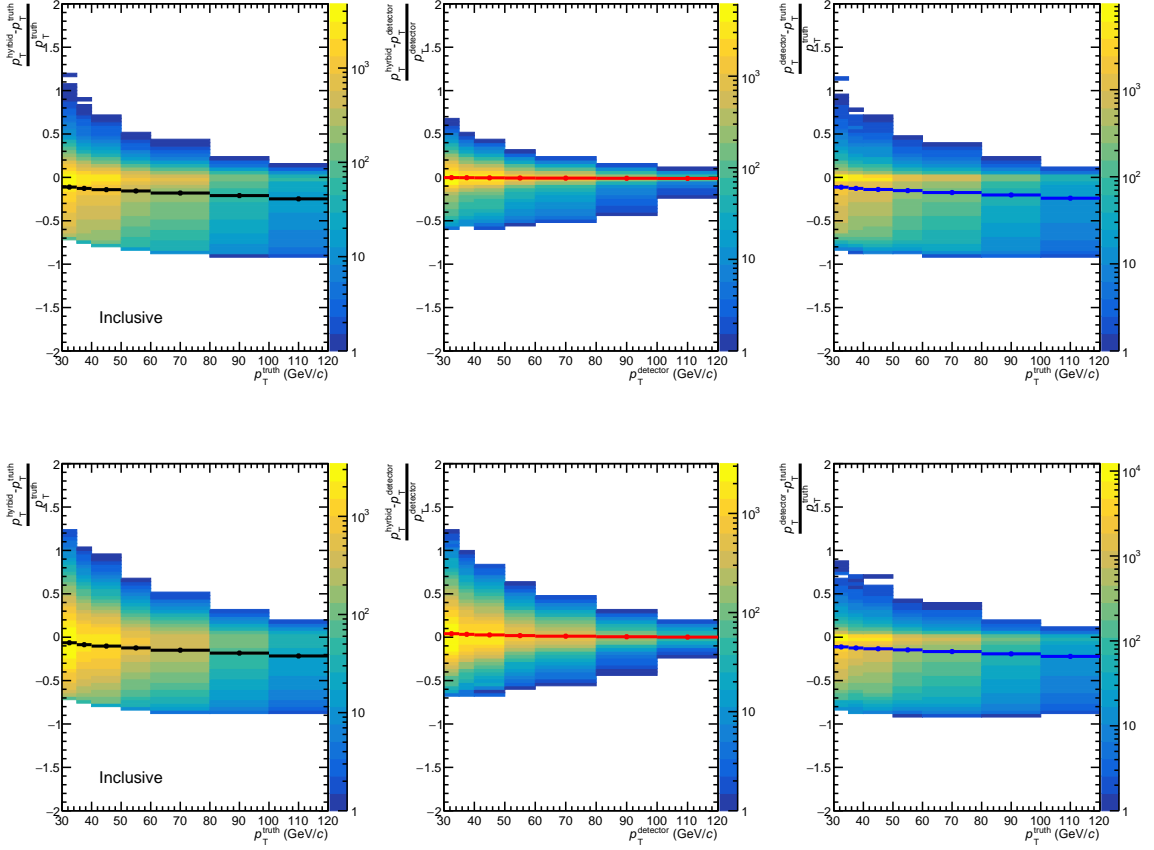


Figure 4.7: Residual plots for $R = 0.2$ (top) and $R = 0.4$ (bottom). These residuals are for jets from an inclusive sample of 30-50% Pb-Pb events.

the unfolding for the different samples of jets.

The next performance metric is the Jet Energy Resolution (JER), which can be thought of as the width of the residual distribution as a function of $p_{T,\text{true}}$. It is defined as:

$$\text{JER} = \sigma\left(\frac{p_{T,\text{rec}} - p_{T,\text{true}}}{p_{T,\text{true}}}\right) \quad (4.11)$$

JER distributions for this analysis can be seen in Fig. 4.9. Note that at low- p_T , JER values are considerably worse for $R = 0.4$, again driven by the fluctuations. This is, as in the case of the JES, due to the fact that $R = 0.4$ jets cluster more combinatorial background.

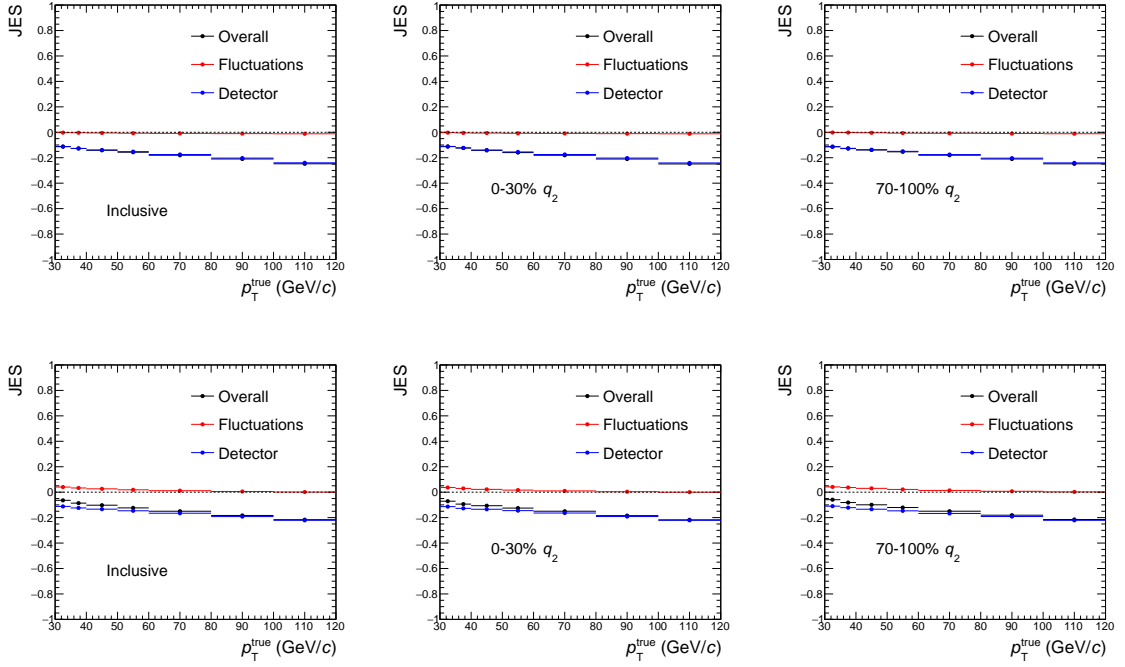


Figure 4.8: Top: JES plots for $R = 0.2$. Bottom: JES plots for $R = 0.4$. Here, Fluctuations (red) refer to contributions from the background, Detector (blue) to contributions from detector imprecisions, and Overall (black) to the combined effect.

Finally, our last jet performance metric is the δp_T :

$$\delta p_T = \frac{dN}{d(p_{T,\text{rec}} - p_{T,\text{true}})} \quad (4.12)$$

which can be seen in Fig. 4.10. Note that here we do not consider the distributions separately for the different spectra levels, but instead are seeking to evaluate the overall accuracy of the reconstructed spectra. The δp_T is an important quantity because the width of this distribution can help to determine the lower bound of the measured range to be used in the unfolding, where we choose a value of:

$$5 \cdot \sigma(\delta p_T) \quad (4.13)$$

Values lower than this are likely to produce significant non-closures. A full set of performance plots for this analysis can be found in **Appendix B**.

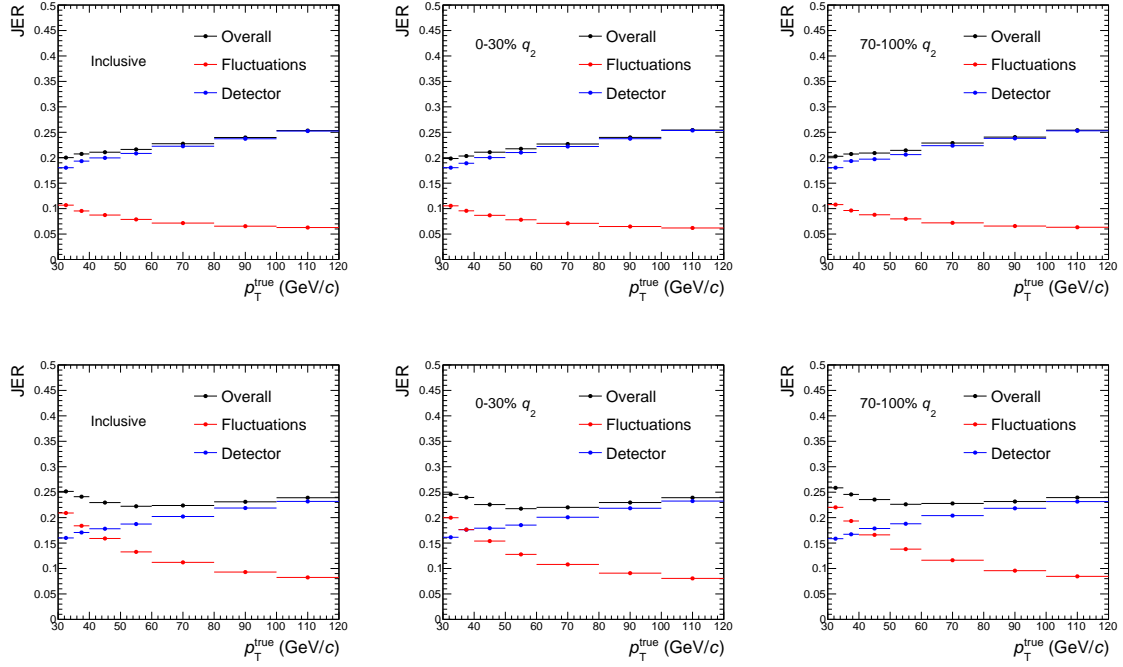


Figure 4.9: JER plots for $R = 0.2$ (top) and $R = 0.4$ (bottom) charged anti- k_T jets with a leading track bias of $p_T^{\text{lead}} > 5 \text{ GeV}/c$. These performance plots are for jets from inclusive (left), q_2 –small (middle), and q_2 –large (right) events recorded for 30–50% Pb–Pb collisions.

Unfolding

To obtain the true spectrum from the reconstructed spectrum, we must now invert the response matrix using an unfolding procedure, where Equation 4.8 is rearranged to give:

$$p_T^{\text{truth}} = \mathbf{R}^{-1} p_T^{\text{rec}} \quad (4.14)$$

This inversion is most straightforward in the case of a diagonal matrix. Such a luxury is not, however, always (ever) afforded when studying heavy-ion collisions. We must therefore employ numerical methods to approximate \mathbf{R}^{-1} , a process known as unfolding.

Bayesian unfolding is one such method [112]. It uses Bayes’s theorem to estimate the truth-level spectrum, which can be done by approximating \mathbf{R}^{-1} in the following

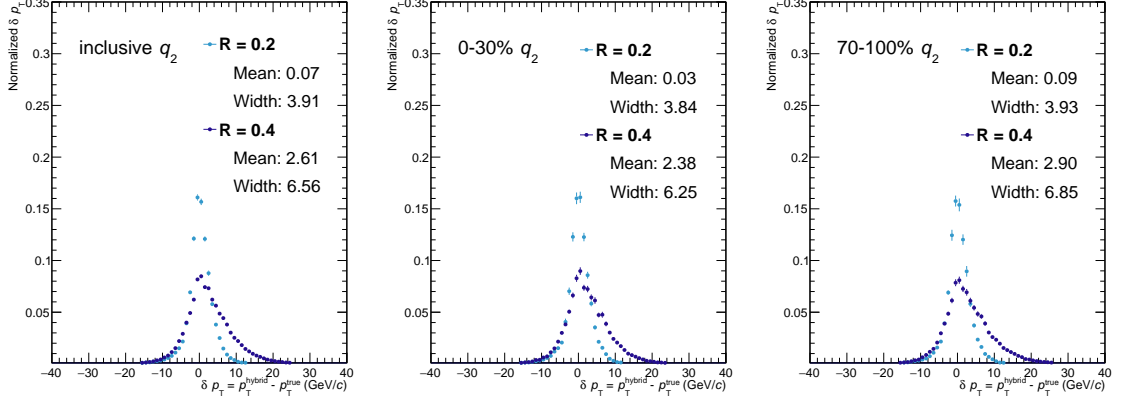


Figure 4.10: Plots of δp_T for inclusive (left), q_2 -small (middle), and q_2 -large (right) classes. Note that the δp_T distributions are wider and more offset from 0 for $R = 0.4$ jets than for $R = 0.2$ jets.

way:

$$P(A|B) = \frac{P(B|A)P(A)}{P(B)} \quad \Rightarrow \quad \mathbf{R}^{-1} = \frac{\mathbf{R}_{ji} \cdot P(C_i)}{\sum_{k=1}^n \mathbf{R}_{jk} \cdot P(C_k)} \quad (4.15)$$

where $P(C)$ is (ideally) the truth-level distribution. At this point, however, we only have access to the measured spectrum and to the response, so we substitute $P(C)$ with our “prior”. In this context, a prior refers to the first guess at p_T^{truth} .⁵ For the purposes of this analysis, we choose the PYTHIA-level Monte-Carlo spectrum to be used as our prior. While this provides a first calculation of \mathbf{R}^{-1} , we would ultimately like to extract the truth-level distribution corresponding to our measured distribution. We can thus plug Equation 4.15 into Equation 4.14 and attempt to solve iteratively:

$$P(C_i)^n = \sum_i \frac{\mathbf{R}_{ji} \cdot P(C_i)^{n-1}}{\sum_k \mathbf{R}_{jk} P(C_k)^{n-1}} \times p_T^{\text{rec}} \quad (4.16)$$

where n represents the iteration (here n is an index, not a power). After a sufficient number of iterations, the result should remain stable when further incrementing. At this point, we claim to have unfolded the spectrum and take the chosen iteration as our nominal result:

⁵While the unfolding should be relatively insensitive to the details of the prior, the robustness of this procedure must be tested. For this analysis, variations of the prior are considered as a systematic uncertainty.

$$P(C_i)^n = p_T^{\text{truth}} \quad (4.17)$$

Note that here, we use the p_T spectrum as our sample observable, but we are free to use any observable when unfolding. Further, it is possible to unfold multiple observables simultaneously up to an arbitrarily high number of dimensions. Currently, the maximum number of dimensions that have been unfolded using the Bayesian technique is 3, but new techniques such as OmniFold [113] are pushing this boundary.

For this analysis, we choose a 2D Bayesian procedure where the axes of unfolding are the jet- p_T and $|\cos(\Delta\varphi)|$, where $\Delta\varphi$ is the relative angle between the jet and the event plane ψ_2 in the $r - \varphi$ plane. To understand the choice of performing a 2D unfolding, consider that our background subtraction procedure is independent of the event-plane angle. Therefore, in-plane jets will, on average, experience an undersubtraction of the underlying event. Conversely, out-of-plane jets will be subject to oversubtraction. A 2D response allows us to account for these phenomena. Additionally, as jets undergo bin migration in p_T , they may also undergo a corresponding bin migration in $\Delta\varphi$. Using 2D unfolding allows for the correction of any such simultaneous migration.

After performing the unfolding using RooUnfold [114], the number of iterations was chosen to be 6. The validity of this result was then assessed by evaluating several stability and closure checks. For the stability checks, we considered how much the final result changed by changing the number of iterations. For the closure tests, we checked how internally consistent the result was. For the simulated samples, this entailed looking at how well the unfolded spectra agreed with their Monte-Carlo level values. For our measured data, this involved refolding the unfolded spectra and seeing how well the refolded results agreed with the raw data. These checks will be described here in more detail.

The first check we performed is the so-called trivial test. This test uses the full embedded sample to build a response and a complementary pseudo-data spectrum. This pseudo-data spectrum is then unfolded using said response. Because the pseudo-

data is composed of the same jets used in the response, it is expected that the closure should be near-perfect. Any non-closures in the trivial test indicate a serious issue with the measurement, such as a significant off-diagonal band that “confuses” RooUnfold. A sample trivial check for this analysis can be seen in Fig 4.11. For the full set of trivial tests, see **Appendix B**.

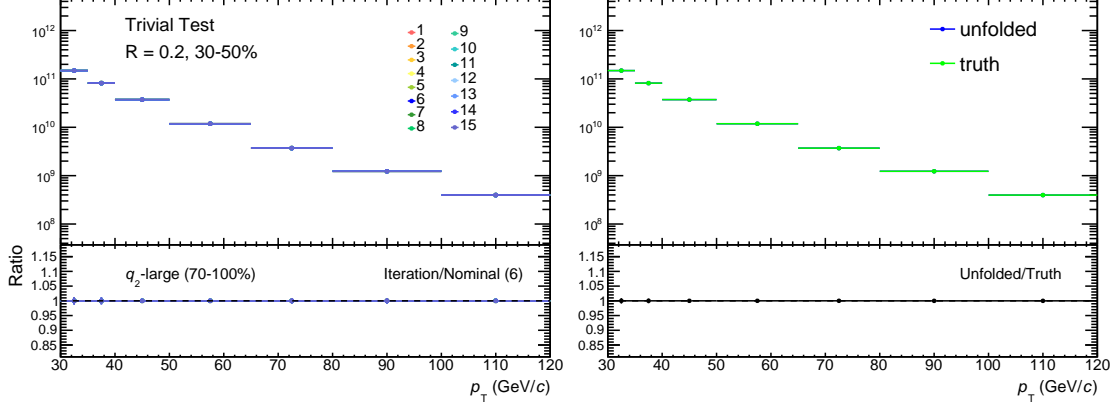


Figure 4.11: Trivial test for $R = 0.2$ jets from q_2 -large events. Left: Unfolded results up to 15 iterations. Bottom panel shows the ratio of each iteration to the chosen iteration (6). Right: Comparison of unfolded and truth-level spectra. Bottom panel shows the ratio of these results, demonstrating the necessary closure.

The next check is the Monte Carlo split test, which is used to assess the statistical stability of the procedure. Here the embedding spectra are randomly divided into two samples, where 70% of the matched jets are used to construct the response, and 30% are used to create the pseudo-data spectrum (compare this with the trivial test, where 100% of the matched jets are used to construct the response, and the same 100% are used to generate the pseudo-data). This pseudo-data is then unfolded, the results of which are compared to the truth-level values of said spectrum. Non-closures that arise during the split test likely point to outliers in the response due to insufficient statistics. A sample split test for this analysis can be seen in Fig. 4.12. A complete set of split tests studied in this analysis can be found in **Appendix B**.

Finally, we can assess the closure of the data using a refolding test. For our data sample, we do not know what the corresponding truth-level spectrum looks like, so we cannot compare our output to a Monte Carlo. Instead, we unfold the data and refold

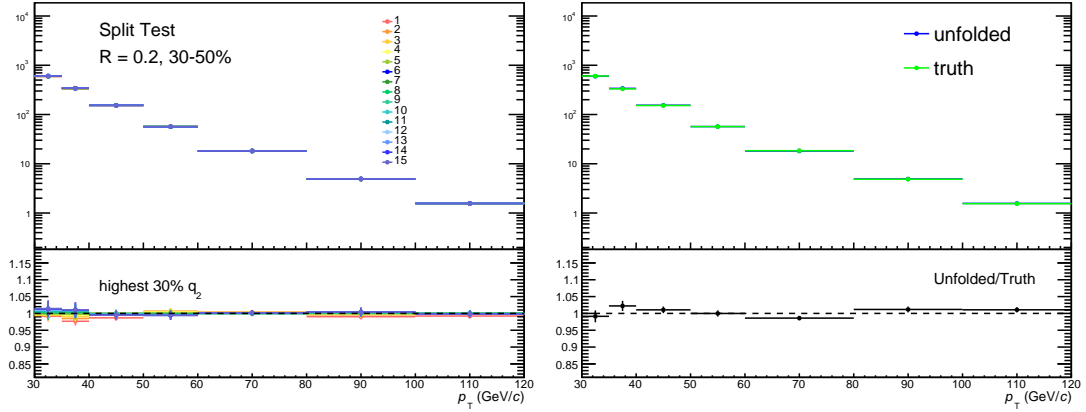


Figure 4.12: Monte Carlo split test for $R = 0.2$ jets from q_2 -large events. Left: Unfolded results up to 15 iterations. Right: Closure test for the 6th iteration.

the spectrum by reapplying the response matrix. The resulting spectrum has thus been “refolded”, and should agree well with the raw spectrum. A sample refolding test can be seen in Fig. 4.13. Full refolding results can be found in **Appendix B**.⁶

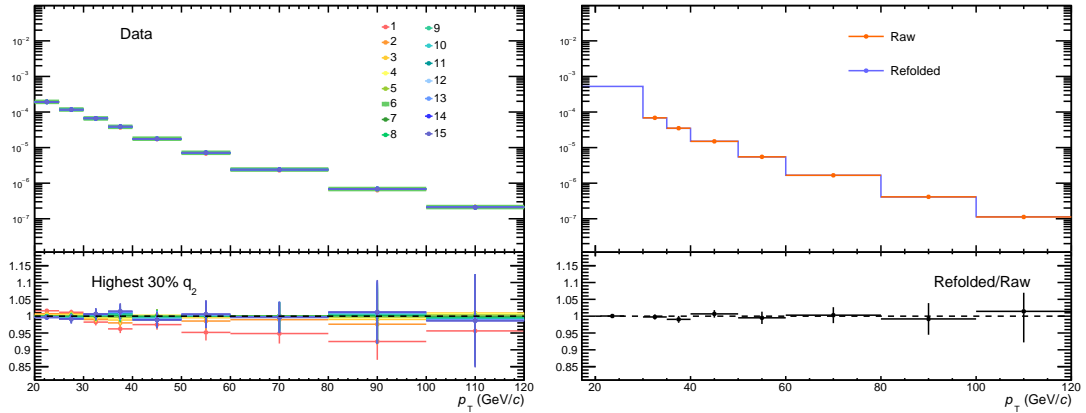


Figure 4.13: Refolding test for $R = 0.2$ jets from q_2 -large events. Left: Unfolded results up to 15 iterations. Right: Refolding test for the 6th iteration.

⁶A nice analogy for refolding is the use of an online translation service. Consider receiving a text in a language you do not speak (for example, Welsh), and translating it to English online. The English seems reasonable, but this alone is not enough to confirm that the translation is good. By then using the translation service to convert the English text back to Welsh, you can compare the original and final Welsh transcripts. This is perhaps not sufficient to verify the translation, but it does give the user confidence that the system is internally consistent.

Corrections

After unfolding, there are two efficiency corrections that must be applied to the jet spectra. The first of these is to account for the reconstruction efficiency, which is defined as:

$$\epsilon = \frac{N_{\text{matched}}}{N_{\text{truth}}} \quad (4.18)$$

where N_{truth} is the number of PYTHIA jets embedded into a pp event and N_{matched} is the number of those jets that are eventually reconstructed and matched back to a truth-level counterpart. This correction accounts for the jets that are lost due to detector effects. The values of the reconstruction efficiencies used in this analysis can be seen in Fig. 4.14.

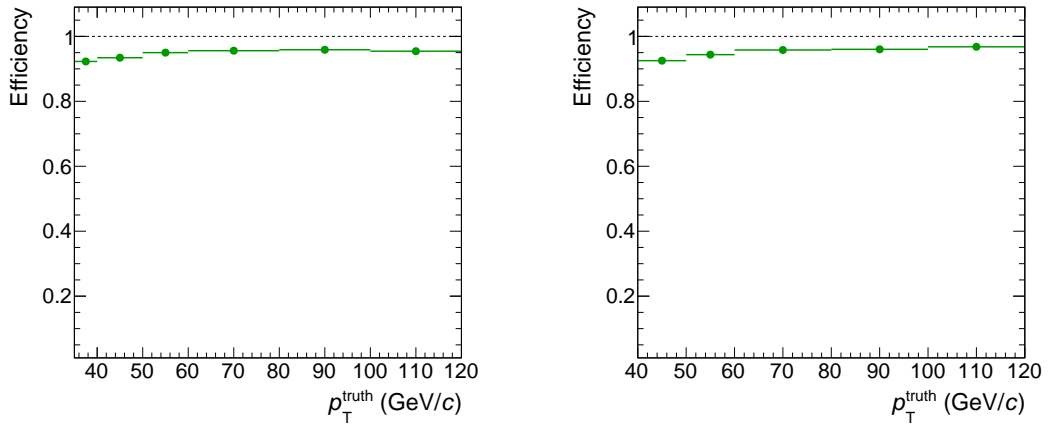


Figure 4.14: Reconstruction efficiency plots for $R = 0.2$ (left) and $R = 0.4$ (right).

The next correction is known as the kinematic efficiency. This correction accounts for jets that are measured outside of the unfolded range, but whose true p_T is within those bounds, as these jets are subsequently “lost” during unfolding. For example, a jet that is 35 GeV/ c at truth-level but 25 GeV/ c at hybrid-level would not be included in the final spectrum if the lower bound of the measured range were 30 GeV/ c . To correct for this, we calculate p_T -dependent kinematic efficiencies for each event-plane angle class when filling the response matrix. We then scale the final spectra by these values. An efficiency of at least 75% is required for reporting the final value. The

kinematic efficiencies used are shown in Fig. 4.15.

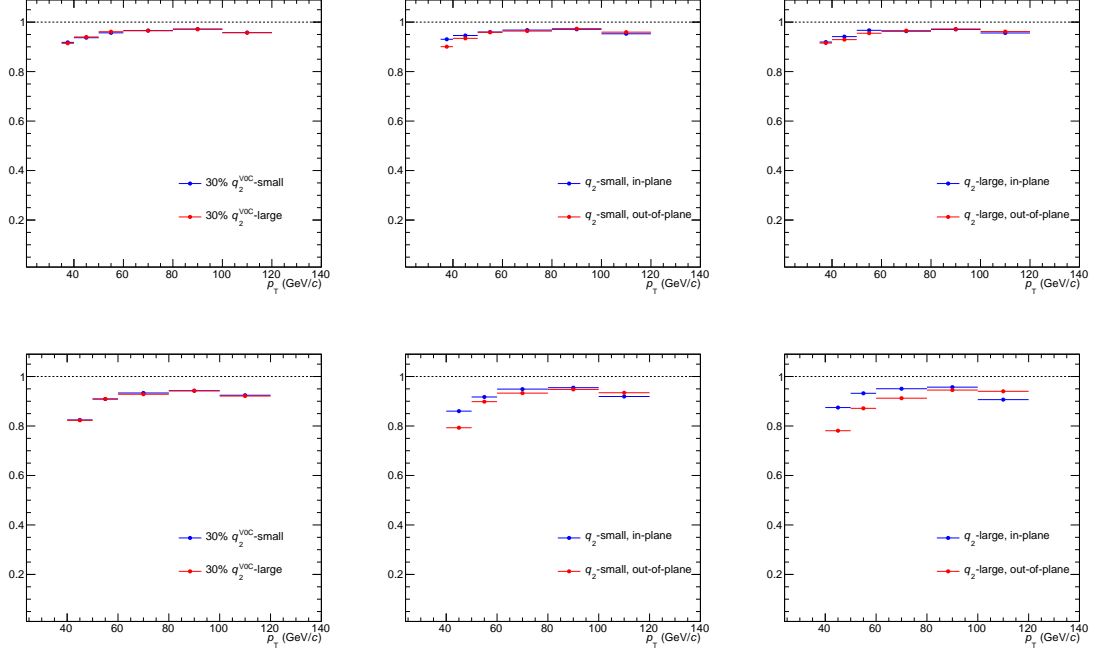


Figure 4.15: Kinematic efficiency plots for $R = 0.2$ (top) and $R = 0.4$ (bottom). Efficiency values are calculated in 2 dimensions (p_T and $\Delta\varphi$; here they are projected onto the p_T axis for in-plane and out-of-plane jets. Note that in-plane efficiencies are generally equivalent to or higher than out-of-plane efficiencies. This can be attributed to the pedestal subtraction, which has a tendency to over-subtract in the out-of-plane direction.)

4.2.2 Flow

Event Ellipticity

A strength of using ESE is that it allows us to study the correlations between phenomena at different scales. For this analysis, we are interested in understanding the relationship between event-shape and jet behavior. To study an event's shape, then, we look to quantify its ellipticity. Experimentally, this is done by measuring the q_2 , defined as:

$$q_2 = |\mathbf{Q}_2|/\sqrt{M}, \quad (4.19)$$

where M is the charged-particle multiplicity and \mathbf{Q}_2 is the second order flow vector. \mathbf{Q}_2 is defined as:

$$\mathbf{Q}_2 = \left(\sum_{i=1}^M w_i \cos(2\varphi_i), \sum_{i=1}^M w_i \sin(2\varphi_i) \right). \quad (4.20)$$

where the sums are performed over all charged tracks in the chosen detector. Here, w_i correspond to the signal weights, calibrated for the specific detector system.⁷ Small values of q_2 correspond to rounder events, whereas large values of q_2 correspond to more almond-shaped events. In this analysis, q_2 was measured using charged hits in the V0C. This detector was chosen because it is sufficiently far forward ($-3.7 < \eta < -1.7$) to minimize auto-correlations with jets in the TPC, but still lower in rapidity than the V0A. This enables a wider distribution of q_2 values and better discrimination of the event-shape than could be achieved by using the V0A. Note that the correlation between q_2 values in the V0C and V0A is not particularly strong, as shown in Fig. 4.16. Ideally, information from both forward and backward rapidities would be used to determine the event shape. Due to the limited number of ALICE sub-detectors and the requirement of using independent sub-detectors for each calculation to avoid auto-correlations, this is not currently preferred.

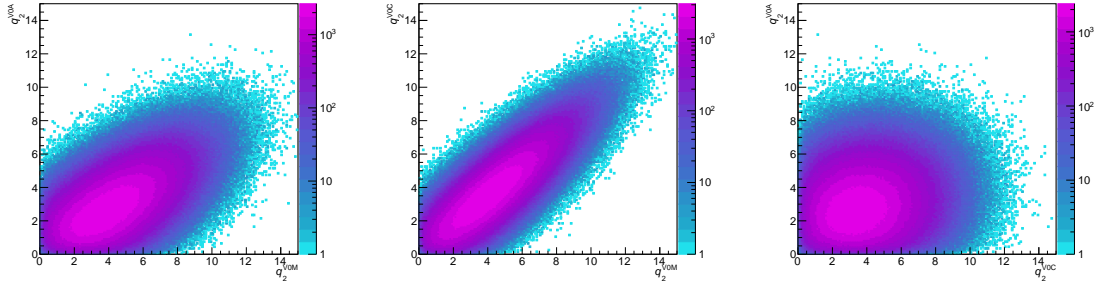
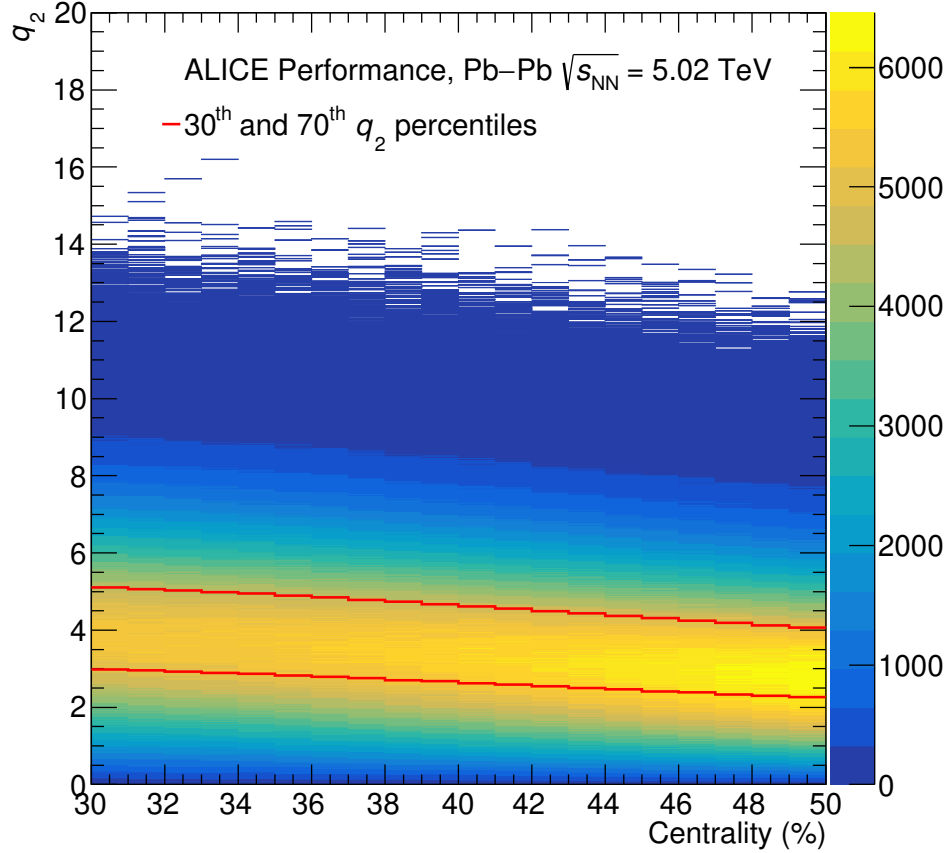


Figure 4.16: Left: Correlations between q_2^{V0A} and q_2^{V0M} . Middle: Correlations between q_2^{V0C} and q_2^{V0M} . Right: Correlations between q_2^{V0A} and q_2^{V0C} .

The measured q_2 distribution is shown in Fig. 4.17 as a function of collision centrality. Events with the 30% smallest and 30% largest q_2 values (henceforth referred to as q_2 -small and q_2 -large) are demarcated by the red lines. Note that these per-

⁷The q_2 calibrations used in this analysis were generously provided to the author by the CF working group.

centiles are determined in bins of 1% centrality, which was done to avoid introducing a trivial bias. From this plot, it can be seen that events have a wide distribution of anisotropies, even within a centrality class, as is predicted by Glauber modeling.⁸



ALI-PERF-537725

Figure 4.17: Measured q_2^{VOC} distribution as a function of collision centrality. Red lines demarcate the 30th and 70th percentiles, which were measured in 1%-wide bins of centrality. A significant distribution of anisotropies can be seen for all reported centrality values.

Event-Plane Angles

In addition to knowing the event ellipticity, we are interested in knowing the event-plane angle for any given collision. The second-order event-plane angle ψ_2 has been measured using the V0A detector and is given by the direction of Q_2 . The V0A was

⁸See **Section 3.2.1: Initial State** for more details regarding Glauber models.

chosen for this measurement due to it's being opposite in rapidity from the V0C, thus minimizing the impact of auto-correlations. Event-plane distributions as measured by the various ALICE subdetectors can be seen in Fig. 4.18.

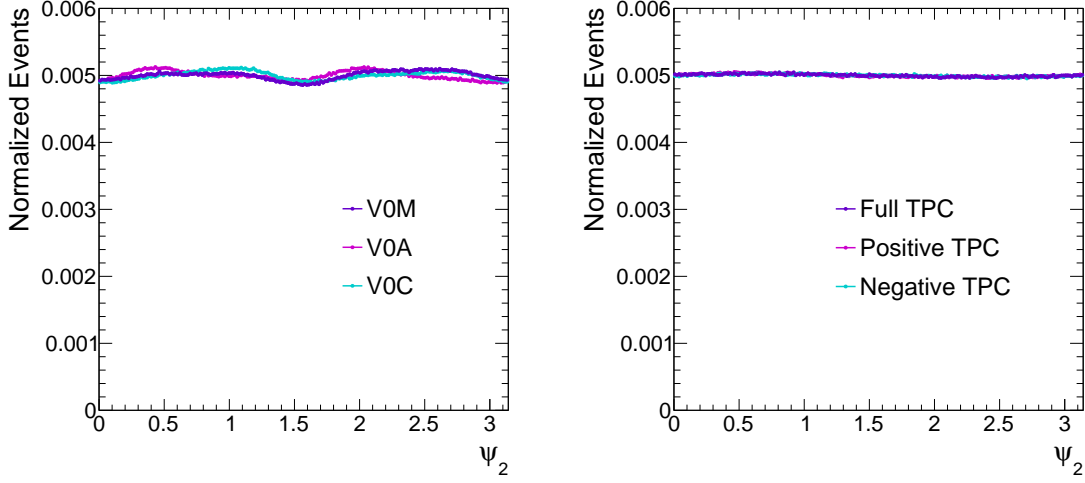


Figure 4.18: Top: Event-plane angle distributions for the V0 detectors (left) and TPC segments (right). Note that, after applying calibrations, the V0 distributions exhibit a non-flatness of 4%. This is consistent with that observed in other published ALICE analyses, e.g. [105].

Knowing the event-plane angles of our events allows us to establish the relative angle of the jets in our sample, from which we can calculate the v_2 . This technique is known as the “event-plane method”, and is what was used for the previous ALICE measurement described in Section 4.1.2 [100]. For this analysis, we define in-plane as being within $\pm 30^\circ$ of Ψ_2 , and out-of-plane as being within $\pm 30^\circ$ of \vec{n} (the vector perpendicular to Ψ_2). Using these definitions, the relationship between the v_2 and the in- and out-of-plane yields can be derived from the Fourier expansion of the azimuthal distribution of the event:

$$\frac{dN}{d(\Delta\varphi_n)} \propto 1 + \sum_{n=1}^{\infty} 2v_n^{\text{jet}} \cos[n(\Delta\varphi_n)] \quad (4.21)$$

From this expression, one can define in- and out-of-plane yields as:

$$N_{\text{in}} = \int_{-\pi/6}^{\pi/6} \frac{dN}{d(\Delta\varphi)} d(\Delta\varphi) + \int_{5\pi/6}^{7\pi/6} \frac{dN}{d(\Delta\varphi)} d(\Delta\varphi) \quad (4.22)$$

$$N_{\text{out}} = \int_{\pi/3}^{2\pi/3} \frac{dN}{d(\Delta\varphi)} d(\Delta\varphi) + \int_{4\pi/3}^{5\pi/3} \frac{dN}{d(\Delta\varphi)} d(\Delta\varphi) \quad (4.23)$$

where the limits of the integrals are assigned based on the angles we restrict on for our in- and out-of-plane choices.⁹ Evaluating these integrals and considering the ratio, we find:

$$\frac{N_{\text{in}}}{N_{\text{out}}} = \frac{\frac{2\pi}{3} + 2\sqrt{3}v_2^{\text{obs}}}{\frac{2\pi}{3} - 2\sqrt{3}v_2^{\text{obs}}} \quad (4.24)$$

This gives us an explicit relationship between the relative in- and out-of-plane yields and the v_2 . We can thus invert this equation to get an explicit expression for the v_2 :

$$v_2^{\text{observed}} = \frac{\pi}{3\sqrt{3}} \frac{N_{\text{in}} - N_{\text{out}}}{N_{\text{in}} + N_{\text{out}}} \quad (4.25)$$

Note, however, that this expression is only for v_2^{observed} as we have not yet accounted for the event-plane resolution. Here, we refer to a phenomenon where imprecisions in the detector used for event-plane determination result in an under-measurement of the v_2 . A sketch of this concept can be seen in Fig. 4.19 (left). To intuitively understand this, consider a completely imprecise detector that produces effectively random angles. In this case, v_2^{observed} would be 0, even though the true v_2 might be some finite value. We account for this smearing, then, by incorporating a value known as R_2 , where:

$$v_2^{\text{true}} = \frac{1}{R_2} v_2^{\text{observed}} = \frac{\pi}{3\sqrt{3}} \frac{1}{R_2} \frac{N_{\text{in}} - N_{\text{out}}}{N_{\text{in}} + N_{\text{out}}} \quad (4.26)$$

R_2 is effectively a measurement of how imprecise the detector is, and can be

⁹The choice to define in-plane jets as being within $\pm 30^\circ$ of ψ_2 and out-of-plane as being $\pm 30^\circ$ of the perpendicular axis was done to maximize signal while minimizing loss of statistics. See **Section 3.3: Trajectum** for more details.

calculated using a technique known as the “three sub-event method” [115], where:

$$R_2^A = \sqrt{\frac{\langle \cos(2(\psi_2^A - \psi_2^C)) \rangle \langle \cos(2(\psi_2^A - \psi_2^B)) \rangle}{\langle \cos(2(\psi_2^B - \psi_2^C)) \rangle}} \quad (4.27)$$

Here, A , B , and C represent 3 independent sub-detectors that have been chosen to measure the event-plane angle. Note that the values of R_2 degrade for highly spherical events, as the concept of an event-plane angle becomes more ambiguous. Values of R_2 for various detector combinations are shown in Fig. 4.19 (right) as a function of q_2 . For the detector combination used in this analysis (V0C for q_2 and V0A for event-plane angles), $R_2 = 0.68$ for q_2 -large samples and 0.55 for q_2 -small samples.

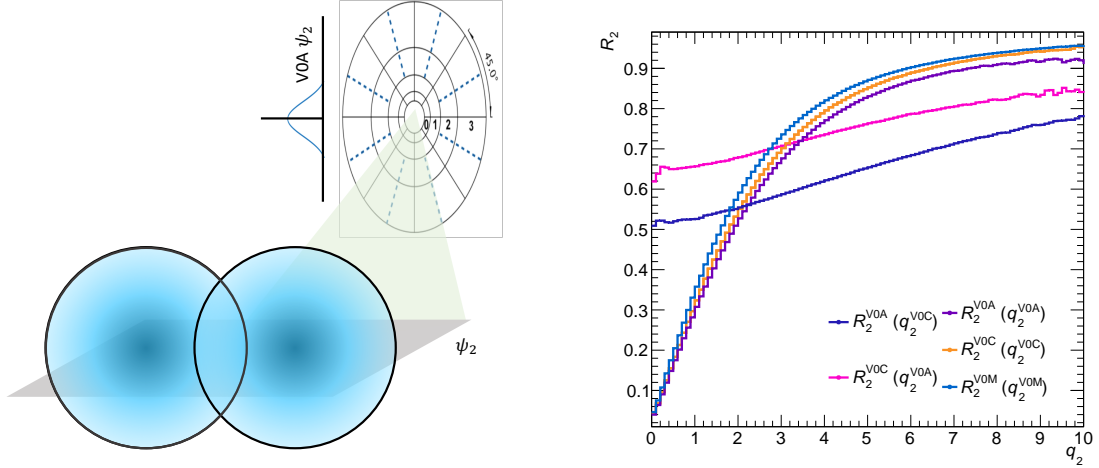


Figure 4.19: Left: Sketch of the ψ_2 smearing that occurs in a detector. Right: R_2 distributions as a function of q_2 . Different colors represent different detector choices for both q_2 and R_2 .

We now have a way to correct the v_2 . This analysis is not, however, reporting the v_2 , but rather is reporting a yield comparison. To correct the yields, we must take an additional step. The procedure is as follows. First, we measure the uncorrected $N_{\text{out}}/N_{\text{in}}$ ratio $\mathcal{R}^{\text{measured}}$. We then calculate the v_2 from this ratio, corrected for the event-plane resolution as described above. Finally, we perform the inverse to recover $\mathcal{R}^{\text{corrected}}$, here assuming $R_2 = 1$. This gives the yield ratios we would expect to measure in the case of a perfect detector, and produces a correction ranging from

5-25%. The impact of the resolution correction on the final ratios can be seen for $R = 0.2$ jets in Fig. 4.20.

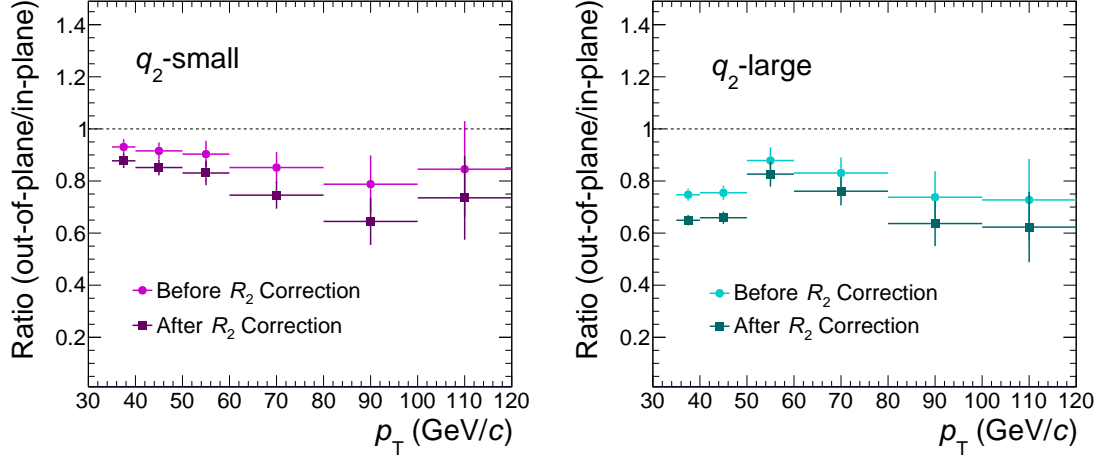


Figure 4.20: Impact of the R_2 correction for $R = 0.2$ jets from q_2 -small (left) and q_2 -large (right) events. Uncorrected points are lighter in color, with corrected points being darker. Note that this correction is not p_T dependent, but instead depends on the value of the uncorrected point, always pulling the out-of-plane/in-plane ratio away from unity.

From the corrected ratio $\mathcal{R}^{\text{corrected}}$, we can also obtain the corrected spectra. We do this by applying the constraint:

$$N_{\text{in}}^{\text{measured}} + N_{\text{out}}^{\text{measured}} = N_{\text{in}}^{\text{corrected}} + N_{\text{out}}^{\text{corrected}} \quad (4.28)$$

This constraint gives us a system of two equations and two unknowns. We can thus solve for these unknowns and fix the yield points as:

$$N_{\text{in}}^{\text{corrected}} = \frac{S}{\mathcal{R}^{\text{corrected}} + 1} \quad (4.29)$$

$$N_{\text{out}}^{\text{corrected}} = \frac{S}{1 + (1/\mathcal{R}^{\text{corrected}})} \quad (4.30)$$

where $S = N_{\text{in}}^{\text{measured}} + N_{\text{out}}^{\text{measured}}$. The final difference between the corrected and uncorrected spectra is very small relative to the amount of code required to implement

it (on average, 6% for $R = 0.2$ and 7% for $R = 0.4$, with a maximum difference of 16% for two points), but this is why we have grad students.

4.2.3 Uncertainties

This analysis is impacted by both statistical and systematic uncertainties. The statistical uncertainties are determined by RooUnfold using a covariance matrix.¹⁰ The systematic uncertainties are determined separately by repeating the analysis while varying relevant parameters. There are five major sources of systematic uncertainty in this measurement. The first general class relates to the unfolding, and consists of those arising from the number of iterations chosen for the unfolding procedure, the truncation of the lower limit of the measured range that enters into the unfolding, and the weighting of the prior. Next, there is the uncertainty arising from the tracking inefficiency. Finally, there is that associated with the event-plane resolution.

When one unfolds a spectrum, there are several choices one must make. Many of these choices could, in principle, produce fully-closing spectra, so we study the changes to the final results that arise from varying these parameters in a reasonable way. The first such choice is the number of iterations used for the Bayesian procedure. We vary this number by ± 1 and compare the result to the nominal number of iterations. The second choice arises from where we truncate the lower bound of the reconstructed jets that enter into the unfolding. This value is also a best-guess based on the jet performance parameters and closure constraints, so we vary this value by ± 5 GeV/ c . Finally, we consider how we weight the prior estimate that we use. For our nominal unfolding, our prior estimate is simply the truth-level spectrum from the embedding. However, there is the possibility that this might bias the final output. For this final unfolding systematic, we reweight our prior by the ratio of the Monte Carlo to the data and scale the response accordingly.

The next major source of uncertainty is derived from our tracking precision. The tracking efficiency in Pb–Pb is nominally assumed to be 2% worse than that in pp collisions based on HIJING+GEANT studies [116]. Experimentally, this 2% loss of

¹⁰This corresponds to using the `errorTreatment = RooUnfold::kCovariance` option.

	R = 0.2				R = 0.4			
	q_2 -small in-plane	q_2 -small out-of-plane	q_2 -large in-plane	q_2 -large out-of-plane	q_2 -small in-plane	q_2 -small out-of-plane	q_2 -large in-plane	q_2 -large out-of-plane
Tracking efficiency	6-15	6-12	8-10	6-16	4-15	6-15	6-20	< 1-17
Unfolding iterations	< 1	< 1-1	< 1-1	< 1-1	< 1-2	< 1-4	1-3	< 1-3
Unfolding prior	< 1-3	< 1-2	< 1-2	< 1-2	2-6	< 1-5	< 1-8	2-5
Unfolding truncation	< 1	< 1	< 1	< 1	< 1-10	< 1-7	1-13	< 1-9
Event-plane determination	< 1	< 1	< 1	< 1	< 1	< 1	< 1	< 1
Total	6-15	6-12	8-10	6-16	8-16	6-16	12-21	9-17

Table 4.2: Summary of systematic uncertainties for differential spectra (reported in percentages). Reported ranges reflect the minimum and maximum uncertainty values across the p_T spectrum. For these differentiated yields, the uncertainties are generally dominated by the tracking efficiency.

efficiency is applied to the PYTHIA tracks that are used for embedding. To assess the uncertainty that this assumption introduces, we redo the embedding after lowering the tracking efficiency by an additional 4%. The data is then unfolded with this new response and compared to the original spectrum.

The last source of uncertainty considered in this analysis is that pertaining to our calculation of the event-plane resolution. To quantify this, we vary the resolution by 2% and repeat the analysis, as was done in the procedure for the Chiral Magnetic Effect analysis [117]. In this study, it was determined that using the χ^2 method (as opposed to the three-subevent method) to calculate R_2 produces a variation of less than 2%, thus motivating the variation done here. A summary of systematic uncertainty values for the ESE-sorted spectra is shown in Table 4.2.

The above methods describe how the uncertainties were calculated for the various spectra. For the ratios considered in this analysis, however, several of these uncertainties can be reduced by considering the correlations present. To treat these correlations, we instead use the ratios as our degrees of freedom. This is to say that the nominal ratio is first computed and then the systematic variations are applied to this curve (as opposed to computing the nominal spectra and propagating the uncertainties in the normal way). The differences between these ratios are then used to compute the systematic uncertainty. In general, the uncertainties in this analysis are highly correlated, so considering ratios allows us to greatly improve our sensitivity to signal. Systematic uncertainties for the ratios are summarized in Table 4.3. For a

	R = 0.2			R = 0.4		
	small (out/in)	large (out/in)	large/small	small (out/in)	large (out/in)	large/small
Tracking efficiency	<1-2	<1-5	1-3	4-9	1-9	1-3
Unfolding iterations	<1-1	<1-1	<1	<1-6	2-6	<1
Unfolding prior	<1-2	<1-3	<1-3	1-5	<1-12	<1-3
Unfolding truncation	<1	<1	<1	1-18	1-21	<1-3
Event-plane determination	<1	<1	N/A	<1-1	<1-1	N/A
Total	2-3	1-5	1-4	5-21	4-25	1-5

Table 4.3: Summary of systematic uncertainties for ratios (reported as percentages). Reported ranges reflect the minimum and maximum uncertainty values across the p_T spectrum.

complete set of uncertainties, see **Appendix C**.

4.3 Results

The charged-jet spectra sorted by ESE class and event-plane angle are presented in Fig. 4.21 for $R = 0.2$ (left) and $R = 0.4$ (right) anti- k_T jets with a leading track bias of 5 GeV/ c . These measurements were performed in 30–50% Pb–Pb collisions at $\sqrt{s_{NN}} = 5.02$ TeV. For $R = 0.2$, results are reported from $35 < p_T < 120$ GeV/ c , whereas for $R = 0.4$ they are reported from $40 < p_T < 120$ GeV/ c . Note that the $R = 0.4$ result is more restricted in p_T due to details of the kinematic efficiency and the stability of the unfolding, as described in **Section: 4.2.1**. These spectra are all steeply falling, as expected. An initial separation between the in-plane (blue + purple) and out-of-plane (orange + pink) yields can already be observed, as is consistent with expectations from the jet- v_2 . However, the systematic uncertainties preclude any further conclusions from being drawn about the differences between the spectra based on the event-shape class.

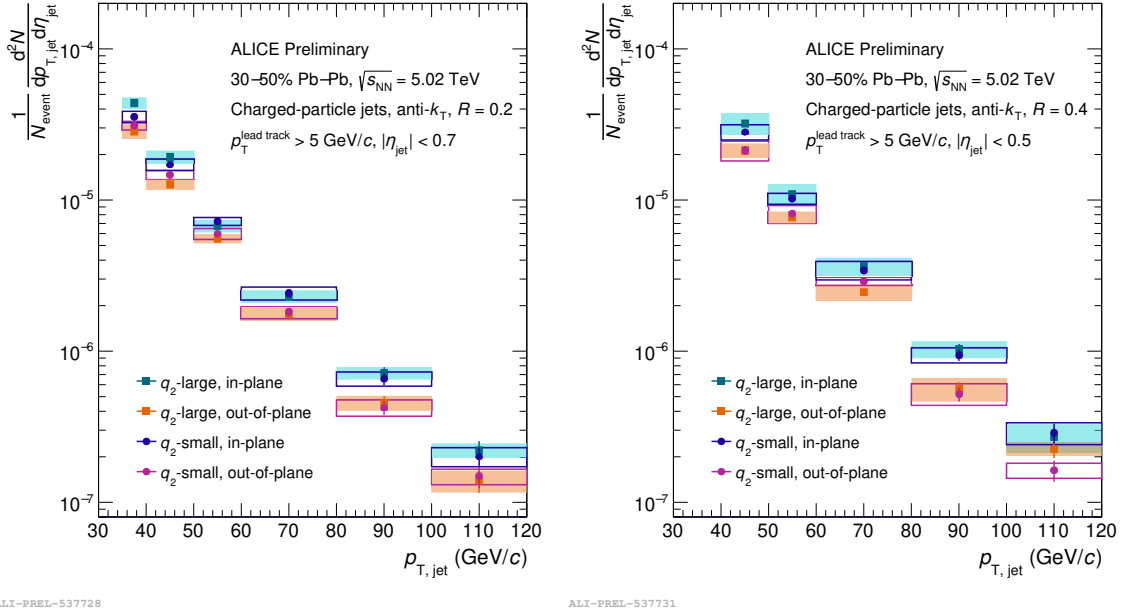
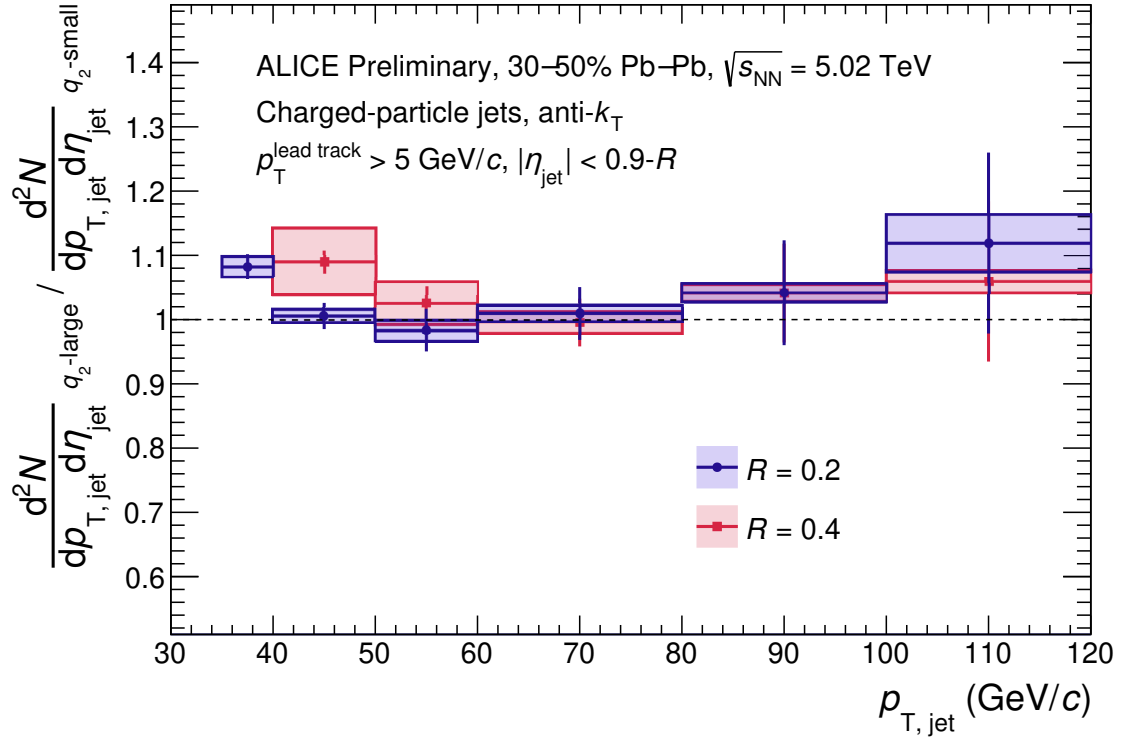


Figure 4.21: Spectra for $R = 0.2$ (left) and $R = 0.4$ (right) charged jets in 30–50% Pb–Pb collisions, reported differentially by ESE class and event-plane angle. Note that out-of-plane yields (orange + pink) appear suppressed relative to in-plane yields (blue + purple) throughout the p_T range, consistent with expectations from the jet- v_2 measurement. Large systematic uncertainties obscure any further interpretation about the impact of the event shape.

The ratio of charged jet yields from q_2 -large events to q_2 -small events is shown in Fig. 4.22. These results are compatible with unity for both $R = 0.2$ (indigo) and $R = 0.4$ (pink), with a hint of a deviation at low- p_T . This data is consistent with the Trajectum calculations showing that the average pathlength traversed by a hard probe does not change significantly with the event shape (see Fig 3.8). These results also suggest that the jet measurements performed for this analysis are insensitive to the shape of the underlying event, providing evidence for the robustness of the background subtraction used. This compares well with, for example, earlier ESE measurements made in the heavy-flavor sector. Similarly, these results show no meaningful sensitivity of D-meson production to the underlying flow (see left panel of Fig. 4.3).

Looking more differentially, a comparison of the ratios of out-of-plane to in-plane jets between q_2 -large and q_2 -small classes can be seen in Fig. 4.23 and Fig. 4.24, for R



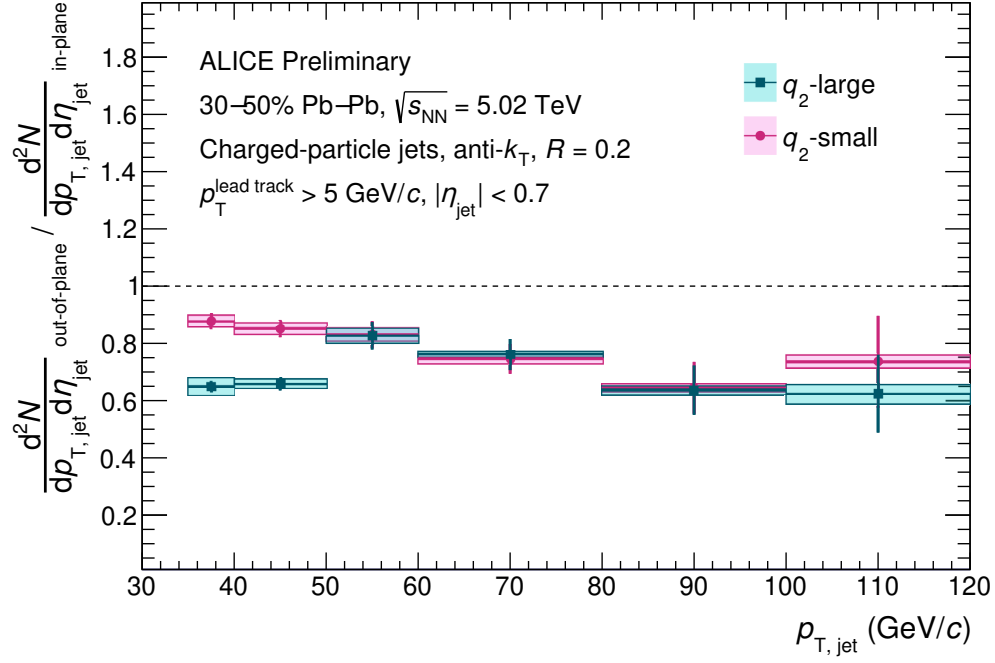
ALI-PREL-537544

Figure 4.22: Ratio of charged jets from q_2 -large events to q_2 -small events for $R = 0.2$ (indigo) and $R = 0.4$ (pink). Results are compatible with unity, indicated no dependence of inclusive charged jet production to the underlying event shape.

$= 0.2$ and $R = 0.4$, respectively. For both sets of results, a suppression from unity is observed, indicating a non-zero azimuthal anisotropy of jet quenching. In addition to the overall anisotropy, a significant deviation between the q_2 -small and q_2 -large curves can be seen at $p_T < 50$ GeV/c for $R = 0.2$. For $R = 0.4$, no significant difference can be seen between the curves.

4.4 Discussion

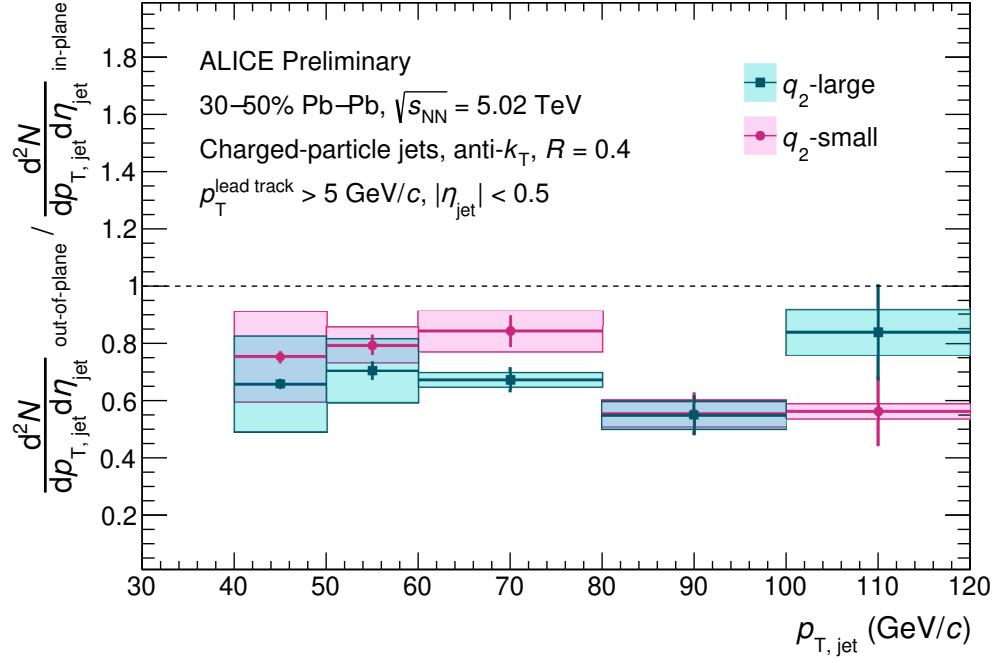
As noted in the **Results** section, the out-of-plane vs. in-plane ratios show significant suppression from unity for $R = 0.2$ and $R = 0.4$ jets in both q_2 -small and q_2 -large event classes. To compare the magnitude of this suppression with that seen in previous measurements, the data used for this analysis was used to reproduce the jet- v_2 . To



ALI-PREL-537622

Figure 4.23: Ratio of out-of-plane to in-plane $R = 0.2$ jets for q_2 -small (pink) and q_2 -large (blue) events. Both results are suppressed from unity over the full p_T range. A significant deviation between these curves can be seen at $p_T < 50$ GeV/c, where there is more relative suppression in the elliptical events than in the isotropic events. This is consistent with expectations of increased energy loss for jets traveling greater distances through the QGP.

allow for a more direct comparison with the v_2 values published by ALICE, out-of-plane and in-plane definitions were relaxed to $\pm 45^\circ$ around Ψ_2 (as opposed to $\pm 30^\circ$). These comparisons can be seen in Fig. 4.25. For $R = 0.2$, the results from this analysis are consistent with the published ALICE results. The $R = 0.4$ results are also consistent within uncertainties, although the nominal points show a slight enhancement. Note that there are several analysis-level differences between the results from this analysis and the published results. For example, this analysis imposes a leading track bias of 5 GeV/c, whereas the published result only requires a leading track of 3 GeV/c. Additionally, this analysis was performed for data with a collision energy of $\sqrt{s_{NN}} = 5.02$ TeV, whereas the published result was for $\sqrt{s_{NN}} = 2.76$ TeV. Despite these differences, the agreement indicates that the azimuthal dependence of quenching is consistent between systems. The slight enhancement of the $R = 0.4$



ALI-PREL-537722

Figure 4.24: Ratio of out-of-plane to in-plane $R = 0.4$ jets for q_2 -small (pink) and q_2 -large (blue) events. Both results are suppressed from unity over the full p_T range. No significant deviation between these curves can be seen.

points does provoke some interest. This would be consistent with the R -dependence of the R_{AA} , which indicated that larger- R jets are more quenched. It would therefore follow that they also more sensitive to the pathlength they traverse. One should, however, be careful not to over-interpret the data, as the v_2 uncertainties (particularly for $R = 0.4$) are quite large.

While the v_2 provides an interesting comparison to existing measurements, the novel contribution of this analysis regards the results for different ESE classes. For the $R = 0.2$ study (see Fig. 4.23), a deviation between the out-of-plane/in-plane ratios is observed between the large- q_2 and small- q_2 samples below 50 GeV/c. To assess the significance of this deviation, one can consider a double ratio of the large- q_2 to small- q_2 single-ratios. This was done by first unfolding the differentiated spectra in the usual way (see **Section 4.2.1: Unfolding**), and then merging the first two bins to account for any correlations between them. The single ratios and systematic uncertainties were then computed in the same way to produce a rebinned version of

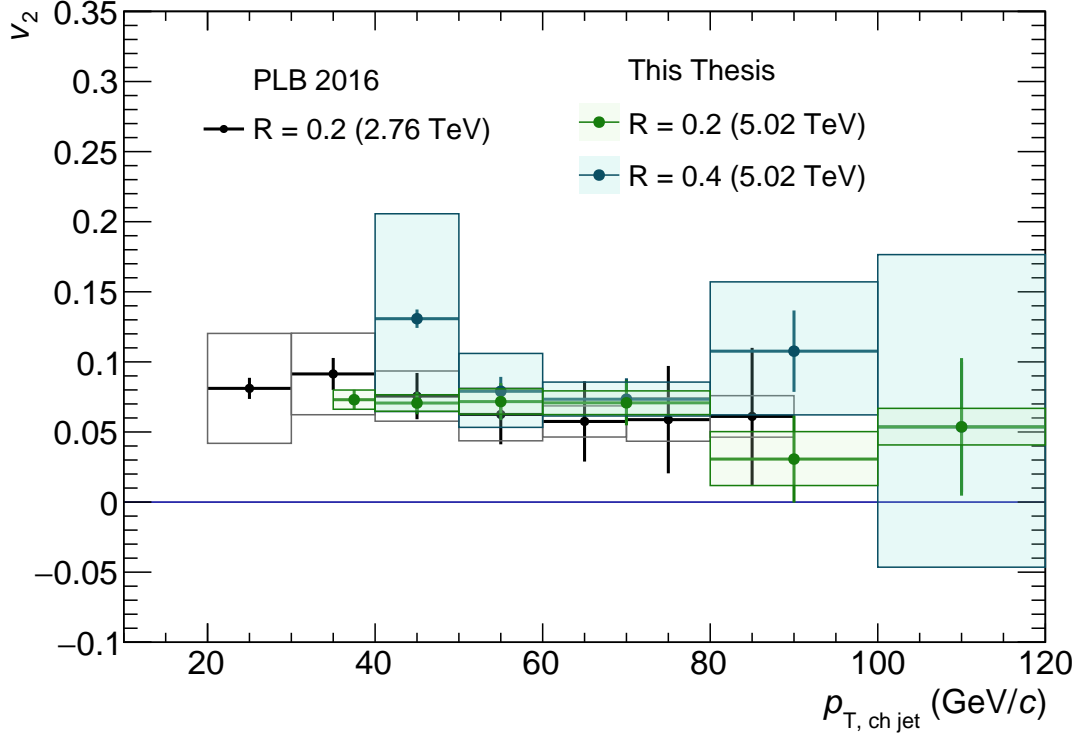


Figure 4.25: Comparison of published v_2 results with the results derived in this analysis. While there are several differences between the published analysis and this analysis (i.e. collision energy, leading track bias, etc.), the $R = 0.2$ results are compatible. The $R = 0.4$ results show a slight deviation in the nominal values, but are consistent within reported uncertainties.

Fig. 4.23. The systematic uncertainties were then added in quadrature, assuming no correlation between the large- q_2 and small- q_2 classes. The same was done for the statistical uncertainties. The results of this study can be seen in Fig. 4.26.

For the lowest bin, the nominal value is 1.32, with a 1σ systematic uncertainty of 0.0364 (fractional value of 2.8%) and a 1σ statistical uncertainty of 0.044 (fractional value of 3.3%). Summing these values in quadrature gives a total uncertainty of 0.056 (fractional value of 4.3%). This puts the nominal value at 5.7σ away from unity.

While such a result seems to be a clear signal of pathlength dependent suppression, it is not yet apparent why this separation does not extend to higher p_T . Intuitively, this is not entirely unexpected, given that the R_{AA} increases with p_T and the jet- v_2 decreases with p_T . These results indicate that jets are relatively less quenched

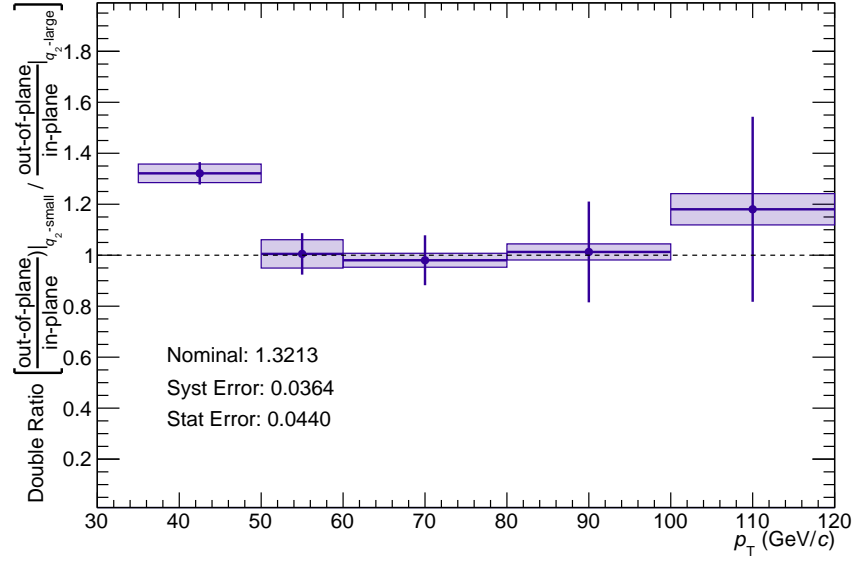


Figure 4.26: Double ratio of the single-ratios reported in Fig. 4.23. The lowest two bins have been merged to account for correlations between them. The nominal values in the lowest bin are approximately 5.7σ away from unity.

at higher p_T . It therefore seems plausible that jets would be less sensitive to slight differences in pathlength at higher p_T . One must be careful not to overinterpret the high- p_T regime of this measurement, however, given that significant statistical uncertainties dominate in that regime. It is therefore unclear if the agreement is due to a true physics effect or due to the fact that we are not experimentally sensitive to the differences in that regime. For this reason, future studies with improved statistics will be highly beneficial for understanding the kinematics of this dependence.

“Always look on the bright side of life.”

— Eric Idle, *Life of Brian*

Chapter 5

Outlook

The current ALICE measurement of jets with event-shape engineering is an exciting step towards constraining the pathlength dependence of jet energy loss. However, this is just the beginning! Hope springs eternal, and there is cause for optimism that model comparisons will enable the current qualitative observations to be transformed into quantitative constraints. Additionally, new observables will become experimentally accessible with upcoming data-taking periods and the installation of next-generation detectors. There are many new avenues of physics waiting to be explored; answers to our enduring questions appear within reach, and will likely beget new questions to accompany these answers.

This chapter will discuss some future prospects for learning more about jet quenching’s pathlength dependence. These include new ideas for observables, as well as proposals for old observables that can be studied in new ways. A brief introduction to various new experiments on the horizon, and what we can hope to gain from these facilities, will also be given. Finally, this chapter will summarize the work presented in this thesis and what has been learned from these studies.

5.1 Future Directions

This thesis includes the first measurement of jets using ESE, opening a new avenue with which to study jet quenching phenomena. Several imminent developments in the experimental landscape will allow for extensions of this measurement. This section will present some possible future avenues with which ESE can be used in the high- p_T sector. Additionally, other ideas to study the pathlength dependence of jet quenching will be discussed.

5.1.1 Increased Statistics

After the end of Long Shutdown 2 [56] in 2022, the long-anticipated pp data-taking period has begun at the LHC. With the first heavy-ion run scheduled for later this year, ALICE is looking forward to increased Pb–Pb luminosities. In LHC Runs 3 and 4, ALICE is expecting to record 50-100 times more Pb–Pb events than were collected for the minimum bias data-set during Run 2 [37]. These statistics will greatly improve the ESE measurement presented here in the following ways.

First, for the current ESE measurement of $R = 0.2$ jets, ratios of out-of-plane to in-plane jets for q_2 -large and q_2 -small events (Fig. 4.23) are consistent within their uncertainties at high- p_T . Note, however, that the measurement uncertainty is dominated by statistics beginning at 50 GeV/ c . This makes it impossible to distinguish if this agreement is the result of an insufficient sample size, or rather if it is the manifestation of a true physics effect. Increased statistics should enable this distinction to be made. Additionally, a larger sample will make more differential measurements in both the event-shape and the event-plane angle possible. These advancements will allow us to make progress towards studying the evolution of jet suppression as a continuous function of event-shape quantities.

5.1.2 Substructure and ESE

As the field of jet substructure develops, ESE offers a promising avenue to further contextualize existing measurements. For example, consider the groomed jet radius

R_g , which quantifies the distance between the two leading prongs of a jet (a schematic can be seen in Fig. 5.1). The R_g is an interesting observable with which to study jet quenching due to the modification observed between pp and Pb–Pb, in which a relative narrowing is seen in heavy-ion collisions [52]. By considering the R_g of jets with respect to the event-plane angle, one could assess the pathlength dependence of this narrowing. Further, constraining the medium fluctuations using ESE would allow for a more differential study of this effect, just as was done with the p_T spectrum. An additional benefit of using ESE in this context would be to minimize interpretation uncertainties due to the survivor bias. Here, we refer to the loss of information introduced by jets that are so suppressed in the QGP that they are never measured. ESE can help here given that the relative difference between events with different shapes is considerably smaller than the difference between Pb–Pb and pp .

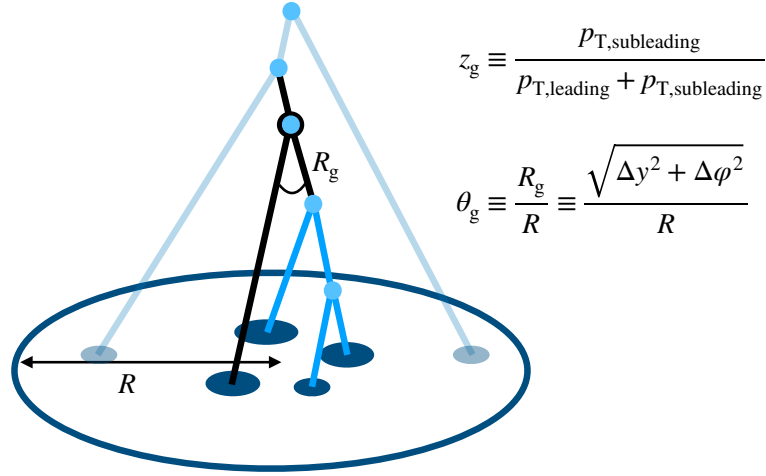


Figure 5.1: The R_g quantifies the distance between a jet's two leading prongs. Figure taken from Ref. [52].

Performing such a measurement will require a significant increase in statistics to allow for 3D unfolding. It will therefore be interesting to see if this is possible in ALICE with Run 3 data, and if so, what we can learn about the evolution of substructure with pathlength.

5.1.3 Dijet Asymmetry

As was discussed in **Section 4.1: Previous Results**, azimuthal anisotropy is not the only way to study pathlength-dependent energy loss. The dijet asymmetry, while incomplete, does augment our understanding of this process.¹ Unfortunately, ALICE does not currently have such a measurement. While, due to the limited fiducial coverage of the ALICE calorimeters, such a measurement is all but prohibited with full jets, it could still be studied using charged jets. The interpretation of such an observable is indeed more complicated, given that uncertainties surrounding charge-to-neutral fluctuations obscure expectations for the results.

Even given this caveat, a charged-dijet asymmetry could serve as a useful comparison point for other efforts in ALICE, such as the ongoing photon-jet correlation measurement [118]. Because this analysis is limited to studying the correlations between photons and charged jets, it is not directly comparable to analyses from other experiments, who prefer to boast their impressive calorimeters by measuring the correlations between photons and full jets [119]. A charged-dijet asymmetry using ALICE data would therefore provide interesting context.

In addition to providing a point of reference for other measurements, such an analysis could prove an interesting study in its own right. For example, if this result were to agree with what is seen for full jets at ATLAS [97], it could suggest that the concern over charge fluctuations is unfounded. Conversely, if such a result disagreed qualitatively with the existing literature, it could provide insight into the ways the charged vs. neutral components of a jet lose energy to the medium.

Given the above motivations, the possibility of performing a charged-dijet asymmetry measurement in ALICE has been briefly studied for the purpose of this thesis. The embedded spectra at truth-, detector-, and hybrid-levels can be seen for leading jets in Fig. 5.2. While the statistics shown in these results indicate that a full study is likely feasible, a few considerations must be made. First, the use of extractor bins is not practical for this measurement. This is because the current implementation down-samples statistics on a jet-by-jet basis, as opposed to down-sampling event-by-

¹See **Section 4.1.1: Dijet Asymmetry** for more details on this observable.

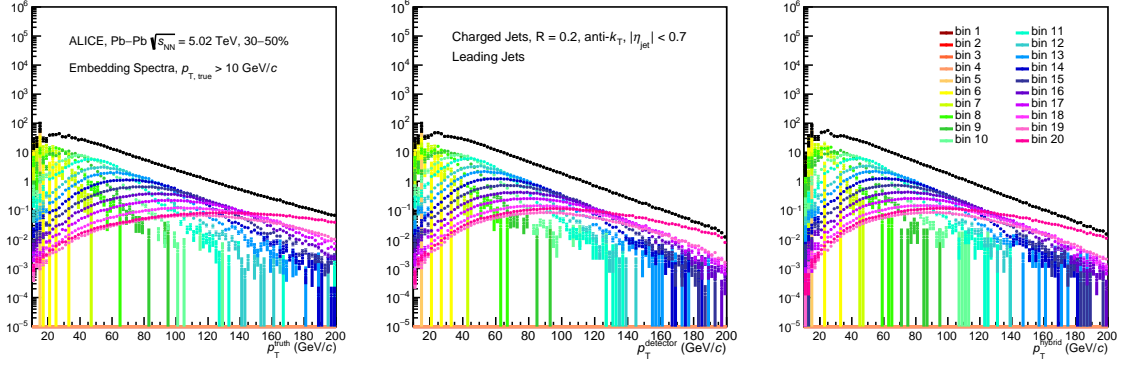


Figure 5.2: Truth- (left), detector- (middle), and hybrid-level (right) spectra for leading jets in the embedded sample.

event.² This introduces the situation where a leading jet may be recorded, but the subleading jet is not. In this case, a sub-sub-leading jet might be recorded in its place. Alternatively, the leading jet may be discarded, resulting in the false identification of a subleading jet as leading, and a sub-sub-leading jet as subleading. This is obviously not desirable. Additionally, this introduces problems with scaling the input for the response. See Fig. 5.3 for a visual representation of this issue.

In addition to the use of extractor bins, the use of a leading track bias to suppress combinatorial background poses difficulties for this measurement. This is because the fragmentation patterns of the leading and subleading jets may be significantly different. However, removing a leading track bias without further consideration amplifies contamination from combinatorial jets, as well as greatly increases the size of the data output files. Some consideration must be given, therefore, to mitigate this problem.

²See **Section 4.2.1: Embedding and the Response** for more details on the use of extractor bins.

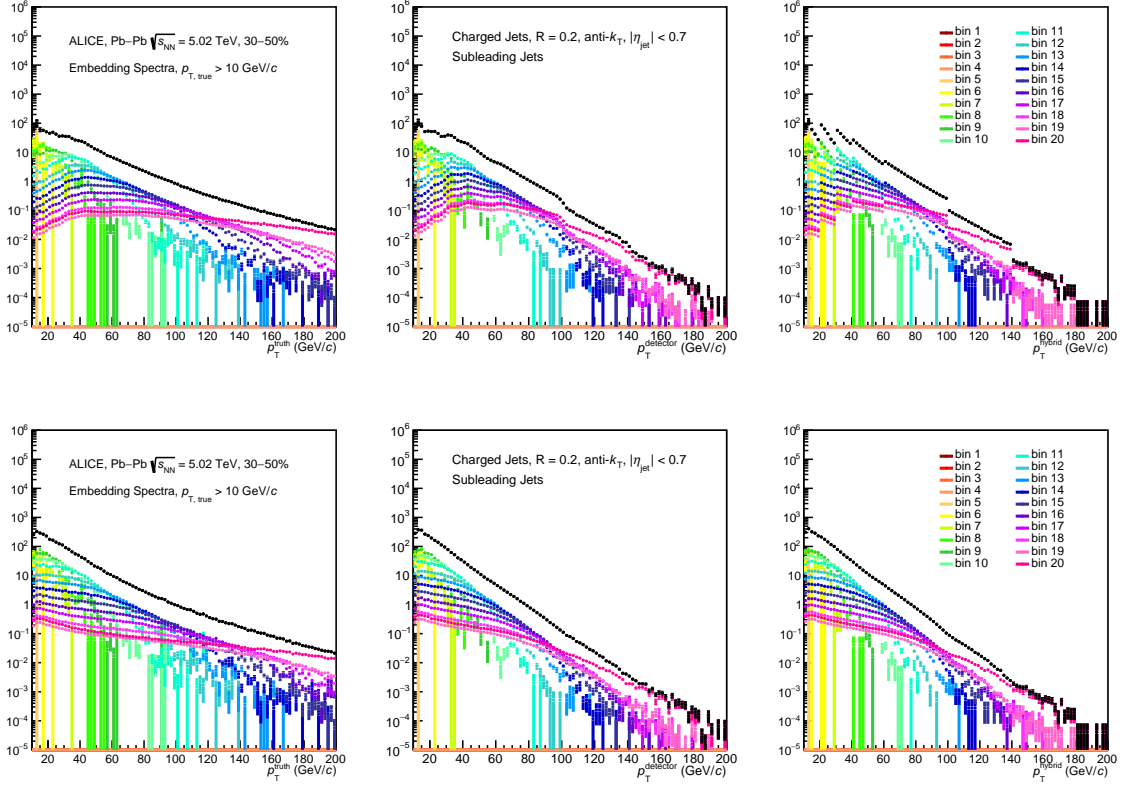


Figure 5.3: Truth-, detector-, and hybrid-level spectra for embedded subleading jets. Top: Jets are scaled using the same extractor bin as the leading jet. This introduces discontinuities in the spectrum. Bottom: Jets are scaled using the extractor bin corresponding to the subleading jet. This scaling produces smooth spectra, but introduces ambiguity into how dijet pairs should be scaled when entered into the response matrix.

5.1.4 New Experiments

Studies of pathlength dependence will benefit from the enhanced capabilities of next-generation experiments. On the immediate horizon, sPHENIX [120] will come online at RHIC this year. It's design has been optimized for the study of jets, and includes a hadronic calorimeter. The combination of good tracking, neutral particle information, and great statistics will enable sPHENIX to make measurements of full jets that are not currently possible at ALICE. Additionally, their focus as a heavy-ion detector will allow them to measure soft behavior of the QGP in a way that is not possible at e.g. CMS and ATLAS, thus providing new opportunities for the study of correlations between soft- and hard-scale physics.

In addition to sPHENIX, the poorly-named but well-designed ALICE 3 detector [121] is intended to come online for the LHC’s Run 5. Much of the focus of its design is geared towards measuring heavy-flavor hadrons, studies of which commonly seek to understand the behavior of heavy-flavor partons in the medium. Because these partons are too massive to be produced thermally, they are typically generated in hard scatterings. Many heavy-flavor analyses would therefore benefit from considering the complete jet so as to approximate the full kinematics of the initiating parton. For this reason, jets will be an important part of the ALICE 3 physics program.

5.2 Conclusions

In this thesis, we have presented the first measurement of jets using event-shape engineering. This newly developed method has shown that jet production is insensitive to the shape of the underlying event in 30–50% Pb–Pb collisions. However, when considering the azimuthal angle of the jets with respect to the event plane, differences begin to emerge. These results reproduce the azimuthal anisotropy seen in previous measurements, and build upon those studies by further constraining the medium fluctuations, thus providing better knowledge of the pathlength distributions that jet samples traverse. At $p_T < 50$ GeV/ c , a deviation is observed between ratios of out-of-plane to in-plane jets from highly-elliptical and highly-spherical events. While model predictions are required to extract explicit constraints from this measurement, the qualitative effect agrees with the intuition that jet energy loss occurs in a pathlength-dependent manner.

This is an important step towards constraining the pathlength dependence of jet quenching, but in many ways, this is just the beginning. In Run 3, enhanced statistics will allow for an improvement on this measurement by enabling higher precision studies at high p_T , as well as allowing for a more differential measurement in q_2 and $\Delta\varphi$. Additionally, increased statistics will allow for ESE to be used as a technique to study more observables than just the jet- p_T . For example, exploring substructure modification with ESE may provide a particularly rich path to studying jet–

medium interactions. Finally, model comparisons will allow qualitative observations of pathlength-dependent energy loss to be converted into quantitative constraints, enabling a better understanding of the fundamental mechanisms that drive jet energy loss in the QGP.

“My numbers mean more to me than my name.”

— Vera Rubin

Appendix A

Data Tables

This appendix includes the point values and associated uncertainties for the final results.

Data associated with Fig. 4.21 (Left)

R = 0.2, q_2–small, in-plane			
p_T range [GeV/ c]	Nominal	Systematic [abs.(%)]	Statistical [abs. (%)]
35-40	3.555e-5	3.08953e-6 (8.69067)	7.47122e-7 (2.10161)
40-50	1.72207e-5	1.5369e-6 (8.92476)	4.15563e-7 (2.41316)
50-60	7.228e-6	4.35036e-7 (6.01876)	2.80085e-7 (3.875)
60-80	2.42924e-6	2.25844e-7 (9.29688)	1.15210e-7 (4.74262)
80-100	6.5727e-7	7.05783e-8 (10.7381)	6.13132e-8 (9.32846)
100-120	2.01512e-7	2.95791e-8 (14.6786)	3.00509e-8 (14.9127)

R = 0.2, q_2–small, out-of-plane			
p_T range [GeV/ c]	Nominal	Systematic [abs.(%)]	Statistical [abs. (%)]
35-40	3.11962e-05	1.98594e-6 (6.36599)	7.41440e-7 (2.3767)
40-50	1.4667e-05	1.01948e-6 (6.95085)	3.78243e-7 (2.57887)
50-60	6.00466e-06	4.94228e-7 (8.23074)	2.45942e-7 (4.09586)
60-80	1.81153e-06	1.55523e-7 (8.5852)	9.28469e-8 (5.12533)
80-100	4.23813e-07	5.25579e-8 (12.4012)	4.44542e-8 (10.4891)
100-120	1.48192e-07	1.75431e-8 (11.8381)	2.36709e-8 (15.9731)

R = 0.2, q_2–large, in-plane			
p_T range [GeV/ c]	Nominal	Systematic [abs.(%)]	Statistical [abs. (%)]
35-40	4.40682e-05	3.57307e-6 (8.10805)	8.26874e-7 (1.87635)
40-50	1.92114e-05	1.79283e-6 (9.33212)	4.35219e-7 (2.26542)
50-60	6.74768e-06	5.99741e-7 (8.8881)	2.62728e-7 (3.89361)
60-80	2.31338e-06	2.17755e-7 (9.41285)	1.11509e-7 (4.82016)
80-100	7.16676e-07	6.41464e-8 (8.95055)	6.36389e-8 (8.87973)
100-120	2.22272e-07	2.35279e-8 (10.5852)	3.17876e-8 (14.3012)

R = 0.2, q_2–large, out-of-plane			
p_T range [GeV/ c]	Nominal	Systematic [abs.(%)]	Statistical [abs. (%)]
35-40	2.86149e-05	3.17539e-6 (11.097)	6.93496e-7 (2.42355)
40-50	1.26598e-05	9.49086e-7 (7.49685)	3.46121e-7 (2.73402)
50-60	5.57683e-06	3.61620e-7 (6.48432)	2.39815e-7 (4.30021)
60-80	1.75997e-06	1.69874e-7 (9.65208)	9.28080e-8 (5.27327)
80-100	4.56287e-07	4.88711e-8 (10.7106)	4.68278e-8 (10.2628)
100-120	1.38499e-07	2.20903e-8 (15.9498)	2.24940e-8 (16.2413)

Data associated with Fig. 4.21 (Right)

R = 0.4, q_2–small, in-plane			
p_T range [GeV/ c]	Nominal	Systematic [abs.(%)]	Statistical [abs. (%)]
40-50	2.83444e-05	3.37712e-6 (11.9146)	5.32416e-7 (1.87838)
50-60	1.02372e-05	8.11907e-7 (7.93095)	2.96899e-7 (2.9002)
60-80	3.44454e-06	4.83851e-7 (14.0469)	1.48796e-7 (4.31975)
80-100	9.43231e-07	1.06951e-7 (11.3388)	8.10705e-8 (8.59498)
100-120	2.89383e-07	4.64280e-8 (16.0438)	4.23445e-8 (14.6327)

R = 0.4, q_2–small, out-of-plane			
p_T range [GeV/ c]	Nominal	Systematic [abs.(%)]	Statistical [abs. (%)]
40-50	2.13271e-05	3.18793e-6 (14.9478)	4.95420e-7 (2.32296)
50-60	8.12698e-06	1.12685e-6 (13.8656)	2.89202e-7 (3.55854)
60-80	2.90138e-06	1.78716e-7 (6.15969)	1.36400e-7 (4.70124)
80-100	5.23168e-07	8.52241e-8 (16.29)	5.28823e-8 (10.1081)
100-120	1.6278e-07	1.86222e-8 (11.4401)	2.58648e-8 (15.8894)

R = 0.4, q_2–large, in-plane			
p_T range [GeV/ c]	Nominal	Systematic [abs.(%)]	Statistical [abs. (%)]
40-50	3.22841e-05	5.33384e-6 (16.5216)	5.29046e-7 (1.63872)
50-60	1.09158e-05	1.74052e-6 (15.945)	2.83731e-7 (2.59927)
60-80	3.6585e-06	4.84722e-7 (13.2492)	1.46031e-7 (3.99156)
80-100	1.03003e-06	1.25468e-7 (12.181)	8.03581e-8 (7.80153)
100-120	2.71655e-07	5.66344e-8 (20.8479)	3.92101e-8 (14.4338)

R = 0.4, q_2–large, out-of-plane			
p_T range [GeV/ c]	Nominal	Systematic [abs.(%)]	Statistical [abs. (%)]
40-50	2.12367e-05	2.14796e-6 (10.1144)	4.99693e-7 (2.35297)
50-60	7.69497e-06	6.49025e-7 (8.43441)	2.85218e-7 (3.70655)
60-80	2.46135e-06	3.09402e-7 (12.5704)	1.25204e-7 (5.08681)
80-100	5.65488e-07	9.59316e-8 (16.9644)	5.68479e-8 (10.0529)
100-120	2.27711e-07	2.49400e-8 (10.9525)	3.16284e-8 (13.8897)

Data associated with Fig. 4.22

R = 0.2, q_2–large/q_2–small			
p_T range (GeV/ c)	Nominal	Systematic [abs. (%)]	Statistical [abs. (%)]
35-40	1.08246	0.0157909 (1.4588)	0.0193057 (1.7835)
40-50	1.0056	0.00967784 (0.962395)	0.0203725 (2.02589)
50-60	0.983208	0.0162832 (1.65613)	0.0327464 (3.33057)
60-80	1.00948	0.0124436 (1.23267)	0.0410876 (4.07019)
80-100	1.04178	0.0142944 (1.37211)	0.081609 (7.83357)
100-120	1.11909	0.0442910 (3.95777)	0.140832 (12.5846)

R = 0.4, q_2–large/q_2–small			
p_T range (GeV/ c)	Nominal	Systematic [abs. (%)]	Statistical [abs. (%)]
40-50	1.09023	0.0515809 (4.73119)	0.0179449 (1.64597)
50-60	1.0252	0.0335589 (3.2734)	0.0265149 (2.58633)
60-80	0.995436	0.0163073 (1.63821)	0.0371636 (3.7334)
80-100	1.04123	0.0130130 (1.24977)	0.0769269 (7.38806)
100-120	1.05941	0.0176339 (1.6645)	0.124718 (11.7724)

Data for Fig. 4.23

R = 0.2, q_2–large, out/in ratio			
p_T range [GeV/ c]	Nominal	Systematic [abs.(%)]	Statistical [abs. (%)]
35-40	0.649334	0.0297518 (4.58189)	0.0199022 (3.06502)
40-50	0.658972	0.0161568 (2.45182)	0.0233977 (3.55063)
50-60	0.826481	0.0259281 (3.13717)	0.0479445 (5.80104)
60-80	0.76078	0.0111103 (1.46038)	0.0543526 (7.14433)
80-100	0.636671	0.0150335 (2.36126)	0.0864033 (13.5711)
100-120	0.623107	0.0330288 (5.30066)	0.134843 (21.6404)

R = 0.2, q_2–small, out/in ratio			
p_T range (GeV/ c)	Nominal	Systematic [abs. (%)]	Statistical [abs. (%)]
35-40	0.877532	0.0200232 (2.28176)	0.0278407 (3.17261)
40-50	0.851707	0.0199458 (2.34186)	0.0300809 (3.53184)
50-60	0.830749	0.0233031 (2.80507)	0.0468410 (5.63841)
60-80	0.745717	0.0171392 (2.29835)	0.0520730 (6.98294)
80-100	0.644808	0.0140749 (2.18281)	0.0905130 (14.0372)
100-120	0.735402	0.0216091 (2.9384)	0.160704 (21.8525)

Data for Fig. 4.24

R = 0.4, q_2–large, out/in ratio			
p_T range (GeV/ c)	Nominal	Systematic [abs. (%)]	Statistical [abs. (%)]
40-50	0.657806	0.167606 (25.4796)	0.0188618 (2.86738)
50-60	0.704936	0.111488 (15.8154)	0.0319132 (4.52711)
60-80	0.672776	0.0252031 (3.74613)	0.0435012 (6.46592)
80-100	0.549004	0.0482755 (8.79329)	0.0698608 (12.725)
100-120	0.838234	0.0796332 (9.50011)	0.167910 (20.0314)

R = 0.4, q_2–small, out/in ratio			
p_T range (GeV/ c)	Nominal	Systematic [abs. (%)]	Statistical [abs. (%)]
40-50	0.752428	0.157175 (20.889)	0.0224779 (2.98738)
50-60	0.793869	0.0623428 (7.85303)	0.0364441 (4.59069)
60-80	0.842314	0.0701434 (8.32746)	0.0537776 (6.38451)
80-100	0.554655	0.0465379 (8.39042)	0.0735933 (13.2683)
100-120	0.562508	0.0261877 (4.65552)	0.121506 (21.6007)

“There is a misconception in America that women scientists are all dowdy spinsters. This is the fault of men.”

— Chien-Shiung Wu

Appendix B

Performance Studies

This Appendix contains the full set of performance and unfolding studies done for this thesis.

Embedding

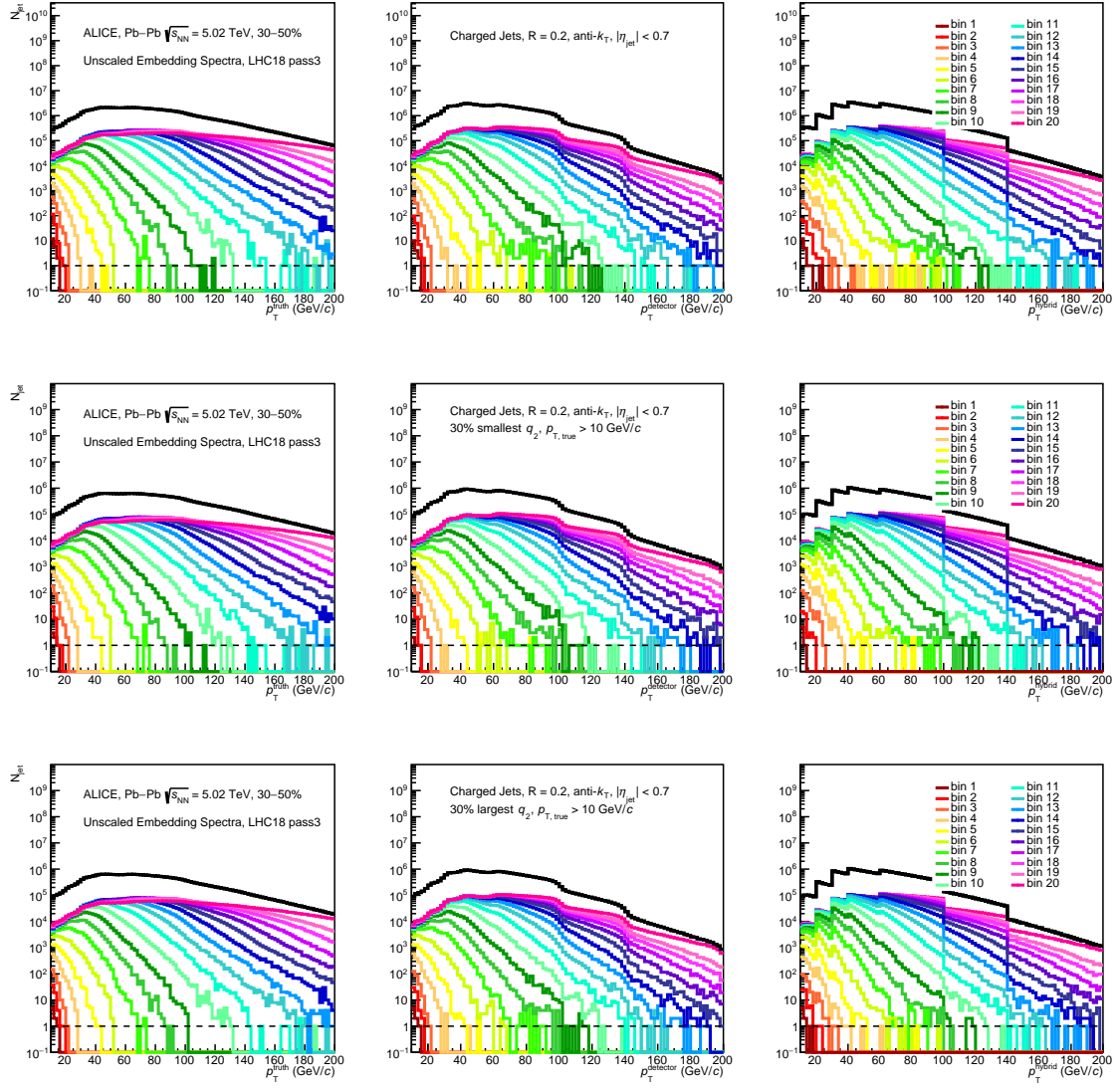


Figure B.1: Unscaled p_T^{hard} spectra for $R = 0.2$.

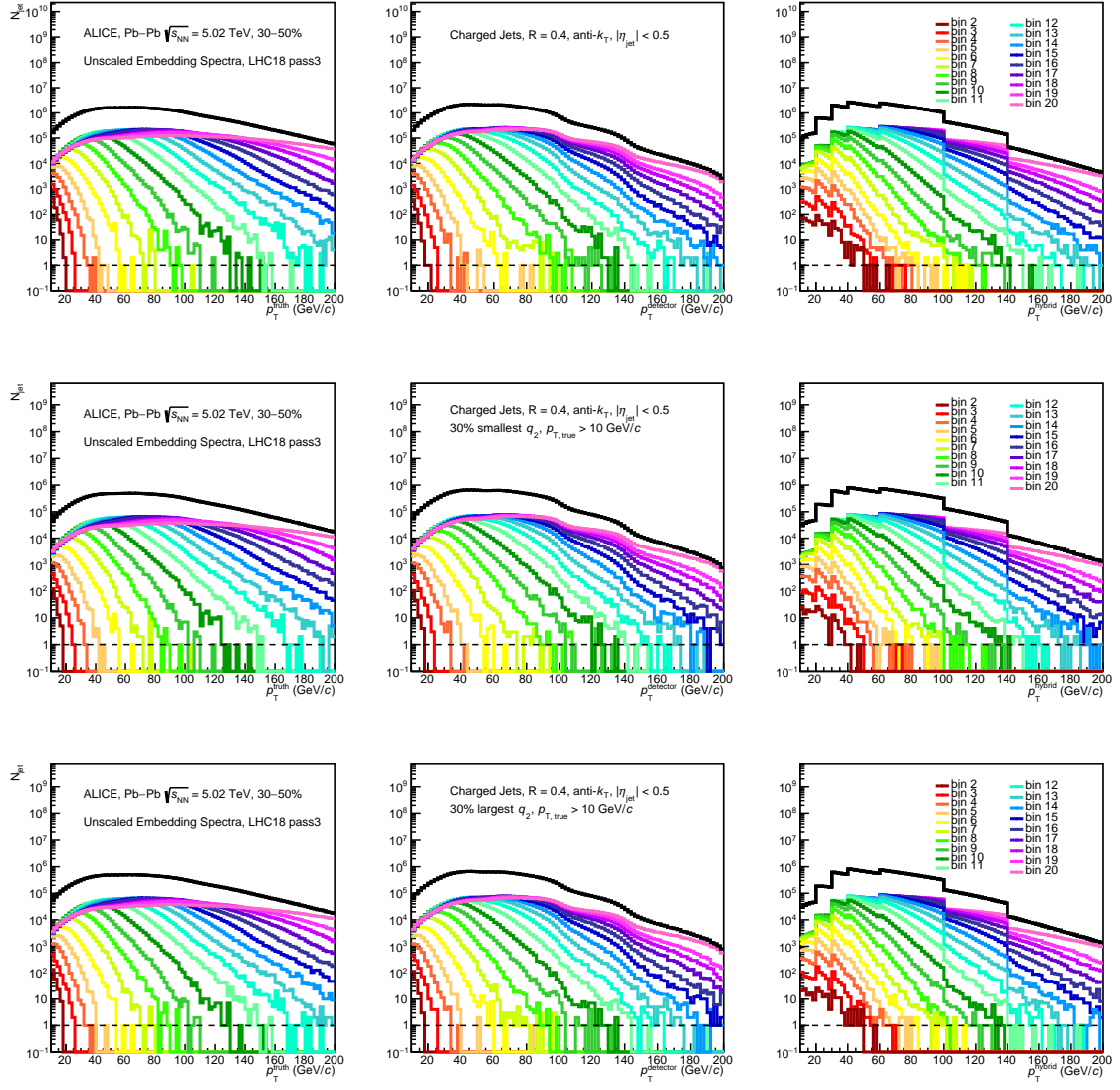


Figure B.2: Unscaled p_T^{hard} spectra for $R = 0.4$.

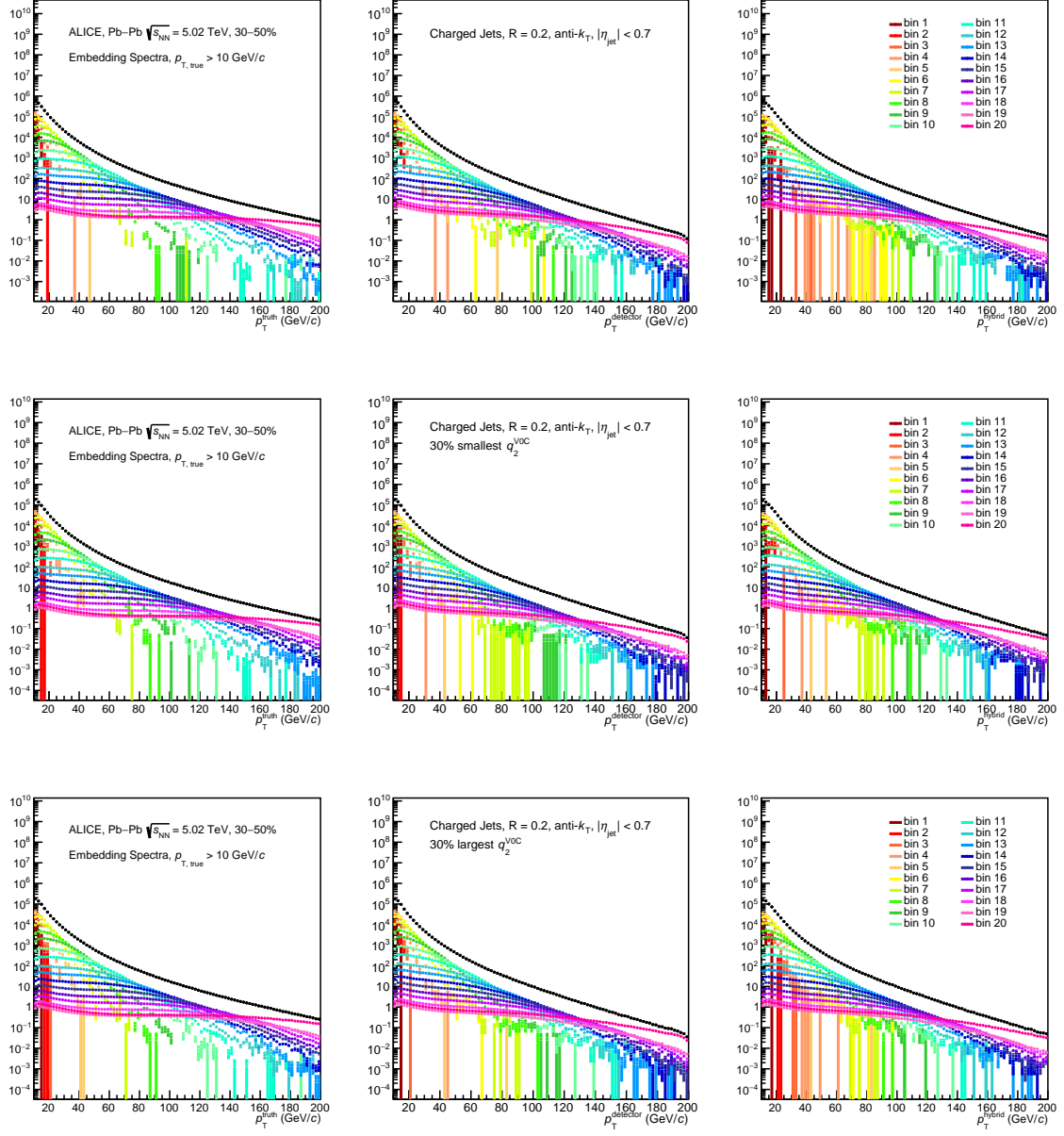


Figure B.3: Scaled p_T^{hard} spectra for $R = 0.2$

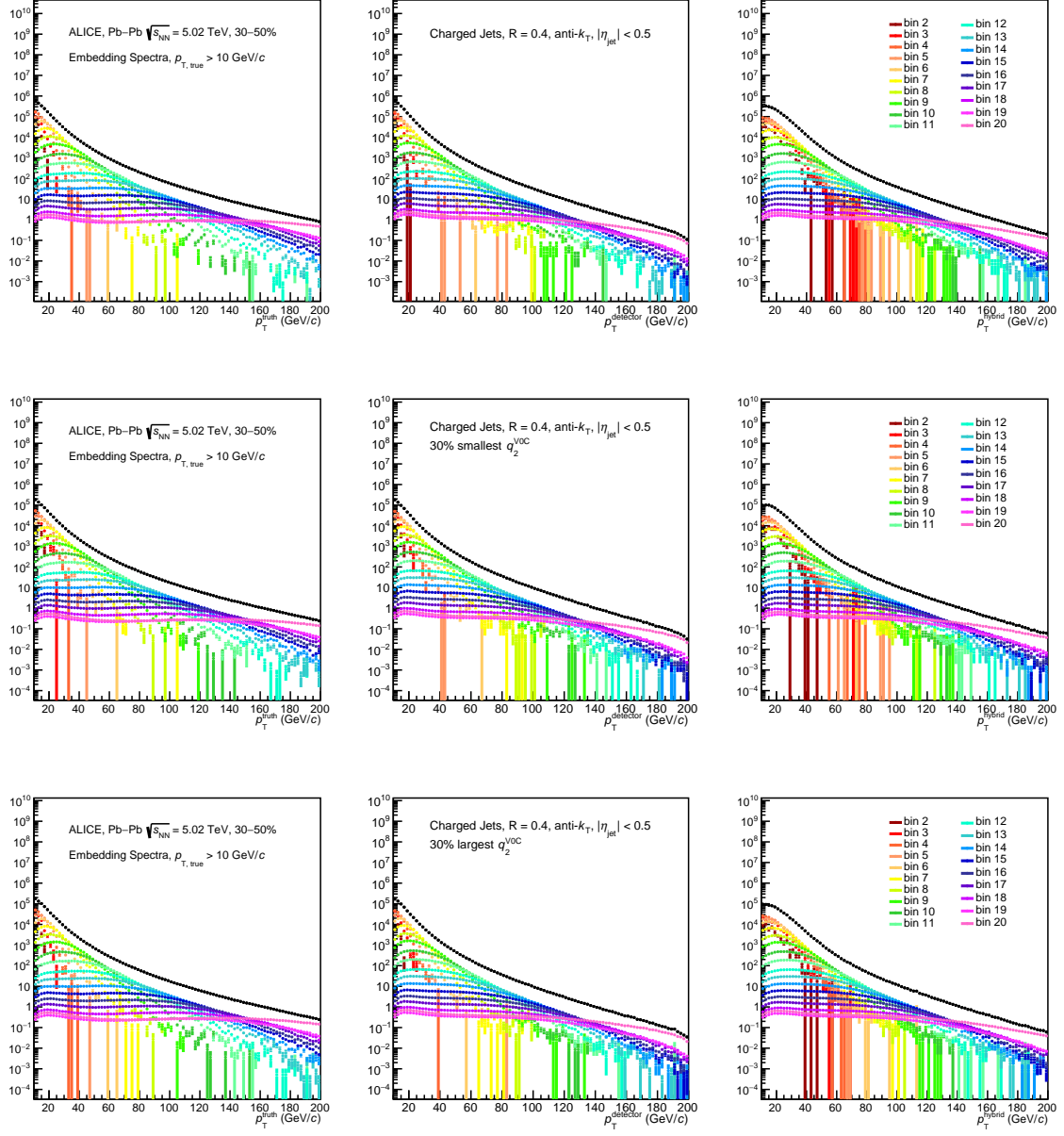


Figure B.4: Scaled p_T^{hard} spectra for $R = 0.4$.

Performance

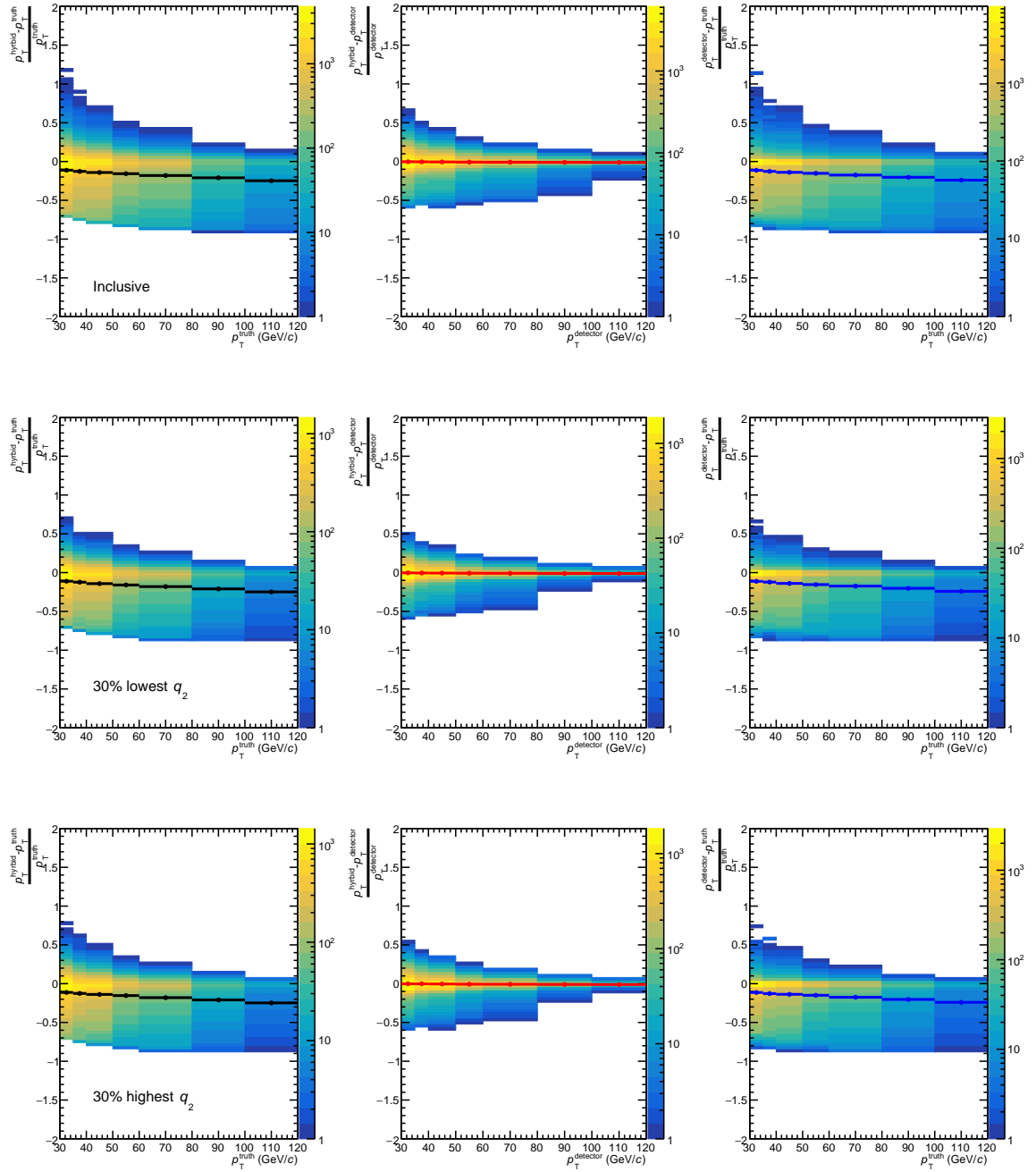


Figure B.5: Residual plots for $R = 0.2$ jets.

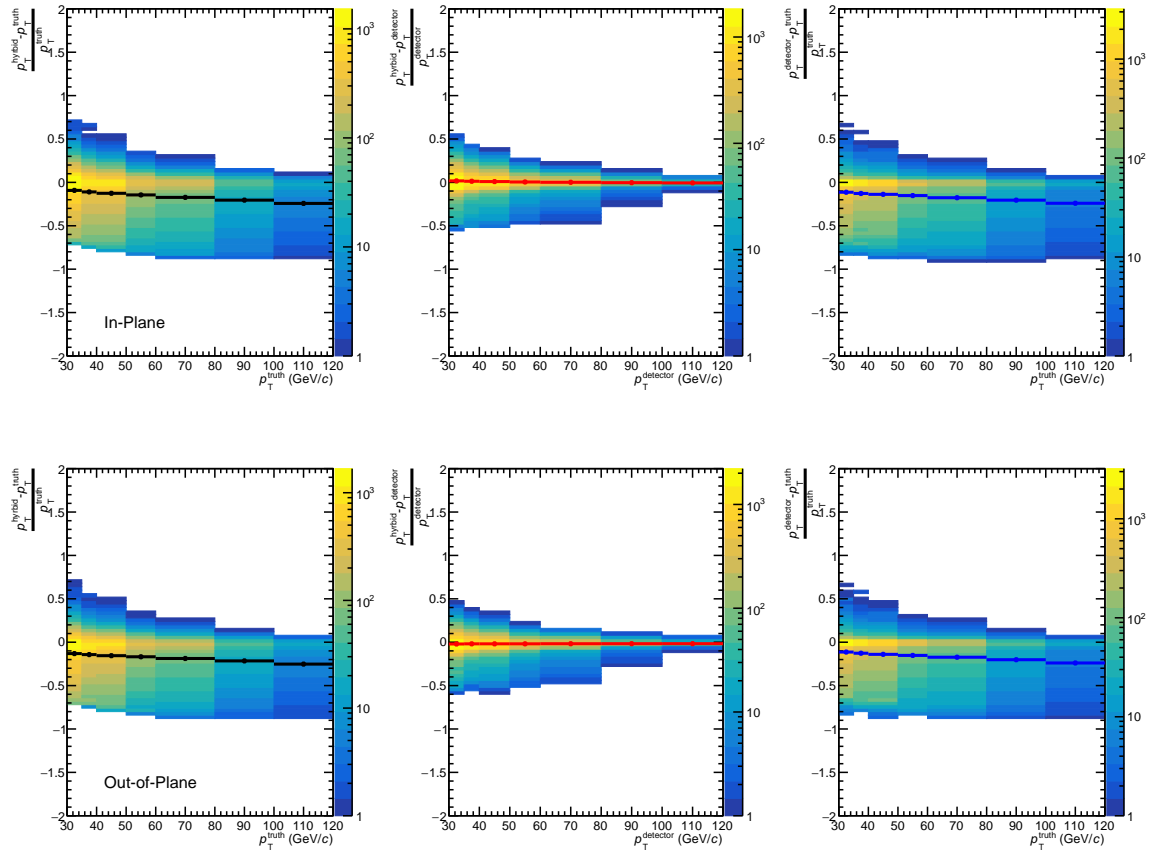


Figure B.6: Residual plots for $R = 0.2$ jets.

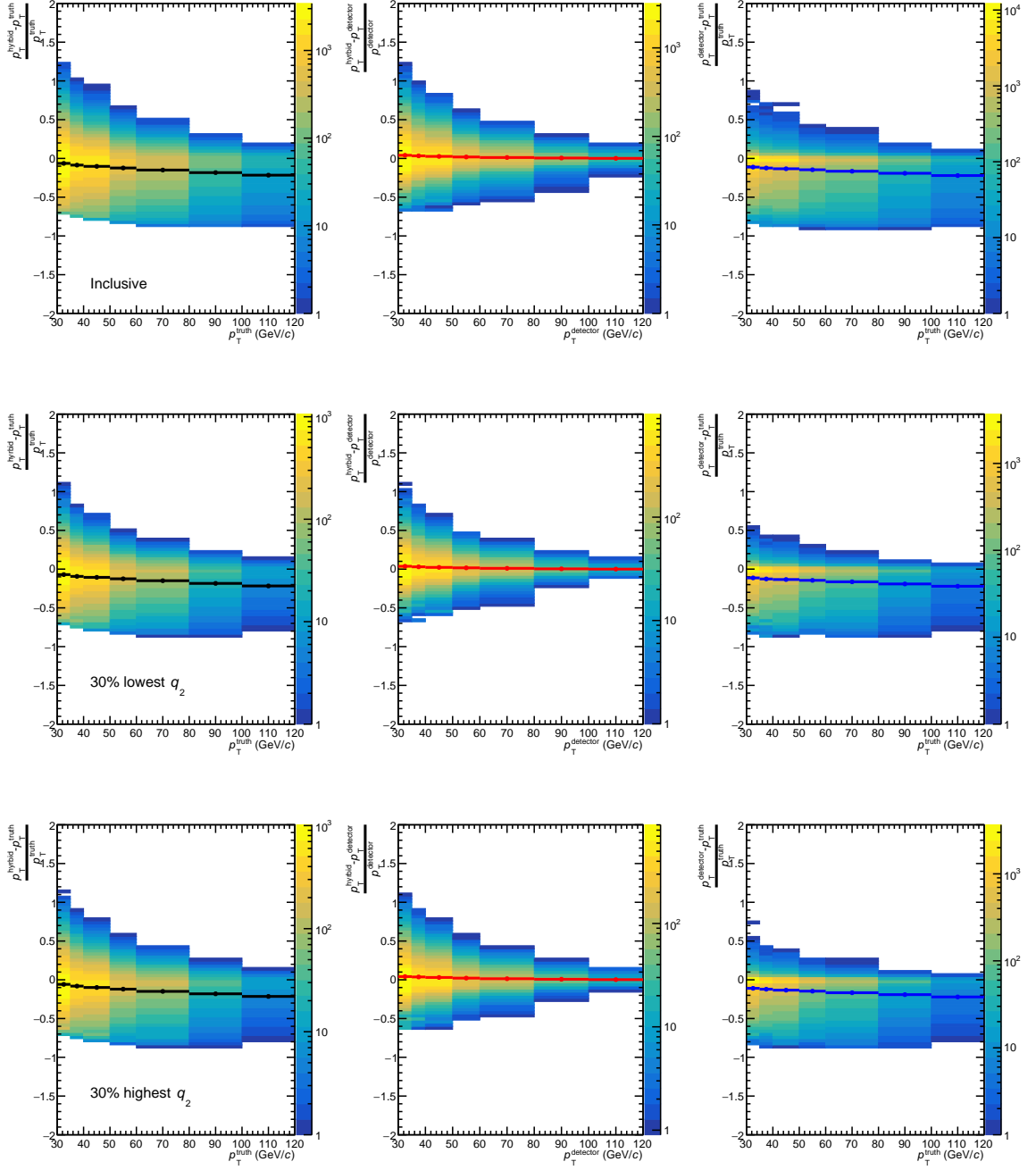


Figure B.7: Residual plots for $R = 0.4$ jets.

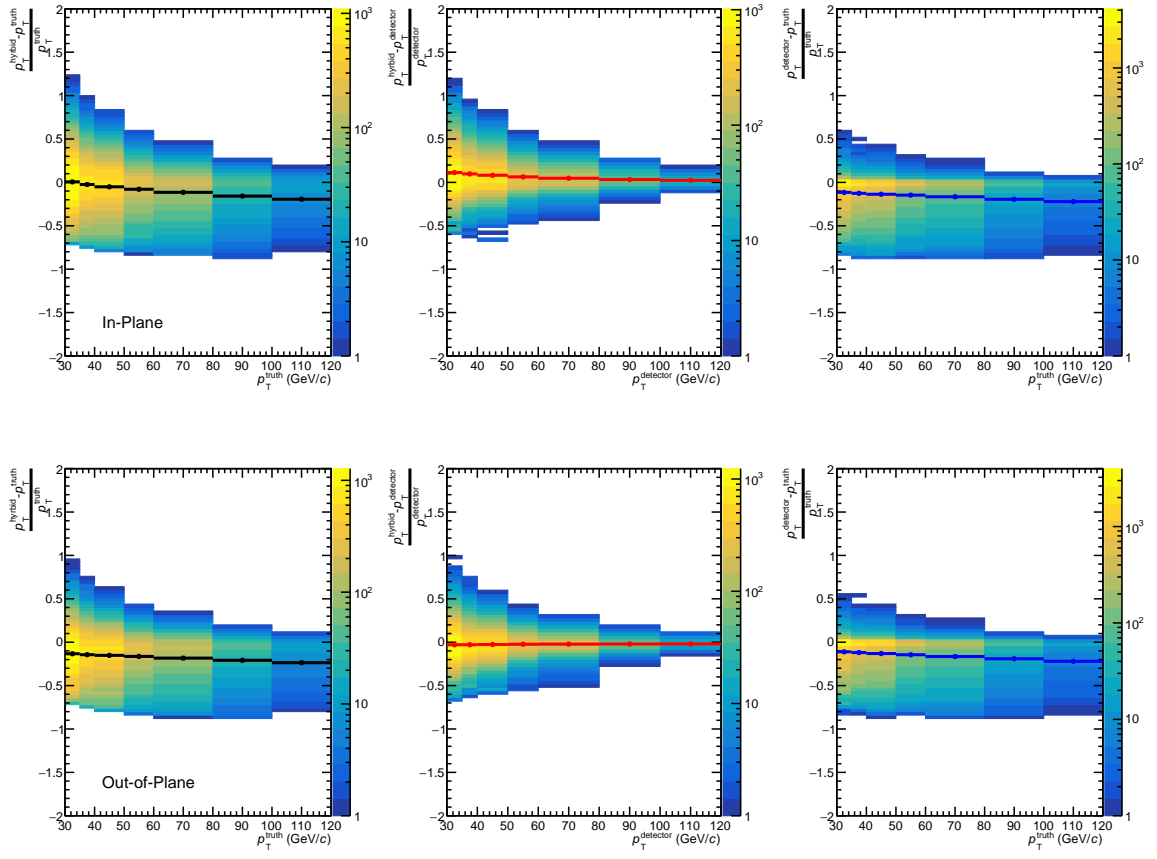


Figure B.8: Residual plots for $R = 0.4$ jets.

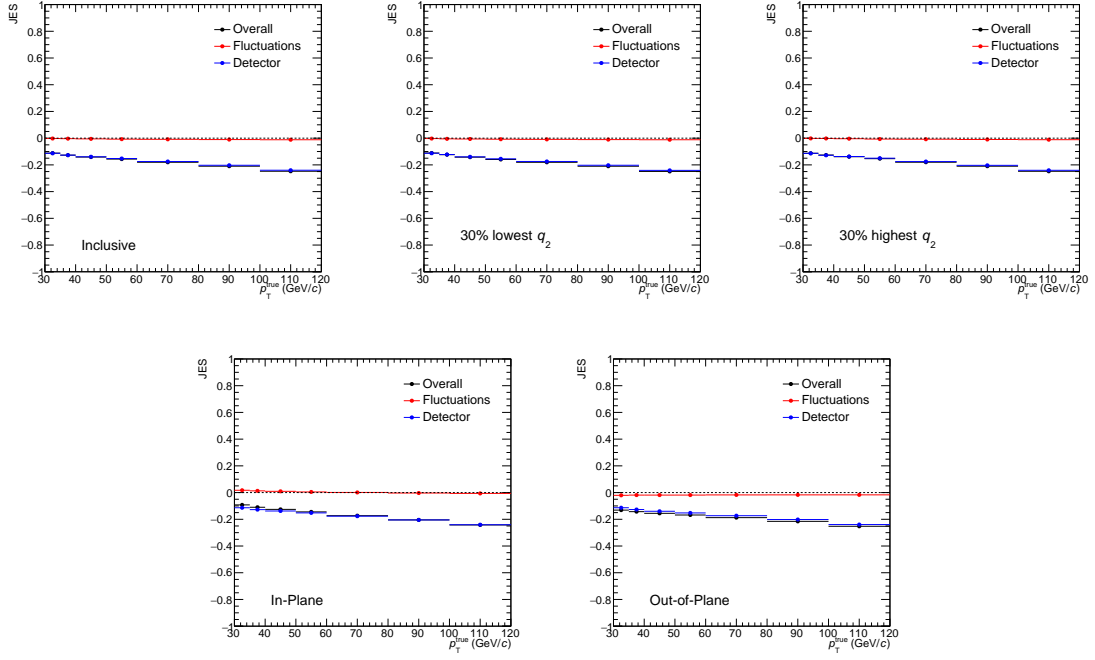


Figure B.9: Jet Energy Scale (JES) plots for $R = 0.2$ jets.

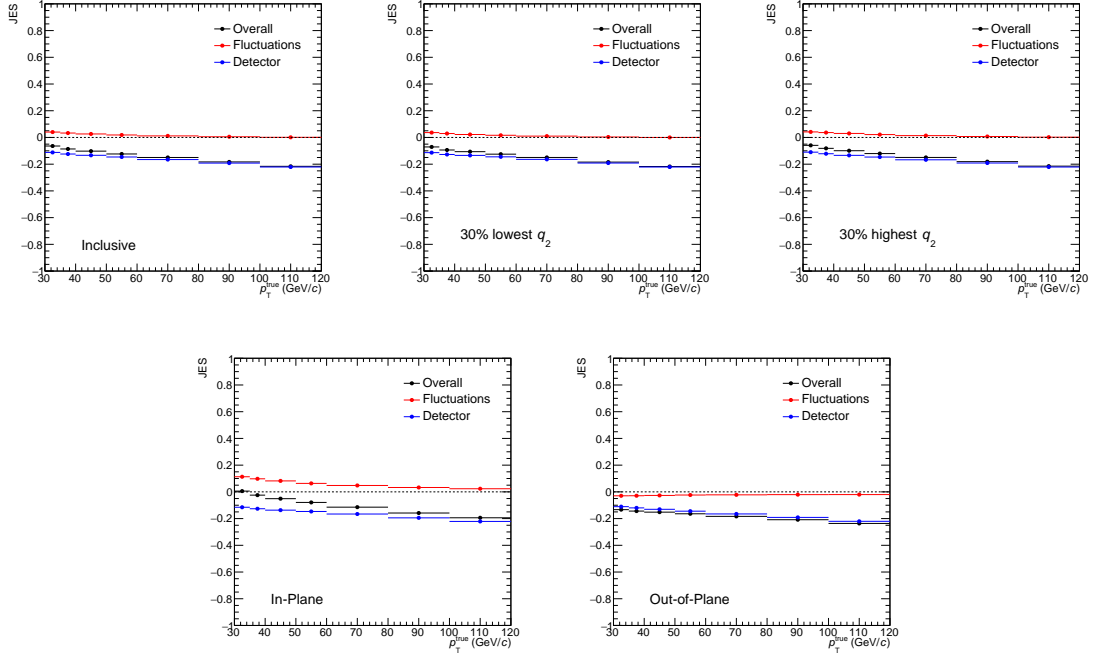


Figure B.10: Jet Energy Scale (JES) plots for $R = 0.4$ jets.

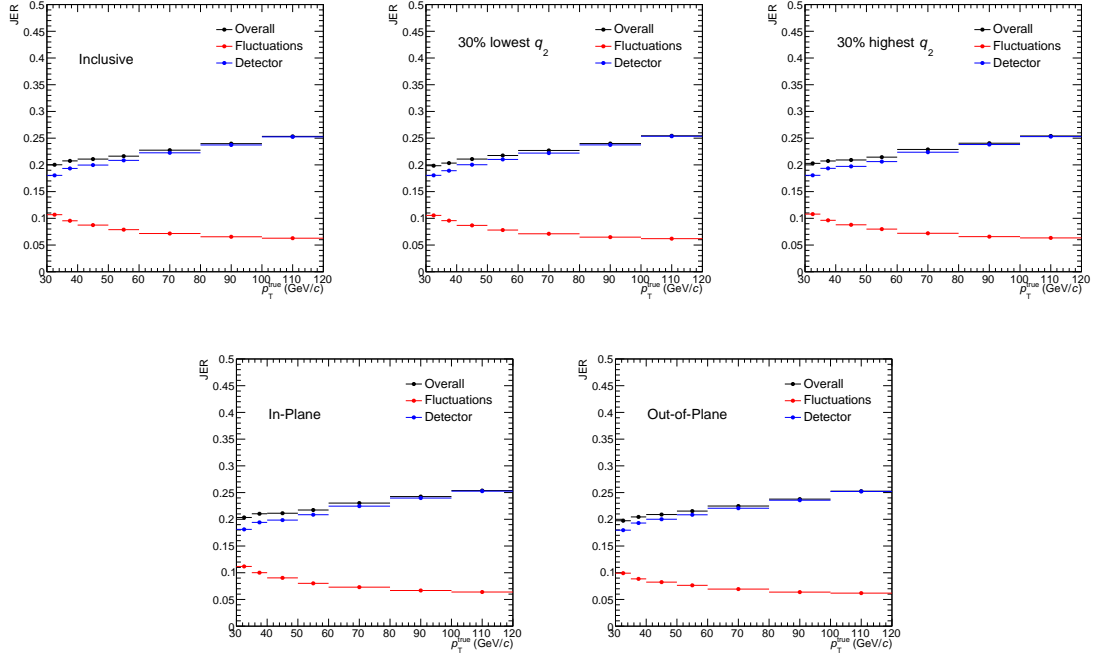


Figure B.11: Jet Energy Resolution (JER) plots for $R = 0.2$ jets.

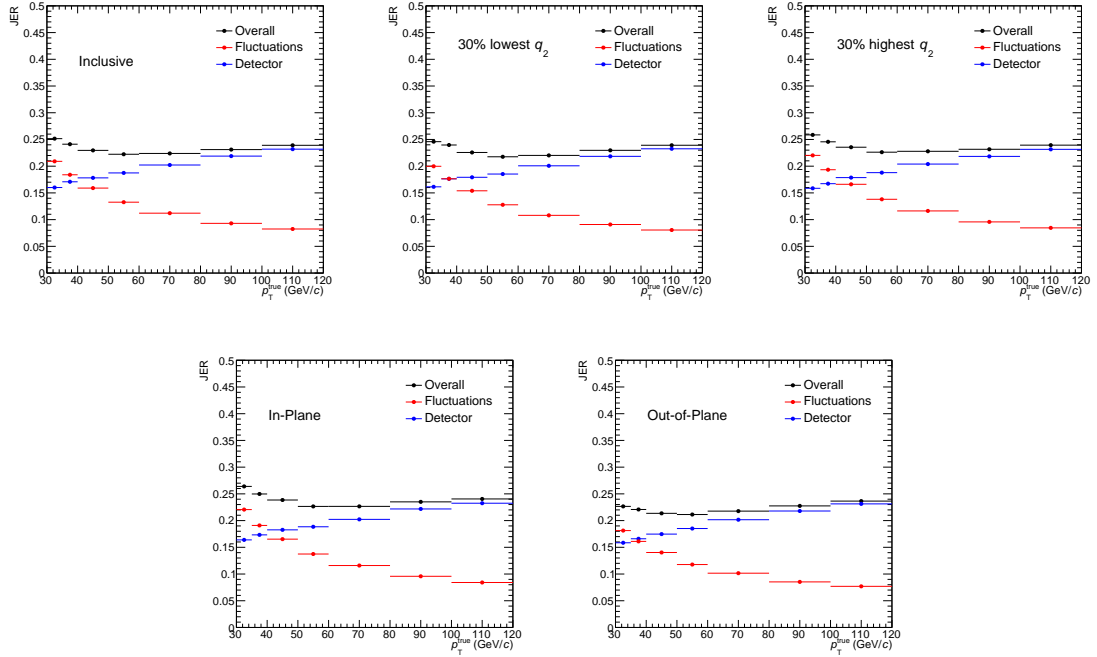


Figure B.12: Jet Energy Resolution (JER) plots for $R = 0.4$ jets.

Response

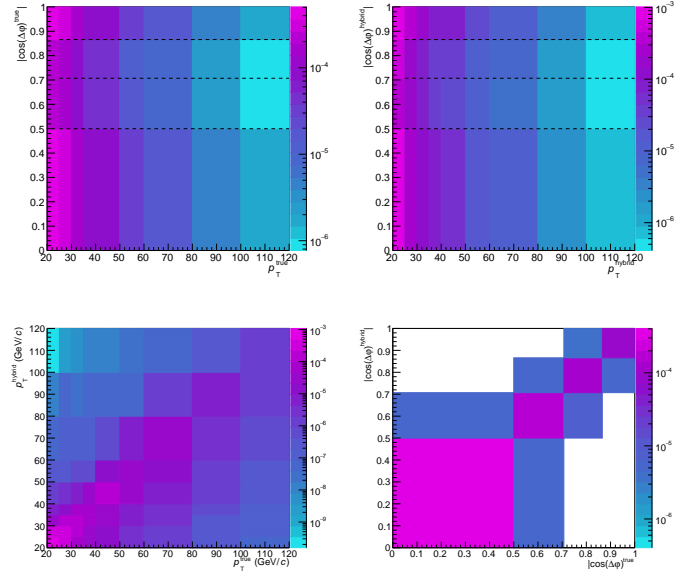


Figure B.13: Projections of the response matrix, $R = 0.2$.

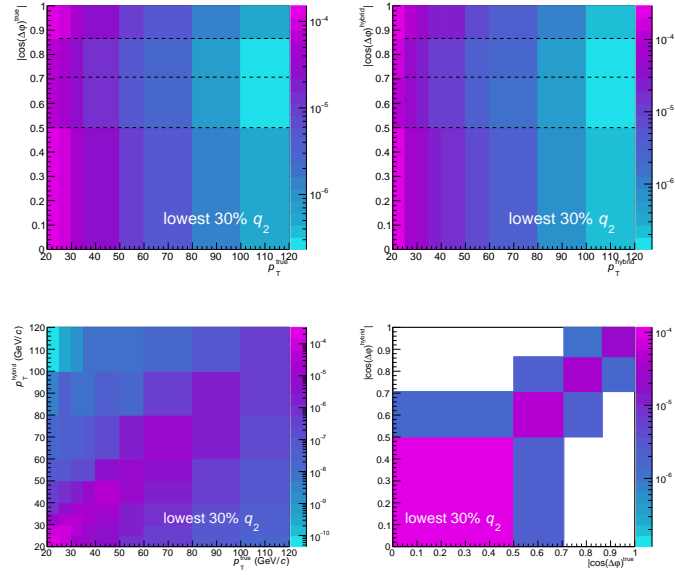


Figure B.14: Projections of the response matrix for the lowest 30% q_2 , $R = 0.2$.

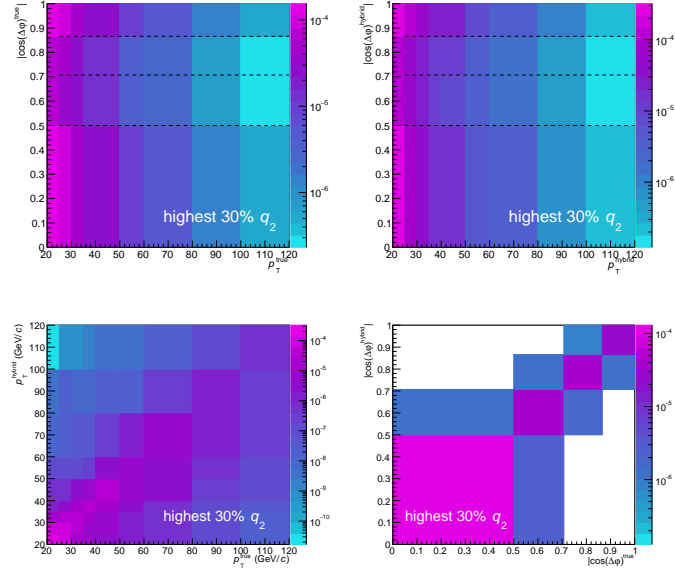


Figure B.15: Projections of the response matrix for the highest 30% q_2 , $R = 0.2$.

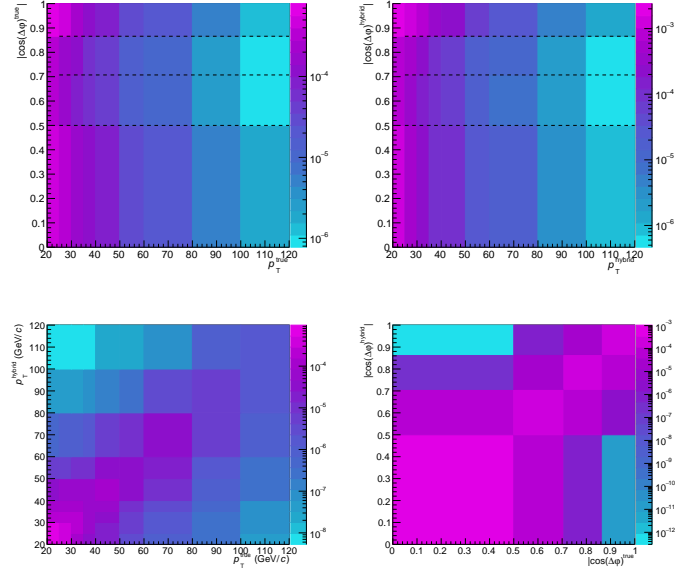


Figure B.16: Projections of the response matrix, $R = 0.4$.

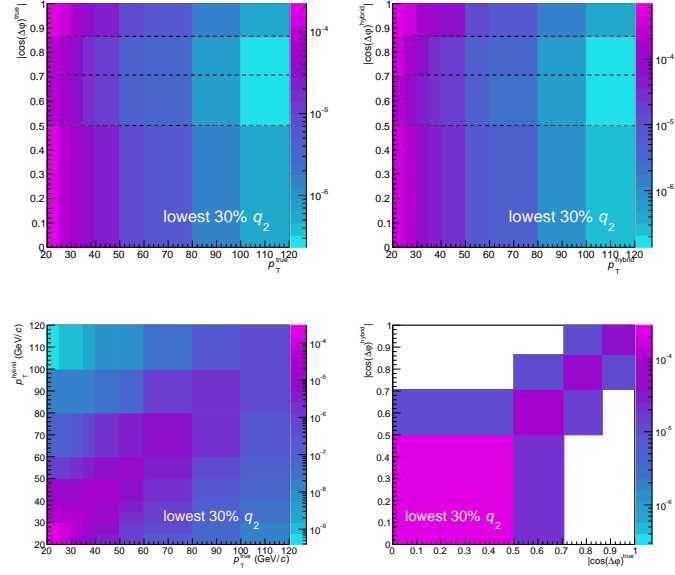


Figure B.17: Projections of the response matrix for the lowest 30% q_2 , $R = 0.4$.

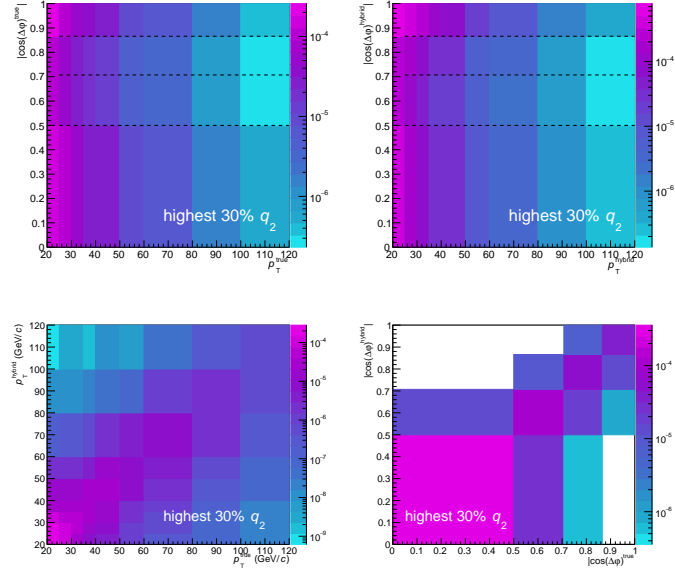


Figure B.18: Projections of the response matrix for the highest 30% q_2 , $R = 0.4$.

Unfolding

This section contains the full set of stability and closure tests for the unfolding.

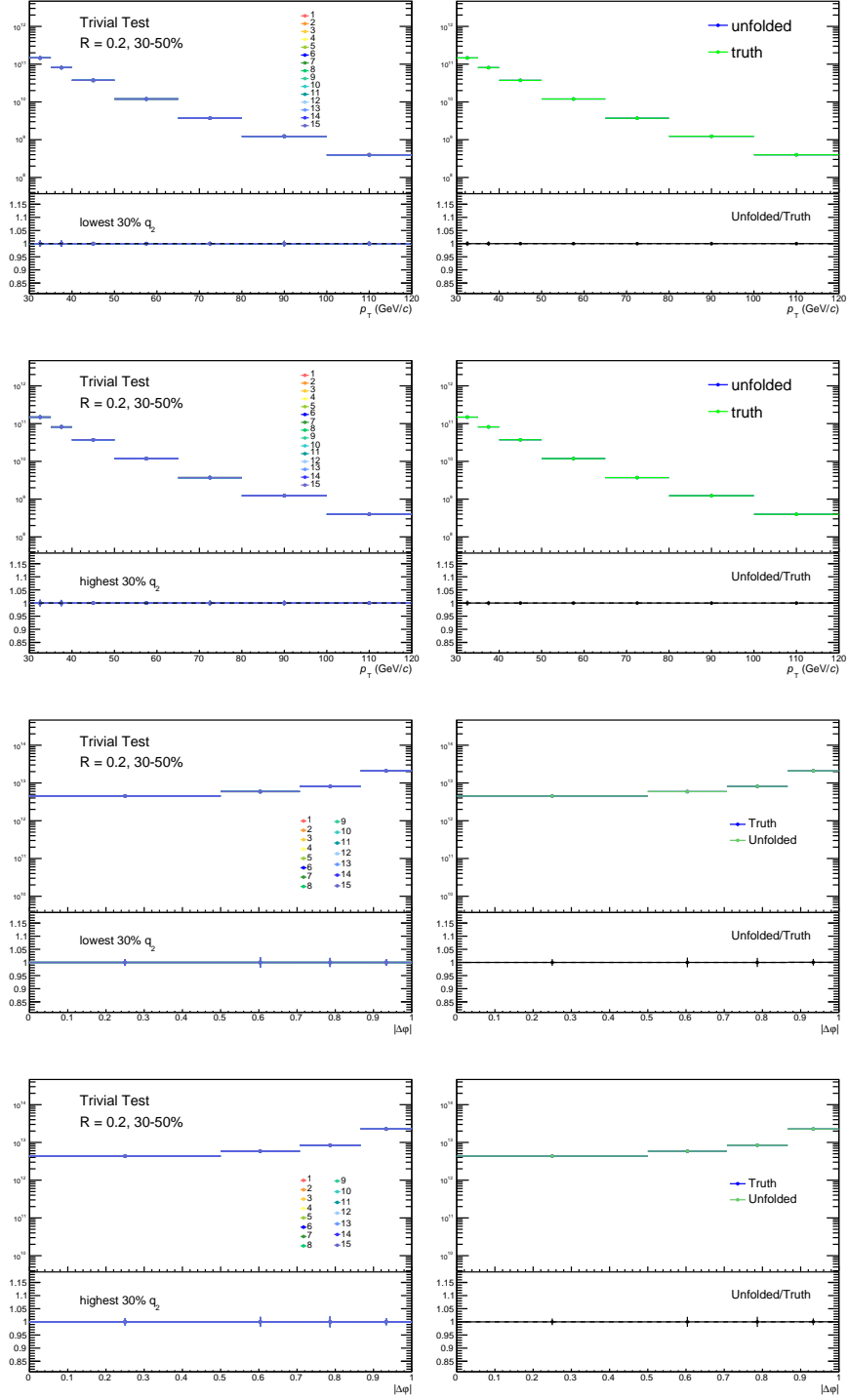


Figure B.19: Trivial unfolding tests for $R = 0.2$ jet sample.

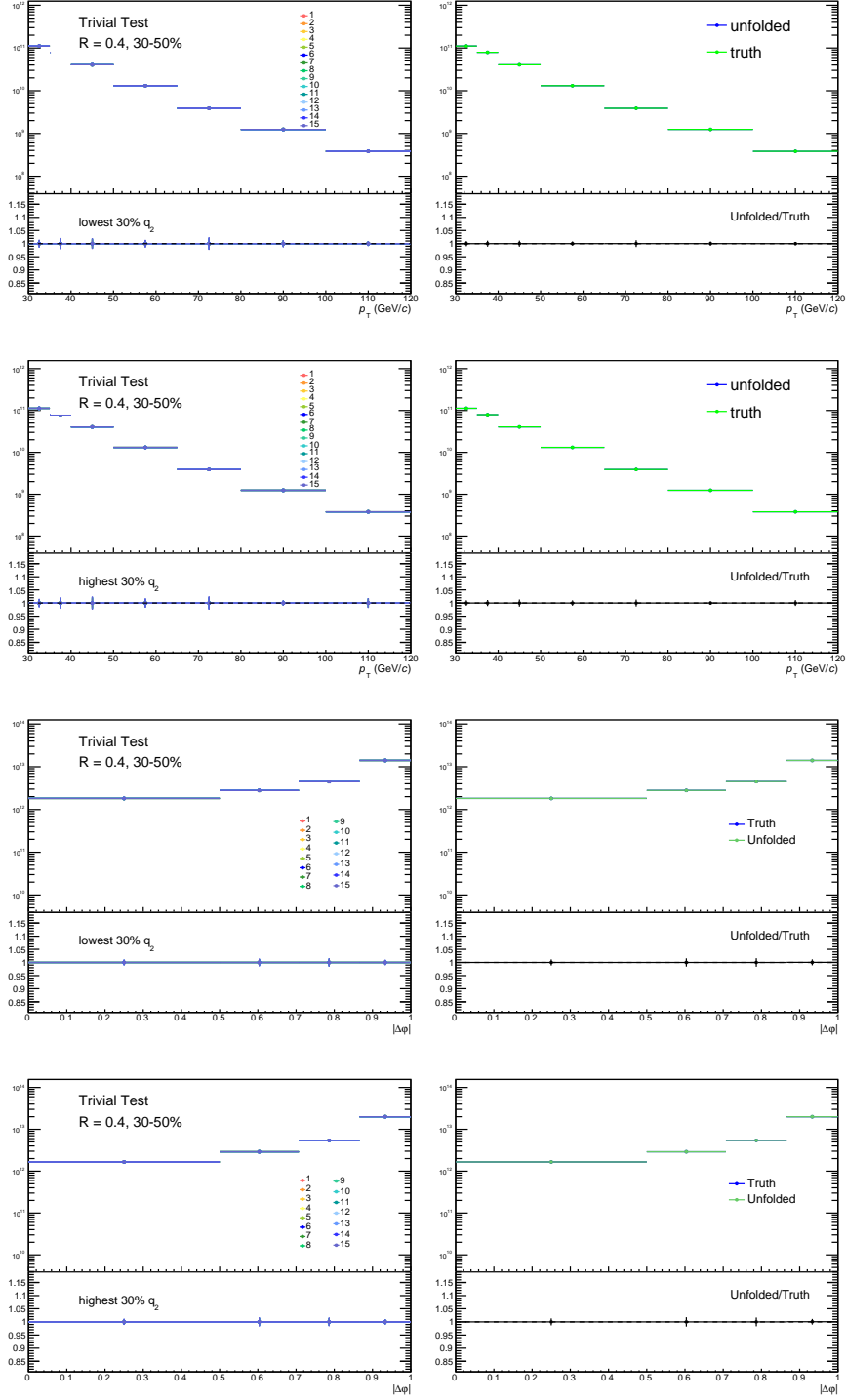


Figure B.20: Trivial unfolding tests for $R = 0.4$ jet sample.

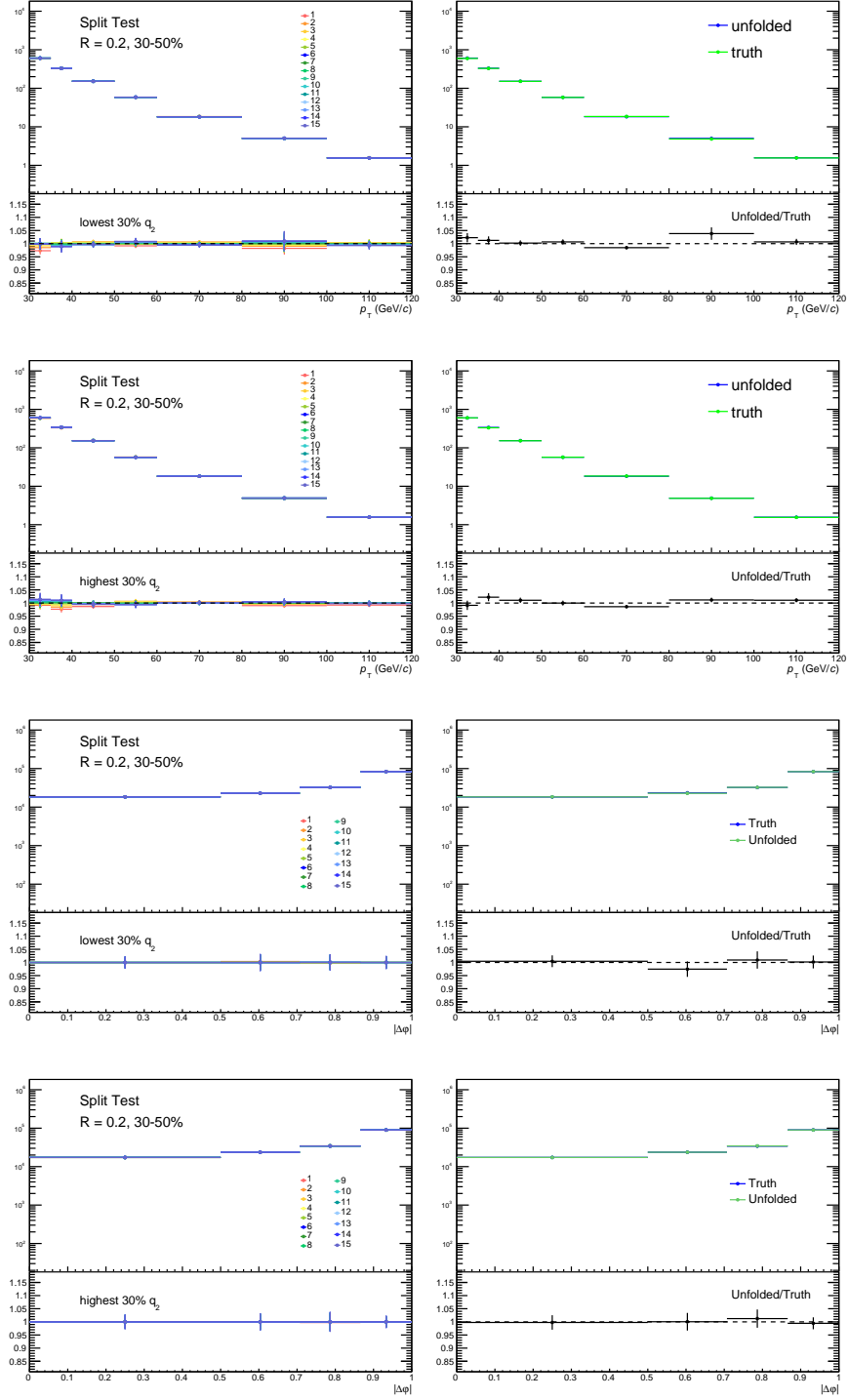


Figure B.21: Split unfolding tests for $R = 0.2$ jet sample.

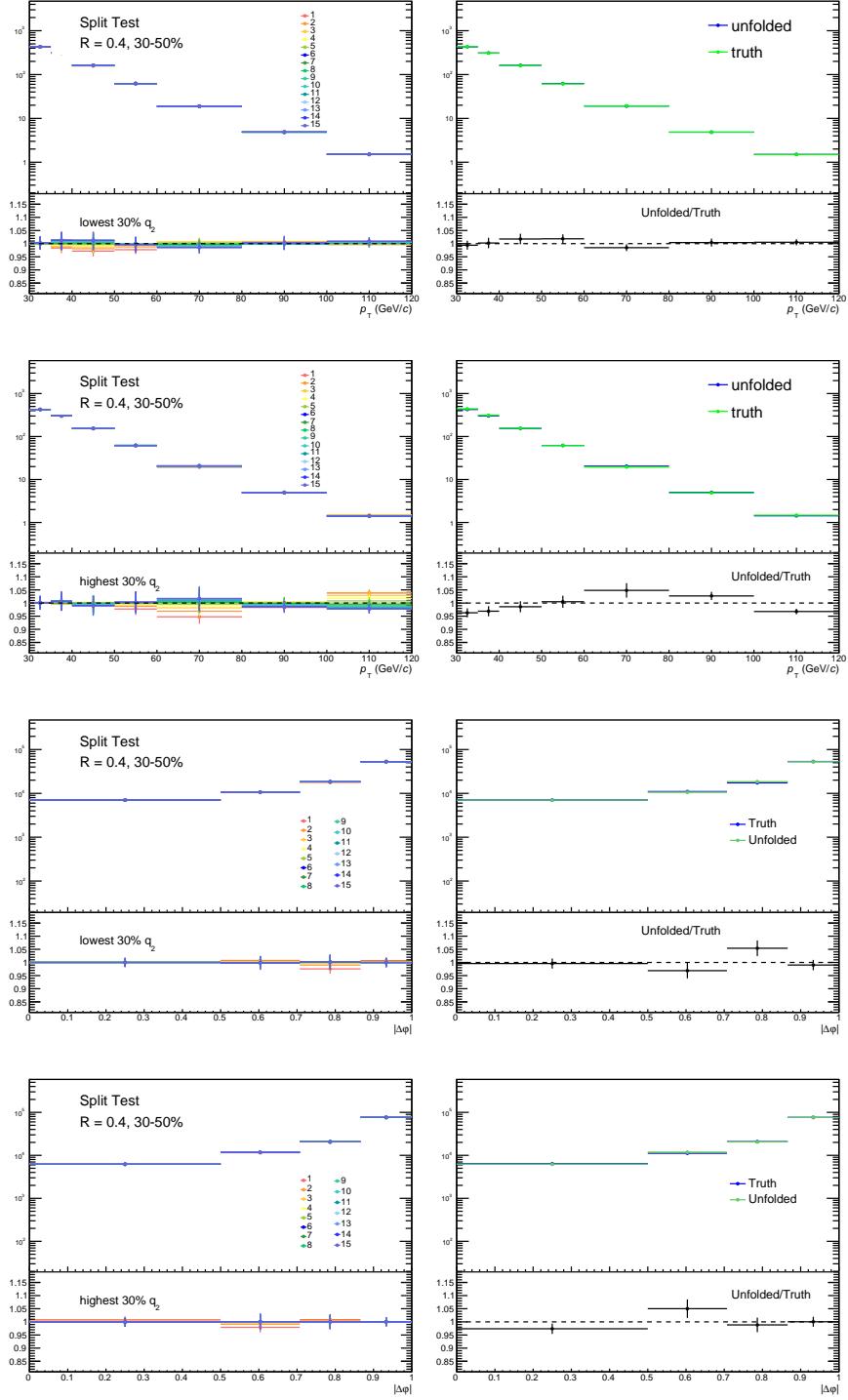


Figure B.22: Split unfolding tests for $R = 0.4$ jet sample.

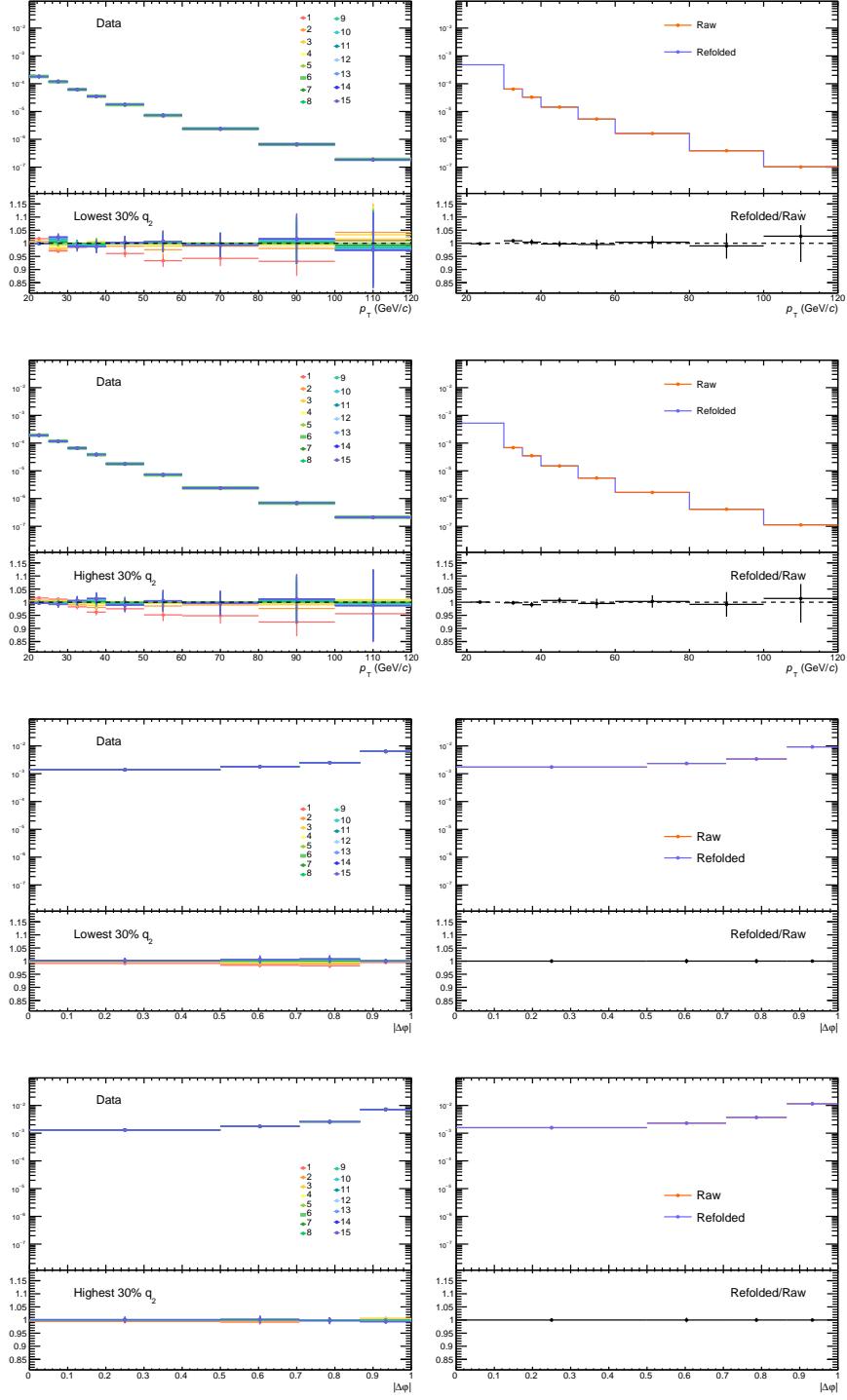


Figure B.23: Data unfolding tests for $R = 0.2$ jet sample.

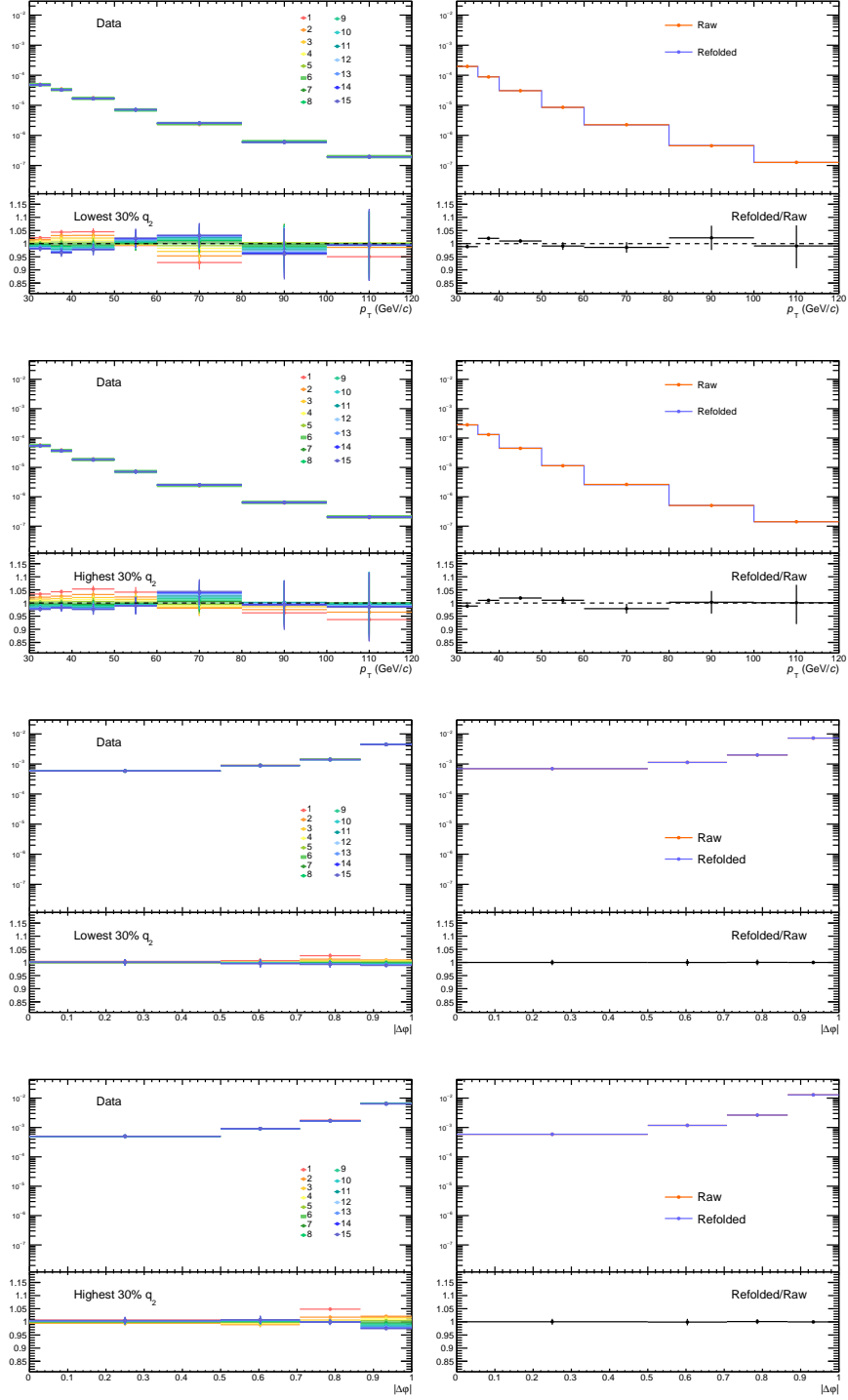


Figure B.24: Data unfolding tests for $R = 0.4$ jet sample.

“Hope this helps, as I ate three portions of salmon last week and was worried!”

— John Harris

Appendix C

Systematic Uncertainties

This appendix contains the full set of systematic uncertainties studied in this analysis.

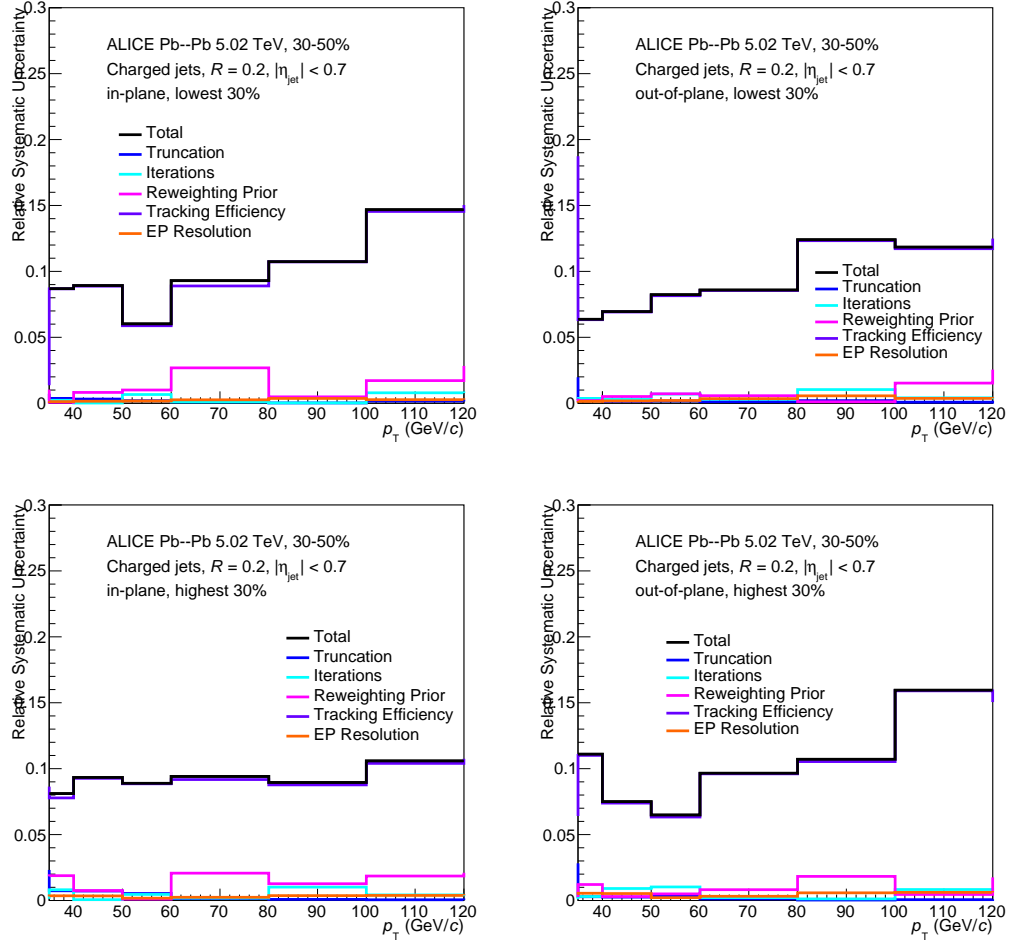


Figure C.1: Systematics for sorted spectra, $R = 0.2$.

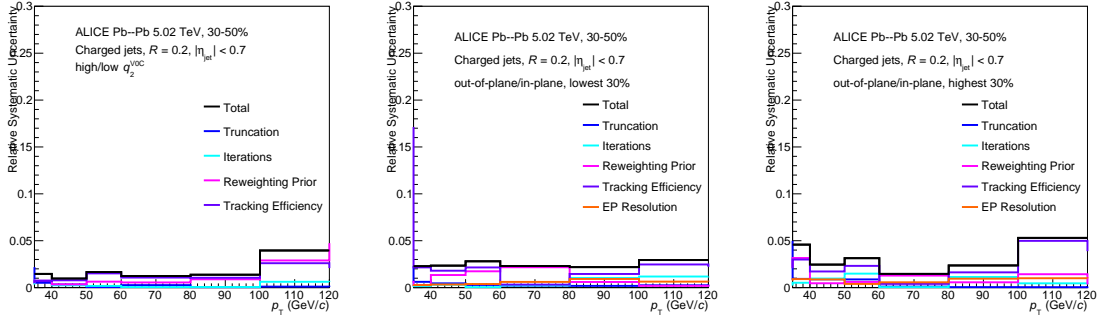


Figure C.2: Combined systematics for ratios of in-plane and out-of-plane jets, $R = 0.2$.

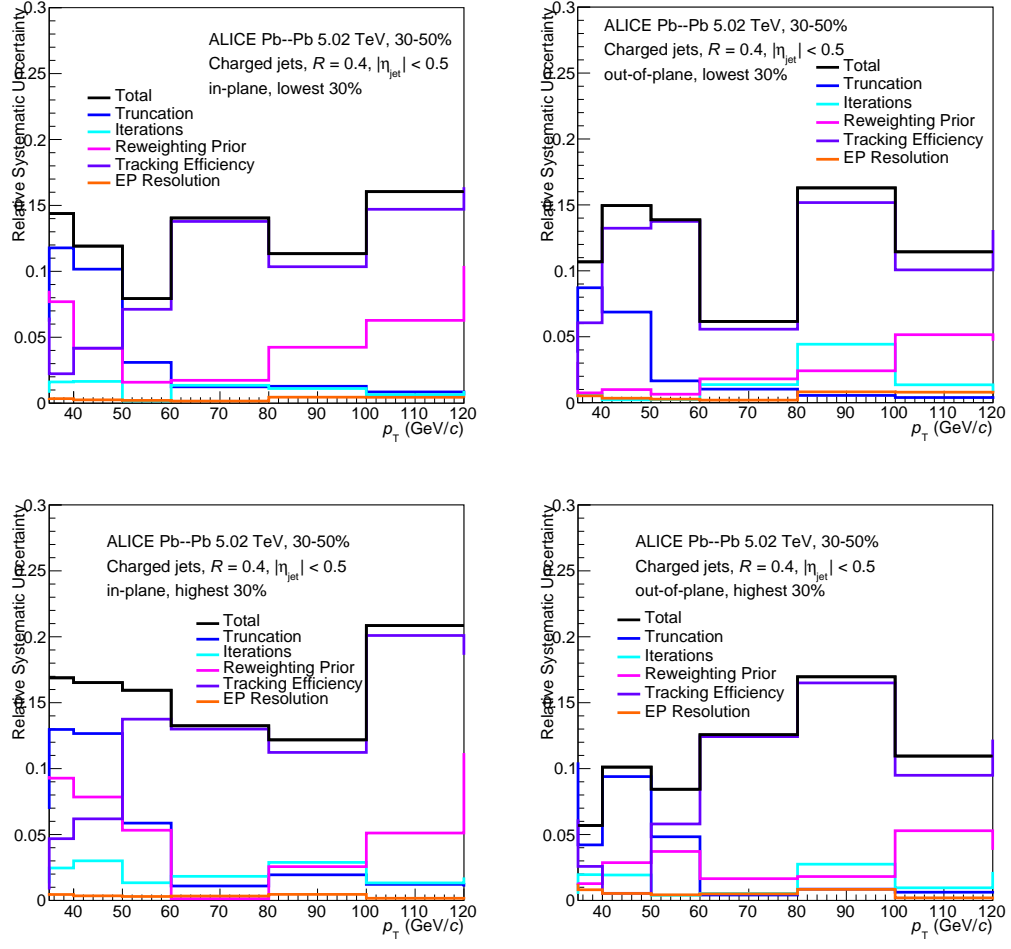


Figure C.3: Systematics for sorted spectra, $R = 0.4$.

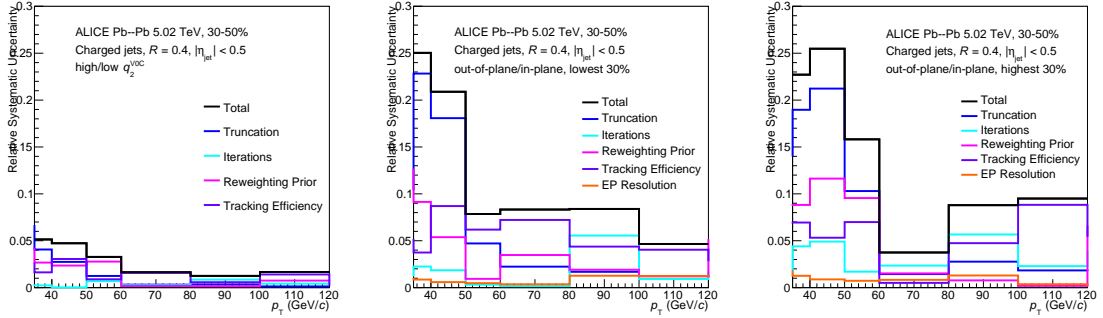


Figure C.4: Combined systematics for ratios of in-plane and out-of-plane jets, $R = 0.4$.

“Because this table was initially derived from published results and many of those results were preliminary, as many as 64 of the mesons in the following table may not exist or have the wrong mass or quantum numbers.”

— Wikipedia, *List of Mesons*

Bibliography

- [1] J. Woithe, G. J. Wiener, and F. F. Van der Veken, “Let’s have a coffee with the Standard Model of particle physics!”, *Phys. Educ.* **52** no. 3, (2017) .
- [2] **ATLAS**, “Standard Model Summary Plots June 2021”,.
- [3] C.-N. Yang and R. L. Mills, “Conservation of Isotopic Spin and Isotopic Gauge Invariance”, *Phys. Rev.* **96** (1954) .
- [4] M. E. Peskin and D. V. Schroeder, *An Introduction to quantum field theory*. Addison-Wesley, Reading, USA, 1995.
- [5] S. Mandelstam, “Determination of the pion - nucleon scattering amplitude from dispersion relations and unitarity. General theory”, *Phys. Rev.* **112** (1958) .
- [6] **ALPHA** Collaboration, M. Bruno, M. Dalla Brida, P. Fritzsche, T. Korzec, A. Ramos, S. Schaefer, H. Simma, S. Sint, and R. Sommer, “The Λ -parameter in 3-flavour QCD and $\alpha_s(m_Z)$ by the ALPHA collaboration”, *PoS LATTICE2016* (2016) , [arXiv:1701.03075 \[hep-lat\]](#).
- [7] A. Bazavov, N. Brambilla, X. G. Tormo, I. P. Petreczky, J. Soto, and A. Vairo, “Determination of α_s from the QCD static energy: An update”, *Phys. Rev. D* **90** no. 7, (2014) , [arXiv:1407.8437 \[hep-ph\]](#). [Erratum: *Phys.Rev.D* 101, 119902 (2020)].

- [8] **Particle Data Group**, R. L. Workman *et al.*, “Review of Particle Physics”, *PTEP* **2022** (2022) .
- [9] J. C. Collins, D. E. Soper, and G. F. Sterman, “Factorization of Hard Processes in QCD”, *Adv. Ser. Direct. High Energy Phys.* **5** (1989) , [arXiv:hep-ph/0409313](#).
- [10] A. Accardi *et al.*, “Electron Ion Collider: The Next QCD Frontier: Understanding the glue that binds us all”, *Eur. Phys. J. A* **52** no. 9, (2016) , [arXiv:1212.1701 \[nucl-ex\]](#).
- [11] S. Bailey, T. Cridge, L. A. Harland-Lang, A. D. Martin, and R. S. Thorne, “Parton distributions from LHC, HERA, Tevatron and fixed target data: MSHT20 PDFs”, *Eur. Phys. J. C* **81** no. 4, (2021) , [arXiv:2012.04684 \[hep-ph\]](#).
- [12] Y. L. Dokshitzer, “Calculation of the Structure Functions for Deep Inelastic Scattering and $e^+ e^-$ Annihilation by Perturbation Theory in Quantum Chromodynamics.”, *Sov. Phys. JETP* **46** (1977) .
- [13] V. N. Gribov and L. N. Lipatov, “Deep inelastic $e p$ scattering in perturbation theory”, *Sov. J. Nucl. Phys.* **15** (1972) .
- [14] G. Altarelli and G. Parisi, “Asymptotic Freedom in Parton Language”, *Nucl. Phys. B* **126** (1977) .
- [15] B. R. Webber, “Fragmentation and hadronization”, *Int. J. Mod. Phys. A* **15S1** (2000) , [arXiv:hep-ph/9912292](#).
- [16] **ALICE** Collaboration, “Centrality determination in heavy ion collisions”, 2018. <https://cds.cern.ch/record/2636623>.
- [17] R. Snellings, “Elliptic Flow: A Brief Review”, *New J. Phys.* **13** (2011) , [arXiv:1102.3010 \[nucl-ex\]](#).

- [18] G.-Y. Qin and X.-N. Wang, “Jet quenching in high-energy heavy-ion collisions”, *Int. J. Mod. Phys. E* **24** no. 11, (2015) , [arXiv:1511.00790](#) [hep-ph].
- [19] **STAR** Collaboration, J. Adams *et al.*, “Evidence from d + Au measurements for final state suppression of high p_T hadrons in Au+Au collisions at RHIC”, *Phys. Rev. Lett.* **91** (2003) , [arXiv:nuc1-ex/0306024](#).
- [20] **ALICE** Collaboration, S. Acharya *et al.*, “Measurements of inclusive jet spectra in pp and central Pb-Pb collisions at $\sqrt{s_{NN}} = 5.02$ TeV”, *Phys. Rev. C* **101** no. 3, (2020) , [arXiv:1909.09718](#) [nucl-ex].
- [21] **ATLAS** Collaboration, G. Aad *et al.*, “Measurements of the Nuclear Modification Factor for Jets in Pb+Pb Collisions at $\sqrt{s_{NN}} = 2.76$ TeV with the ATLAS Detector”, *Phys. Rev. Lett.* **114** no. 7, (2015) , [arXiv:1411.2357](#) [hep-ex].
- [22] **ATLAS** Collaboration, M. Aaboud *et al.*, “Measurement of the nuclear modification factor for inclusive jets in Pb+Pb collisions at $\sqrt{s_{NN}} = 5.02$ TeV with the ATLAS detector”, *Phys. Lett. B* **790** (2019) , [arXiv:1805.05635](#) [nucl-ex].
- [23] **CMS** Collaboration, V. Khachatryan *et al.*, “Measurement of inclusive jet cross sections in pp and PbPb collisions at $\sqrt{s_{NN}} = 2.76$ TeV”, *Phys. Rev. C* **96** no. 1, (2017) , [arXiv:1609.05383](#) [nucl-ex].
- [24] T. Matsui and H. Satz, “ J/ψ Suppression by Quark-Gluon Plasma Formation”, *Phys. Lett. B* **178** (1986) .
- [25] **ALICE** Collaboration, “ $\psi(2S)$ suppression in Pb-Pb collisions at the LHC”, [arXiv:2210.08893](#) [nucl-ex].
- [26] **CMS** Collaboration, A. M. Sirunyan *et al.*, “Measurement of prompt and nonprompt charmonium suppression in PbPb collisions at 5.02 TeV”, *Eur. Phys. J. C* **78** no. 6, (2018) , [arXiv:1712.08959](#) [nucl-ex].

- [27] P. Koch, B. Muller, and J. Rafelski, “Strangeness in Relativistic Heavy Ion Collisions”, *Phys. Rept.* **142** (1986) .
- [28] **ALICE** Collaboration, J. Adam *et al.*, “Enhanced production of multi-strange hadrons in high-multiplicity proton-proton collisions”, *Nature Phys.* **13** (2017) , [arXiv:1606.07424 \[nucl-ex\]](#).
- [29] **ALICE** Collaboration, S. Acharya *et al.*, “Production of charged pions, kaons, and (anti-)protons in Pb-Pb and inelastic *pp* collisions at $\sqrt{s_{\text{NN}}} = 5.02$ TeV”, *Phys. Rev. C* **101** no. 4, (2020) , [arXiv:1910.07678 \[nucl-ex\]](#).
- [30] J. Noronha-Hostler, “Hydrodynamics overview”, 2016. Presentation given at Hot Quarks 2016.
- [31] **ALICE** Collaboration, J. Adam *et al.*, “Anisotropic flow of charged particles in Pb-Pb collisions at $\sqrt{s_{\text{NN}}} = 5.02$ TeV”, *Phys. Rev. Lett.* **116** no. 13, (2016) , [arXiv:1602.01119 \[nucl-ex\]](#).
- [32] J. Noronha-Hostler, M. Luzum, and J.-Y. Ollitrault, “Hydrodynamic predictions for 5.02 TeV Pb-Pb collisions”, *Phys. Rev. C* **93** no. 3, (2016) , [arXiv:1511.06289 \[nucl-th\]](#).
- [33] **HotQCD** Collaboration, A. Bazavov *et al.*, “Equation of state in (2+1)-flavor QCD”, *Phys. Rev. D* **90** (2014) , [arXiv:1407.6387 \[hep-lat\]](#).
- [34] R. Gupta, “Introduction to lattice QCD: Course”, in *Les Houches Summer School in Theoretical Physics, Session 68: Probing the Standard Model of Particle Interactions*, pp. 83–219. 7, 1997. [arXiv:hep-lat/9807028](#).
- [35] **Nuclear Science Advisory Committee**, A. Aprahamian *et al.*, “Reaching for the horizon: The 2015 long range plan for nuclear science”, 10, 2015.
- [36] U. Heinz, C. Shen, and H. Song, “The viscosity of quark-gluon plasma at RHIC and the LHC”, *AIP Conf. Proc.* **1441** no. 1, (2012) , [arXiv:1108.5323 \[nucl-th\]](#).

- [37] **ALICE** Collaboration, “The ALICE experiment - A journey through QCD”,
arXiv:2211.04384 [nucl-ex].
- [38] J. Schukraft, A. Timmins, and S. A. Voloshin, “Ultra-relativistic nuclear
collisions: event shape engineering”, *Phys. Lett. B* **719** (2013) ,
arXiv:1208.4563 [nucl-ex].
- [39] **ALICE** Collaboration, K. Aamodt *et al.*, “The ALICE experiment at the
CERN LHC”, *JINST* **3** (2008) .
- [40] **LHCb** Collaboration, A. A. Alves, Jr. *et al.*, “The LHCb Detector at the
LHC”, *JINST* **3** (2008) .
- [41] **CMS** Collaboration, S. Chatrchyan *et al.*, “The CMS Experiment at the
CERN LHC”, *JINST* **3** (2008) .
- [42] **ATLAS** Collaboration, G. Aad *et al.*, “The ATLAS Experiment at the
CERN Large Hadron Collider”, *JINST* **3** (2008) .
- [43] N. Angert *et al.*, “CERN heavy ion facility design report”,
<https://lib-extopc.kek.jp/preprints/PDF/1993/9306/9306544.pdf>.
- [44] CERN Website, “The Low Energy Ion Ring”, 2012.
<https://cds.cern.ch/record/1997352>.
- [45] J.-P. Burnet *et al.*, “Fifty years of the CERN Proton Synchrotron : Volume
2”, arXiv:1309.6923 [physics.acc-ph].
- [46] CERN Website, “The Proton Synchrotron”, 2012.
<https://cds.cern.ch/record/1997189>.
- [47] “The Super Proton Synchrotron”,
<https://cds.cern.ch/record/1997188>.
- [48] CERN. <https://cds.cern.ch/images/CERN-GRAPHICS-2022-001-1>.
Accessed: 2022-12-15.

- [49] A. Tauro, “ALICE Schematics”, 2017.
<https://cds.cern.ch/record/2263642>. General Photo.
- [50] **ALICE** Collaboration, “Upgrade of the ALICE Time Projection Chamber”,
tech. rep., Oct, 2013. <https://cds.cern.ch/record/1622286>.
- [51] **ALICE** Collaboration, S. Acharya *et al.*, “Exploration of jet substructure
using iterative declustering in pp and Pb–Pb collisions at LHC energies”,
Phys. Lett. B **802** (2020) , [arXiv:1905.02512](https://arxiv.org/abs/1905.02512) [nucl-ex].
- [52] **ALICE** Collaboration, S. Acharya *et al.*, “Measurement of the groomed jet
radius and momentum splitting fraction in pp and Pb–Pb collisions at
 $\sqrt{s_{NN}} = 5.02$ TeV”, *Phys. Rev. Lett.* **128** no. 10, (2022) , [arXiv:2107.12984](https://arxiv.org/abs/2107.12984)
[nucl-ex].
- [53] Appelshauser, Harald and others, “Space-charge distortion measurements and
their calibration in the ALICE TPC.” ALICE Public Note, 2018.
- [54] F. Sauli, “Gem: A new concept for electron amplification in gas detectors”,
Nuclear Instruments and Methods in Physics Research A **386** (1997) .
- [55] Y. Giomataris, P. Rebourgeard, J. P. Robert, and G. Charpak,
“MICROMEGAS: A High granularity position sensitive gaseous detector for
high particle flux environments” , *Nucl. Instrum. Meth. A* **376** (1996) .
- [56] **ALICE** Collaboration, “ALICE upgrades during the LHC Long Shutdown 2” ,
[arXiv:2302.01238](https://arxiv.org/abs/2302.01238) [physics.ins-det].
- [57] B. Azmoun, C. Beattie, J. W. Harris, R. Majka, N. Smirnov, and C. Woody,
“Options for gain elements and gas mixtures in a high rate eic time projection
chamber”, in *2020 IEEE Nuclear Science Symposium and Medical Imaging
Conference (NSS/MIC)*, pp. 1–4. 2020.
- [58] **ALICE TPC** Collaboration, J. Adolfsson *et al.*, “The upgrade of the ALICE
TPC with GEMs and continuous readout” , *JINST* **16** no. 03, (2021) ,
[arXiv:2012.09518](https://arxiv.org/abs/2012.09518) [physics.ins-det].

- [59] L. Breiman, “Random Forests”, *Machine Learning* **45** (2001) .
- [60] **ALICE** Collaboration, K. Aamodt *et al.*, “Alignment of the ALICE Inner Tracking System with cosmic-ray tracks”, *JINST* **5** (2010) , [arXiv:1001.0502 \[physics.ins-det\]](#).
- [61] **ALICE** Collaboration, E. Abbas *et al.*, “Performance of the ALICE VZERO system”, *JINST* **8** (2013) , [arXiv:1306.3130 \[nucl-ex\]](#).
- [62] **ALICE** Collaboration, B. B. Abelev *et al.*, “Performance of the ALICE Experiment at the CERN LHC”, *Int. J. Mod. Phys. A* **29** (2014) , [arXiv:1402.4476 \[nucl-ex\]](#).
- [63] **ALICE** Collaboration, C. W. Fabjan, L. Jirdén, V. Lindestruth, L. Riccati, D. Rorich, P. Van de Vyvre, O. Villalobos Baillie, and H. de Groot, *ALICE trigger data-acquisition high-level trigger and control system: Technical Design Report*. Technical design report. ALICE. CERN, Geneva, 2004. <http://cds.cern.ch/record/684651>.
- [64] **ALICE** Collaboration, “Performance of the ALICE Electromagnetic Calorimeter”, [arXiv:2209.04216 \[physics.ins-det\]](#).
- [65] F. D’Eramo, K. Rajagopal, and Y. Yin, “Molière scattering in quark-gluon plasma: finding point-like scatterers in a liquid”, *JHEP* **01** (2019) , [arXiv:1808.03250 \[hep-ph\]](#).
- [66] L. Havener, “Jet overview”, 2022. Presentation given at Hot Quarks 2022.
- [67] U. A. Wiedemann, “Jet Quenching in Heavy Ion Collisions”, [arXiv:0908.2306 \[hep-ph\]](#).
- [68] J. Casalderrey-Solana, D. C. Gulhan, J. G. Milhano, D. Pablos, and K. Rajagopal, “A Hybrid Strong/Weak Coupling Approach to Jet Quenching”, *JHEP* **10** (2014) , [arXiv:1405.3864 \[hep-ph\]](#). [Erratum: *JHEP* **09**, 175 (2015)].

- [69] D. d’Enterria, “Jet quenching”, *Landolt-Bornstein* **23** (2010) ,
arXiv:0902.2011 [nucl-ex].
- [70] R. Baier, Y. L. Dokshitzer, A. H. Mueller, S. Peigne, and D. Schiff, “Radiative energy loss of high-energy quarks and gluons in a finite volume quark - gluon plasma”, *Nucl. Phys. B* **483** (1997) , arXiv:hep-ph/9607355.
- [71] M. Gyulassy, P. Levai, and I. Vitev, “NonAbelian energy loss at finite opacity”, *Phys. Rev. Lett.* **85** (2000) , arXiv:nucl-th/0005032.
- [72] P. B. Arnold, G. D. Moore, and L. G. Yaffe, “Photon and gluon emission in relativistic plasmas”, *JHEP* **06** (2002) , arXiv:hep-ph/0204343.
- [73] X.-f. Guo and X.-N. Wang, “Multiple scattering, parton energy loss and modified fragmentation functions in deeply inelastic e A scattering”, *Phys. Rev. Lett.* **85** (2000) , arXiv:hep-ph/0005044.
- [74] K. C. Zapp, “Monte Carlo simulations of jet quenching in heavy ion collisions”, *Nucl. Phys. A* **855** (2011) , arXiv:1012.0177 [hep-ph].
- [75] T. Sjostrand, S. Mrenna, and P. Z. Skands, “PYTHIA 6.4 Physics and Manual”, *JHEP* **05** (2006) , arXiv:hep-ph/0603175.
- [76] T. Sjöstrand, S. Ask, J. R. Christiansen, R. Corke, N. Desai, P. Ilten, S. Mrenna, S. Prestel, C. O. Rasmussen, and P. Z. Skands, “An introduction to PYTHIA 8.2”, *Comput. Phys. Commun.* **191** (2015) , arXiv:1410.3012 [hep-ph].
- [77] V. V. Sudakov, “Vertex parts at very high-energies in quantum electrodynamics”, *Sov. Phys. JETP* **3** (1956) .
- [78] B. Andersson, G. Gustafson, G. Ingelman, and T. Sjostrand, “Parton Fragmentation and String Dynamics”, *Phys. Rept.* **97** (1983) .

- [79] K. Zapp, G. Ingelman, J. Rathsman, J. Stachel, and U. A. Wiedemann, “A Monte Carlo Model for ‘Jet Quenching’”, *Eur. Phys. J. C* **60** (2009) , [arXiv:0804.3568 \[hep-ph\]](#).
- [80] J. Casalderrey-Solana, D. C. Gulhan, J. G. Milhano, D. Pablos, and K. Rajagopal, “A Hybrid Strong/Weak Coupling Approach to Jet Quenching”, *JHEP* **10** (2014) , [arXiv:1405.3864 \[hep-ph\]](#). [Erratum: *JHEP* **09**, 175 (2015)].
- [81] J. H. Putschke *et al.*, “The JETSCAPE framework”, [arXiv:1903.07706 \[nucl-th\]](#).
- [82] B. Schenke, C. Gale, and S. Jeon, “MARTINI: An Event generator for relativistic heavy-ion collisions”, *Phys. Rev. C* **80** (2009) , [arXiv:0909.2037 \[hep-ph\]](#).
- [83] M. L. Miller, K. Reygers, S. J. Sanders, and P. Steinberg, “Glauber modeling in high energy nuclear collisions”, *Ann. Rev. Nucl. Part. Sci.* **57** (2007) , [arXiv:nucl-ex/0701025](#).
- [84] R. D. Woods and D. S. Saxon, “Diffuse Surface Optical Model for Nucleon-Nuclei Scattering”, *Phys. Rev.* **95** (1954) .
- [85] P. Tribedy, “Initial conditions of heavy ion collisions”, 2015. Presentation given at RHIC AGS Annual Users’ Meeting.
- [86] B. Schenke, P. Tribedy, and R. Venugopalan, “Fluctuating Glasma initial conditions and flow in heavy ion collisions”, *Phys. Rev. Lett.* **108** (2012) , [arXiv:1202.6646 \[nucl-th\]](#).
- [87] F. Gelis, E. Iancu, J. Jalilian-Marian, and R. Venugopalan, “The Color Glass Condensate”, *Ann. Rev. Nucl. Part. Sci.* **60** (2010) , [arXiv:1002.0333 \[hep-ph\]](#).

- [88] J. S. Moreland, J. E. Bernhard, and S. A. Bass, “Alternative ansatz to wounded nucleon and binary collision scaling in high-energy nuclear collisions”, *Phys. Rev. C* **92** no. 1, (2015) , [arXiv:1412.4708 \[nucl-th\]](#).
- [89] B. Schenke, S. Jeon, and C. Gale, “(3+1)D hydrodynamic simulation of relativistic heavy-ion collisions”, *Phys. Rev. C* **82** (2010) , [arXiv:1004.1408 \[hep-ph\]](#).
- [90] H. Song, S. A. Bass, and U. Heinz, “Viscous QCD matter in a hybrid hydrodynamic+Boltzmann approach”, *Phys. Rev. C* **83** (2011) , [arXiv:1012.0555 \[nucl-th\]](#).
- [91] P. Christiansen, “Event-Shape Engineering and Jet Quenching”, *J. Phys. Conf. Ser.* **736** no. 1, (2016) , [arXiv:1606.07963 \[hep-ph\]](#).
- [92] K. Fukushima, D. E. Kharzeev, and H. J. Warringa, “The Chiral Magnetic Effect”, *Phys. Rev. D* **78** (2008) , [arXiv:0808.3382 \[hep-ph\]](#).
- [93] M. A. Lisa, S. Pratt, R. Soltz, and U. Wiedemann, “Femtoscopy in relativistic heavy ion collisions”, *Ann. Rev. Nucl. Part. Sci.* **55** (2005) , [arXiv:nucl-ex/0505014](#).
- [94] G. Nijs, W. van der Schee, U. Gürsoy, and R. Snellings, “Bayesian analysis of heavy ion collisions with the heavy ion computational framework Trajectum”, *Phys. Rev. C* **103** no. 5, (2021) , [arXiv:2010.15134 \[nucl-th\]](#).
- [95] C. Beattie, G. Nijs, M. Sas, and W. van der Schee, “Hard probe path lengths and event-shape engineering of the quark-gluon plasma”, *Phys. Lett. B* **836** (2023) , [arXiv:2203.13265 \[nucl-th\]](#).
- [96] F. Cooper and G. Frye, “Comment on the Single Particle Distribution in the Hydrodynamic and Statistical Thermodynamic Models of Multiparticle Production”, *Phys. Rev. D* **10** (1974) .

- [97] **ATLAS** Collaboration, “Measurements of the suppression and correlations of dijets in Pb+Pb collisions at $\sqrt{s_{\text{NN}}} = 5.02$ TeV”, [arXiv:2205.00682](#) [nucl-ex].
- [98] J. G. Milhano and K. C. Zapp, “Origins of the di-jet asymmetry in heavy ion collisions”, *Eur. Phys. J. C* **76** no. 5, (2016) , [arXiv:1512.08107](#) [hep-ph].
- [99] **CMS** Collaboration, S. Chatrchyan *et al.*, “Observation and studies of jet quenching in PbPb collisions at nucleon-nucleon center-of-mass energy = 2.76 TeV”, *Phys. Rev. C* **84** (2011) , [arXiv:1102.1957](#) [nucl-ex].
- [100] **ALICE** Collaboration, J. Adam *et al.*, “Azimuthal anisotropy of charged jet production in $\sqrt{s_{\text{NN}}} = 2.76$ TeV Pb-Pb collisions”, *Phys. Lett. B* **753** (2016) , [arXiv:1509.07334](#) [nucl-ex].
- [101] **ATLAS** Collaboration, G. Aad *et al.*, “Measurement of the Azimuthal Angle Dependence of Inclusive Jet Yields in Pb+Pb Collisions at $\sqrt{s_{\text{NN}}} = 2.76$ TeV with the ATLAS detector”, *Phys. Rev. Lett.* **111** no. 15, (2013) , [arXiv:1306.6469](#) [hep-ex].
- [102] **ALICE** Collaboration, “Azimuthal anisotropy of jet particles in p-Pb and Pb-Pb collisions at $\sqrt{s_{\text{NN}}} = 5.02$ TeV”, [arXiv:2212.12609](#) [nucl-ex].
- [103] **ALICE** Collaboration, J. Adam *et al.*, “Event shape engineering for inclusive spectra and elliptic flow in Pb-Pb collisions at $\sqrt{s_{\text{NN}}} = 2.76$ TeV”, *Phys. Rev. C* **93** no. 3, (2016) , [arXiv:1507.06194](#) [nucl-ex].
- [104] **ALICE** Collaboration, S. Acharya *et al.*, “Event-shape engineering for the D-meson elliptic flow in mid-central Pb-Pb collisions at $\sqrt{s_{\text{NN}}} = 5.02$ TeV”, *JHEP* **02** (2019) , [arXiv:1809.09371](#) [nucl-ex].
- [105] **ALICE** Collaboration, S. Acharya *et al.*, “Transverse-momentum and event-shape dependence of D-meson flow harmonics in Pb–Pb collisions at $\sqrt{s_{\text{NN}}} = 5.02$ TeV”, *Phys. Lett. B* **813** (2021) , [arXiv:2005.11131](#) [nucl-ex].

- [106] W. Ke, Y. Xu, and S. A. Bass, “Linearized Boltzmann-Langevin model for heavy quark transport in hot and dense QCD matter”, *Phys. Rev. C* **98** no. 6, (2018) , [arXiv:1806.08848 \[nucl-th\]](#).
- [107] G. C. Blazey *et al.*, “Run II jet physics”, in *Physics at Run II: QCD and Weak Boson Physics Workshop: Final General Meeting*, pp. 47–77. 5, 2000. [arXiv:hep-ex/0005012](#).
- [108] M. Cacciari, G. P. Salam, and G. Soyez, “The anti- k_T jet clustering algorithm”, *Journal of High Energy Physics* (2008) .
- [109] M. Cacciari, G. P. Salam, and G. Soyez, “FastJet User Manual”, *Eur. Phys. J. C* **72** (2012) , [arXiv:1111.6097 \[hep-ph\]](#).
- [110] **ALICE** Collaboration, B. Abelev *et al.*, “Measurement of Event Background Fluctuations for Charged Particle Jet Reconstruction in Pb-Pb collisions at $\sqrt{s_{NN}} = 2.76$ TeV”, *JHEP* **03** (2012) , [arXiv:1201.2423 \[hep-ex\]](#).
- [111] R. Brun, F. Bruyant, F. Carminati, S. Giani, M. Maire, A. McPherson, G. Patrick, and L. Urban, “GEANT Detector Description and Simulation Tool”,.
- [112] G. D’Agostini, “A multidimensional unfolding method based on Bayes’ theorem”, *Nuclear Instruments and Methods in Physics Research A* **362** (1995) .
- [113] A. Andreassen, P. T. Komiske, E. M. Metodiev, B. Nachman, and J. Thaler, “OmniFold: A Method to Simultaneously Unfold All Observables”, *Phys. Rev. Lett.* **124** no. 18, (2020) , [arXiv:1911.09107 \[hep-ph\]](#).
- [114] T. Adye, “Unfolding algorithms and tests using RooUnfold”, in *PHYSTAT 2011*, pp. 313–318. CERN, Geneva, 2011. [arXiv:1105.1160 \[physics.data-an\]](#).

- [115] A. Poskanzer and S. Voloshin, “Methods for analyzing anisotropic flow in relativistic nuclear collisions”, *Phys. Rev. C* **58** (1998) .
- [116] X.-N. Wang and M. Gyulassy, “HIJING: A Monte Carlo model for multiple jet production in p p, p A and A A collisions”, *Phys. Rev. D* **44** (1991) .
- [117] **ALICE** Collaboration, S. Acharya *et al.*, “Constraining the magnitude of the Chiral Magnetic Effect with Event Shape Engineering in Pb-Pb collisions at $\sqrt{s_{\text{NN}}} = 2.76$ TeV”, *Phys. Lett. B* **777** (2018) , [arXiv:1709.04723](#) [nucl-ex].
- [118] A. Liu on behalf of the **ALICE** Collaboration, “Isolated photon-jet correlations in Pb-Pb collisions at $\sqrt{s_{\text{NN}}} = 5.02$ TeV in ALICE”, in *29th International Conference on Ultra-relativistic Nucleus-Nucleus Collisions*. 8, 2022. [arXiv:2208.08523](#) [nucl-ex].
- [119] **CMS** Collaboration, A. M. Sirunyan *et al.*, “Study of jet quenching with isolated-photon+jet correlations in PbPb and pp collisions at $\sqrt{s_{\text{NN}}} = 5.02$ TeV”, *Phys. Lett. B* **785** (2018) , [arXiv:1711.09738](#) [nucl-ex].
- [120] **PHENIX** Collaboration, A. Adare *et al.*, “An Upgrade Proposal from the PHENIX Collaboration”, [arXiv:1501.06197](#) [nucl-ex].
- [121] **ALICE** Collaboration, “Letter of intent for ALICE 3: A next-generation heavy-ion experiment at the LHC”, [arXiv:2211.02491](#) [physics.ins-det].